

University of Alberta

**Analytical Methods for the Investigation of Adsorbed Protein Films at Chemically
Modified Surfaces**

By

Vishal Kumar Kanda



A thesis submitted to the Faculty of Graduate Studies and Research in partial fulfillment
of the requirements for the degree of Doctor of Philosophy

Department of Chemistry

Edmonton, Alberta, Canada

Fall 2004



Library and
Archives Canada

Bibliothèque et
Archives Canada

Published Heritage
Branch

Direction du
Patrimoine de l'édition

395 Wellington Street
Ottawa ON K1A 0N4
Canada

395, rue Wellington
Ottawa ON K1A 0N4
Canada

Your file *Votre référence*
ISBN: 0-612-95949-X
Our file *Notre référence*
ISBN: 0-612-95949-X

The author has granted a non-exclusive license allowing the Library and Archives Canada to reproduce, loan, distribute or sell copies of this thesis in microform, paper or electronic formats.

L'auteur a accordé une licence non exclusive permettant à la Bibliothèque et Archives Canada de reproduire, prêter, distribuer ou vendre des copies de cette thèse sous la forme de microfiche/film, de reproduction sur papier ou sur format électronique.

The author retains ownership of the copyright in this thesis. Neither the thesis nor substantial extracts from it may be printed or otherwise reproduced without the author's permission.

L'auteur conserve la propriété du droit d'auteur qui protège cette thèse. Ni la thèse ni des extraits substantiels de celle-ci ne doivent être imprimés ou autrement reproduits sans son autorisation.

In compliance with the Canadian Privacy Act some supporting forms may have been removed from this thesis.

Conformément à la loi canadienne sur la protection de la vie privée, quelques formulaires secondaires ont été enlevés de cette thèse.

While these forms may be included in the document page count, their removal does not represent any loss of content from the thesis.

Bien que ces formulaires aient inclus dans la pagination, il n'y aura aucun contenu manquant.

Canada

Education is what survives when what has been learned has been forgotten.

B. F. Skinner

Dedicated to my parents

Madan Lal Kanda and Nirmal Kanda

Acknowledgements

The road to this thesis has been long and hard, as required. Given the conventionally lofty nature of personal acknowledgments, I shall endeavor to stay true to form. Towering above the fray amongst those to whom I feel indebted for assistance in having finally reached the conclusion of my graduate research, Professor Mark McDermott has been a cornerstone of my scientific evolution. In addition to being willing to lead by example, and possessing a savvy grasp of the science and politics in our field, has become a good friend in a way I suspect is rare among such supervisory figures. As I leave behind the group of which I have been a member for these many years, I can only hope I have had a fraction of the influence on this group as Mark has had on me in my development as a scientist and as a person.

When I first became a member of this group, we were a rather macho bunch, just beyond the primes of our lives. I'd like to thank the group members who graduated prior to me for their help and friendship, and with whom I had the honour of working: Michael Finot, James Kariuki, Gregory Kiema, Truong Ta, Mirwais Aktary and Solomon Ssenyange. I hope you guys all continue to achieve with your hard work and enthusiasm, and I look forward to another camping trip with you all. Ahem. To the present members of the group, Aaron Skelhorne, Francis Nsiah, Bushra Sajed, Chris Grant, Dwayne Shewchuk, and Rongbing Du, it was great working with all of you. I wish you nothing but the best as you strive to become more VK-like.

In completing my research, I had the pleasure of learning from various collaborators; Prof. D. R. Bundle, Pavel Kitov, and Soren Anderson were generous with

their time, expertise, and precious chemicals in the studies of carbohydrate interactions. Dimitre Karpuzov and Anqian He of the ACSES facility were of great help in the XPS studies of modified PDMS. I thank all of the Department of Chemistry technical staff; the NanoFab facility, and Dr. John-Bruce Green for helpful discussions and the use of his evaporator, ozone cleaner, plasma chamber and tools.

Having a life away from the lab was vital in helping me to maintain a sense of normalcy. Of course, people have lives away from work, but I am particularly grateful for the time I had to evolve friendships with these people. So thank you, George Colin, Brendan Alseth, Chris Pagett, Andrew Prasad, Rachelle and Crystal Andre, and Erin Brennan. All of whom are people on whom I have relied and who I have known to be true friends.

Lastly, I'd like to thank my wonderful family for their support and love throughout the years. They have raised me to be an inquirer and an analyst, and yet, how can I analyze the way each of them has sacrificed and toiled to afford me not only opportunities, but the ability to take advantage of them? I am not, nor have I ever been, the recipient of crude charity on the part of these two people; the dividends I reap are wholly due to the investments they made of themselves, in me. And without laborious qualifications regarding the nature of immortality and such existential tedium, or genetic even-more-tedium, I can say that I am each of my parents, and my successes are their victories. In addition, my brothers Suneil and Vikram have always been sources of inspiration for me. Being the oldest, and some would say best, son hasn't always been easy, but my brothers are the reason I can go anywhere and not feel alone.

Table of Contents

Chapter I: Introduction

Proteins at Interfaces	1
Microarray Analysis	6
Tailoring Surface Chemistry	8
Scanning Force Microscopy	11
Surface Plasmon Resonance Imaging	17
Research Objectives	20
References	22

Chapter II: Probing Surface Chemistry Induced Variations in Protein Films with Tapping-Mode Scanning Force Microscopy

Introduction	27
Experimental	29
Results and Discussion	31
Conclusions	55
References	56

Chapter III: Surface Plasmon Resonance Imaging of Protein Arrays

Introduction	60
Experimental	62
Results and Discussion	65
Conclusions	85
References	86

Chapter IV: Surface Plasmon Resonance Imaging of Protein-Carbohydrate

Interactions

Introduction	89
Experimental	92
Results and Discussion	94
Conclusions	118
References	120

Chapter V: Surface Chemical Modifications with Microfluidics

Introduction	123
Experimental	125
Results and Discussion	127
Conclusions	150
References	150

Chapter VI: Conclusions and Suggestions for Future Work

General Conclusions	154
Suggestions for Future Work	155
References	158

List of Tables

Table 2.1	IRRAS was performed on HFG films formed on complete monolayers of UDT and MUA. Native values from ref. 22.	39
Table 3.1	Curve-fitting parameters for anti-bIgG binding curves.	84
Table 4.1	Curve-fitting parameters for Se155-4 binding curves in Fig. 4.03	101
Table 4.2	Curve-fitting parameters for Se155-4 binding curves in Fig. 4.05	105
Table 4.3	Curve-fitting parameters SLT inhibition curves in Fig.s 4.11 and 4.12	116
Table 5.1	IRRAS peaks for MUA SAMs formed from aqueous micellar solutions of Tween 20.	133
Table 5.2	Atomic concentrations for native and modified PDMS samples.	143

List of Figures

Figure 1.01	Protein adsorbing at solid-liquid interface	3
Figure 1.02	Fibrinogen, immunoglobulin G, and albumin	4
Figure 1.03	Alkylthiolate monolayer formation on gold	10
Figure 1.04	Microcontact printing	12
Figure 1.05	Patterning via microfluidic channels	13
Figure 1.06	Scanning force microscopy	15
Figure 1.07	Phase signal in tapping-mode SFM	16
Figure 1.08	Force curve analysis	18
Figure 1.09	SPR imaging	21
Figure 2.01	Protein film disruption in contact-mode SFM	32
Figure 2.02	TM-SFM of HFG film on patterned SAM	34
Figure 2.03	IRRAS spectra of HFG on different SAMs	37
Figure 2.04	SPR sensorgrams of HFG on different SAMs	41
Figure 2.05	Examples of force curves for HFG on different SAMs	46
Figure 2.06	Histogram of pull-off forces for HFG on different SAMs	48
Figure 2.07	TM-SFM of BSA film on patterned SAM	50
Figure 2.08	High-resolution TM-SFM of HFG on MHA SAM	53
Figure 3.01	Patterning protein lines via microfluidic channels	66
Figure 3.02	SPR imaging sequence for a three protein line array	67
Figure 3.03	Image profiles showing changes upon antibody adsorption	69

Figure 3.04	Effect of BSA blocking on antibody capture	71
Figure 3.05	Patterning surface chemistry and proteins cross-wise via microfluidic channels	74
Figure 3.06	SPR images of antibody capture on three protein array	76
Figure 3.07	Line profiles for three protein array after gIgG adsorption	77
Figure 3.08	Line profile for three protein array after anti-BSA adsorption	79
Figure 3.09	Effect of surface antigen density on antibody binding	81
Figure 4.01	Structures of <i>Salmonella</i> epitopes	95
Figure 4.02	SPR imaging of Se155-4 binding to SMA-17 at different surface densities	96
Figure 4.03	Binding isotherms for Se155-4 against arrayed SMA-17	99
Figure 4.04	SPR imaging of Se155-4 binding to arrayed <i>Salmonella</i> epitopes at different surface densities	103
Figure 4.05	Binding isotherms for Se155-4 against arrayed <i>Salmonella</i> epitopes	104
Figure 4.06	Structure of Starfish (SF-2) ligand	106
Figure 4.07	Structure of Daisy ligand	107
Figure 4.08	Structures of P ^k and AGM ₂	109
Figure 4.09	SPR imaging of SLT binding to P ^k and AGM ₂	110
Figure 4.10	IRRAS study of SLT binding at different surface densities of P ^k	112
Figure 4.11	Inhibition of SLT binding with SF-2	114
Figure 4.12	Inhibition of SLT binding with Daisy	115

Figure 4.13	Comparison of ELISA protocols with SPR imaging protocol	119
Figure 5.01	SPR images of microcontact printed MUO	129
Figure 5.02	Infrared spectra of MUA SAMs formed from aqueous Tween 20	131
Figure 5.03	SPR images of MUA lines formed from Tween 20 solutions	134
Figure 5.04	XPS survey spectra for native and modified PDMS	138
Figure 5.05	High resolution XPS spectra for native and oxidized PDMS	139
Figure 5.06	XPS-determined atomic compositions change with plasma oxidation time	141
Figure 5.07	XPS-determined atomic compositions after silanization with TFS	142
Figure 5.08	SPR imaging of an ODT line array formed through PDMS[ox]-F microchannels	146
Figure 5.09	SPR imaging of an MHA line array formed through cleaned PDMS[ox]-F microchannels	149

List of Symbols

$\overline{P}_{\text{tip}}$	Power dissipated by tip-sample contact
k	Cantilever spring constant
ω_0	Resonance frequency of cantilever
A	Amplitude of oscillation
A_0	Amplitude of freely oscillating cantilever
Q_0	Quality factor
Φ	Phase angle
$\Delta\Phi$	Phase lag between cantilever tip and drive signal
$\Delta(\Delta\Phi)$	Difference in phase lags
θ	Fractional surface coverage
θ_i	Incident light angle
ν_{AI}	Stretching frequency of amide I band
$\nu_{\text{a}}(\text{CH}_2)$	Asymmetric Methylene C-H Stretch
$\nu_{\text{s}}(\text{CH}_2)$	Symmetric Methylene C-H Stretch
AI	Absorbance of amide I band
AII	Absorbance of amide II band
n	Refractive index
$\%R$	Reflected light intensity (reflectivity) as a percent of maximum
$\Delta\%R$	Change in percent reflectivity in difference image
I_{s}	Intensity of s-polarized light

I_p	Intensity of p-polarized light
K_d	Desorption coefficient
K_{ads}	Adsorption coefficient
[A]	Solution adsorbate concentration
IC_{50}	Concentration at which inhibition is half-maximal

List of Abbreviations

μ CP	Microcontact Printing
μ FC	Microfluidic Channel(s)
a.u.	Absorbance Units
AFM	Atomic Force Microscope/Microscopy
AIBN	Azobis(isobutyronitrile)
bIgG	Bovine Immunoglobulin G
BFG	Bovine Fibrinogen
BSA	Bovine Serum Albumin
CCD	Charge-Coupled Device
DNA	Deoxyribonucleic Acid
EG3-OMe	1-Mercaptoundec-11-yltri(ethylene glycol) methyl ether
ELISA	Enzyme-Linked Immunosorbent Assay
gIgG	Goat Immunoglobulin G
HFG	Human Fibrinogen
HRP	Horseradish Peroxidase
IgG	Immunoglobulin G
IRRAS	Infrared Reflectance Absorbance Spectroscopy
MAb	Monoclonal Antibody
MALDI	Matrix Assisted Laser Desorption Ionization
MHA	Mercaptohexadecanoic Acid
MP	Milk Protein

MS	Mass Spectrometry
MUA	Mercaptoundecanoic Acid
MUAM	Mercaptoundecylamine
MUO	Mercaptoundecanol
NMR	Nuclear Magnetic Resonance (Spectroscopy)
ODT	Octadecanethiol
OVA	Ovalbumin
PBS	Phosphate-Buffered Saline
PBS ^T	Phosphate-Buffered Saline with Tween 20
PDMS	Polydimethylsiloxane
PDMS[ox]	Oxidized Polydimethylsiloxane
PDMS[ox]-F	Oxidized Polydimethylsiloxane Silanized with TFS
RF	Radio Frequency
RIU	Reflected Intensity Units
RNA	Ribonucleic Acid
RU	Response Units
SA	Streptavidin
SAM	Self-Assembled Monolayer
SFM	Scanning Force Microscope/Microscopy
SDS	Sodium Dodecyl Sulphate
SLT	Shiga-Like Toxin
SPM	Scanning Probe Microscope/Microscopy
SPR	Surface Plasmon Resonance (Spectroscopy)

TFS	(Tridecafluoro-1,1,2,2-tetrahydrooctyl)-1-trichlorosilane
TLC	Thin Layer Chromatography
TMB	Tetramethylbenzidine
TM-SFM	Tapping-Mode Scanning Force Microscopy
UDT	Undecanethiol
XPS	X-Ray Photoelectron Spectroscopy

Chapter I

Introduction

1. Proteins at interfaces

The interfacial behaviour of proteins is commonly studied at the air/liquid, liquid/liquid, and solid/liquid boundaries. All of these interfaces include liquid phases since the native environment of proteins is liquid, including the fluid mosaic of cell membranes. Due to the varying hydrophobicity of amino acid side-chains and the folding of oligopeptides, proteins have segregated regions of similar hydrophobicity. A consequence of this amphipathic nature is a tendency to aggregate at interfacial regions where the hydration of hydrophobic protein domains can be minimized.^{1, 2} In this work, means of controlling surface chemistry were explored with a particular emphasis on protein adsorption due to the relevance of interfacial protein adsorption in various biotechnological applications.

If a given liquid system contains proteins, one can view the adsorption of proteins onto a foreign solid surface as the initial response of this system to the surface. Generally, proteins adsorb spontaneously to any solid surface to which they are exposed.¹ The lack of such adsorption inside living systems is due to passivation of the surfaces by species such as lipids and oligosaccharides, and by other proteins. This passivation facilitates the specialization of protein functions. The spontaneous adsorption of proteins to alien surfaces can be viewed as a passivation process by which the interfacial free

energy is minimized. In a multi-protein liquid, such as those in biological systems, the adsorption process starts with the adsorption of the most abundant proteins, which are eventually displaced by other proteins with higher affinities for the surface. This phenomenon has been termed the Vroman effect; Leo Vroman first discovered transient maxima in the immunoreactivity of adsorbed fibrinogen in the late 1960s.¹ In order to minimize the complications of multiprotein competition and adsorption, single-protein solutions were studied in this work. The use of single-protein solutions also allowed for the development of assays based on interactions of target proteins at surfaces. Figure 1.01 illustrates the adsorption process for a model protein.

Figure 1.02 introduces three proteins of particular interest; fibrinogen, immunoglobulin G (IgG), and albumin. Fibrinogen is important to studies of blood compatibility as it is not only a very large and notoriously surface-active protein, but it is present at concentrations of 2-4 mg/mL in human plasma. The high surface activity of fibrinogen is due to its large size (340 kDa) and flexible domains. It is known to adsorb so readily to a variety of surfaces that it is often used as a benchmark for testing surfaces for protein resistance.³⁻⁸ The structure of adsorbed fibrinogen molecules and fibrinogen films have been widely studied and shown to vary with the chemical properties of the substrate.⁹⁻¹⁴ The surface activity of fibrinogen is important to study, as adsorbed fibrinogen has been shown to mediate further reactions such as platelet binding and activation, as well as providing attachment sites for bacteria.¹⁵

IgGs (150 kDa) form the most abundant class of immunological recognition proteins in mammals (12.5 mg/mL in human blood). IgG is important technologically due to the wide use of IgG antibodies in a variety of applications requiring highly

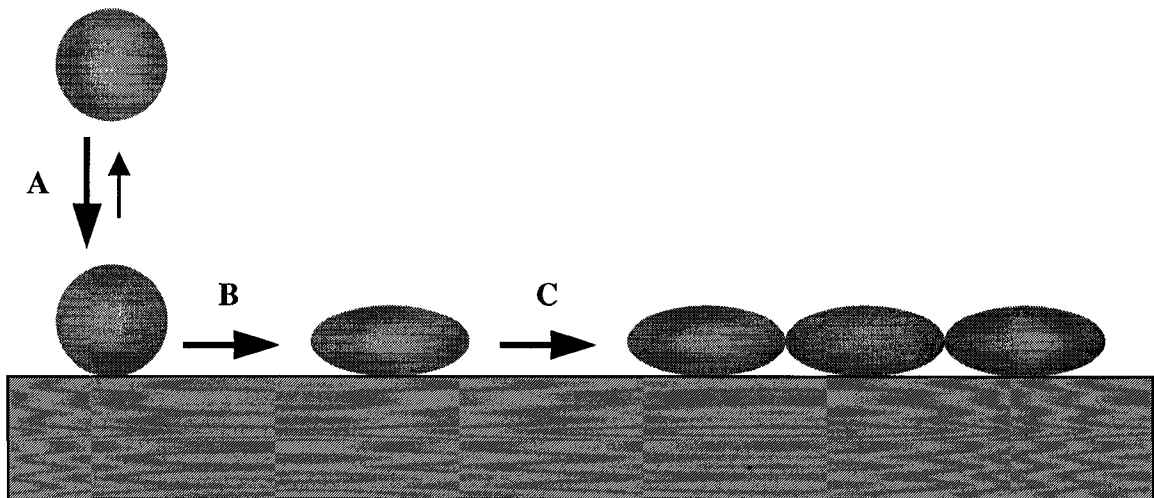


Figure 1.01. Steps in the formation of a protein film at the interface between a solid surface and a single-protein solution. (A) Adsorption/desorption of a protein. (B) Denaturation of adsorbed protein increases contact area with the surface. (C) Film formation, whereby surface protein concentration reaches an equilibrium value.

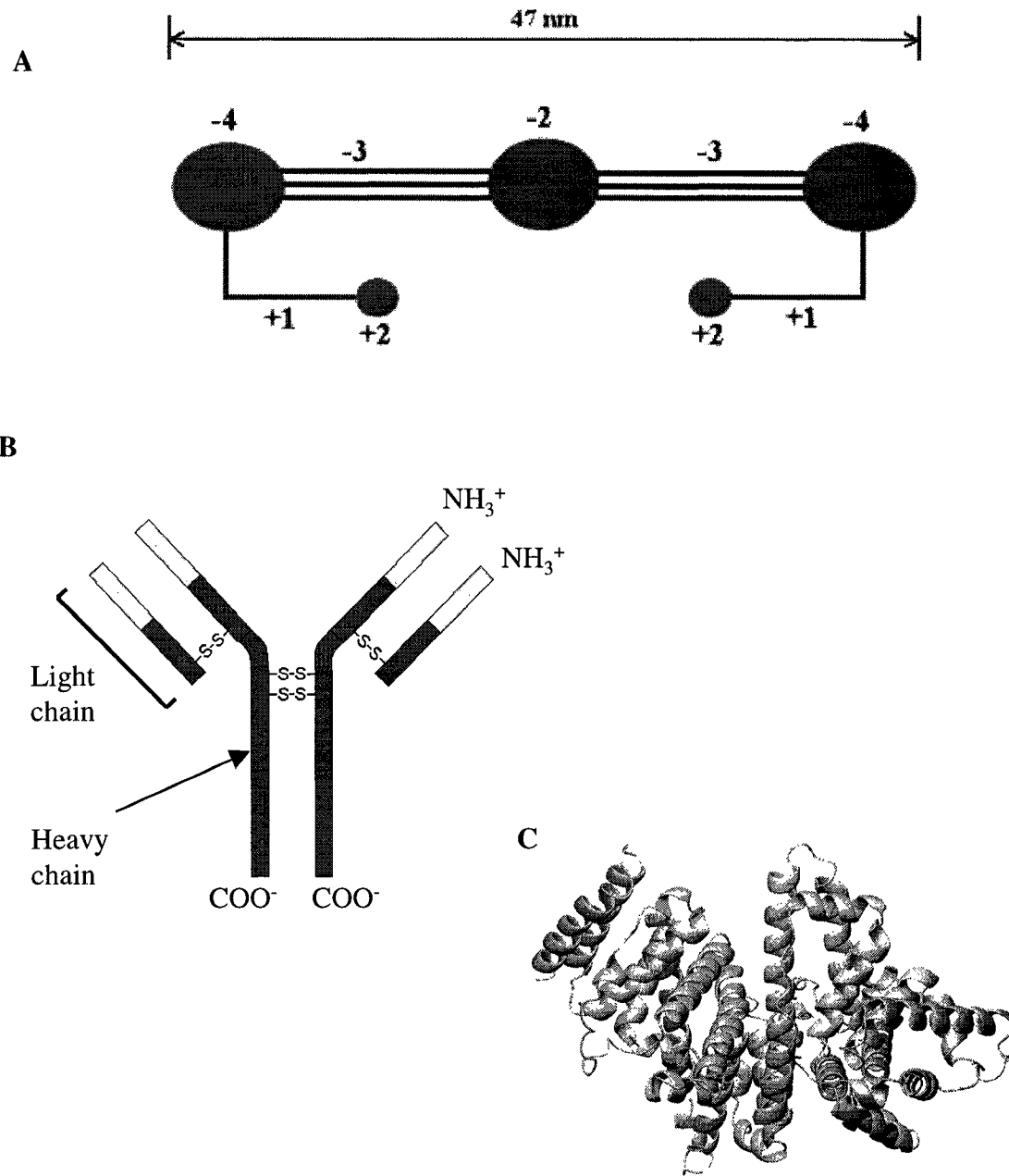


Figure 1.02. (A) Fibrinogen is an antiparallel dimer, each half of which is composed of three polypeptide chains. The structure is generally described as three major globular domains linked by helical coiled coils. Net charges on major domains are indicated. (B) Immunoglobulin G structurally contains two heavy chains and two light chains linked by disulphide bonds. In addition, there are two antigen binding regions (yellow) which are of variable sequence and structure. (C) Bovine serum albumin is an approximately heart-shaped globular molecule consisting of a single folded polypeptide chain.

selective and binding of targets. As shown in Fig. 1.02(B), IgG has two variable regions (yellow) which engage in binding interactions. Each of the variable regions of the heavy and light chains consists of three smaller loops of highly variable sequence. Together the six loops in the hypervariable region of the IgG molecule form an antigen binding site known as the complementarity determining region.¹⁶

Albumin is a globular molecule (66 kDa) which is known to have a high affinity for lipids and hydrophobic alkyl chains. The exposure of biomaterials to blood or blood plasma initially results in the formation of a layer of albumin due to its high abundance (40-50 mg/mL in human blood). This layer is then displaced by higher molecular weight species such as IgG and fibrinogen, which in turn may be eventually displaced by high molecular weight kininogen.

In the studies presented here, protein films are studied at intermediate adsorption times, typically on the order of tens or hundreds of minutes. After an initial adsorption and film formation, proteins can undergo further slow structural rearrangements on the order of days or weeks. The benefit of studying the initially formed films, trapped in a local free energy minimum, is that they can be probed after a short period in order to elucidate the properties of the initially formed film. Given the aforementioned Vroman effect, it is desirable to study the films formed initially upon exposure to the surface in order to elucidate properties which would typically have a transient existence. Physical phenomena of interest when studying protein adsorption generally include kinetic and thermodynamic parameters. Herein, the focus is on films that have formed to a degree of thermodynamic stability or equilibrium. The physical properties of such films may then be a subject of inquiry on the basis of variations in the underlying substrate. That is, the

manipulation of the properties of the solid adsorbent can be shown to influence the state of the equilibrium films.

The effects of the topology, chemistry, and flexibility (in the case of polymer films) of solid sorbents can be studied.¹⁷ It has been speculated and confirmed that the chemical nature of the biomaterial surface can influence the initial adsorption. In particular, the chemical functionality of the surface can dictate the strength and density of the binding, the adsorbed orientation of the biomolecules, conformational perturbations, and the formation of superstructures among the proteins. These factors influence the subsequent cavalcade of adsorbing proteins, platelets, and cells. Technologies which aim to exploit protein adsorption phenomena must take into account the effect of the surface chemistry. Indeed, surface chemistry seems to be a key factor in the manipulation of the interactions of proteins at interfaces.

2. Microarray Analysis

An important developing technology that depends on the immobilization of proteins is that of protein microarrays. Microscopic planar arrays of proteins or of ligands for protein binding are being developed as alternatives to traditional means of study such as ELISA or more instrumental methods such as NMR and MS due to the two major advantages of higher throughput and decreased sample consumption. Research in microarray technology has been pioneered as a response to the need for high throughput in the field of genomics. In the mid-to-late 1990s, there was a rapid increase in the proliferation of microarray analysis for the purpose of examining gene expression

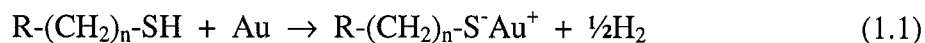
profiles, leading to the successful commercialization of genetic microarrays, or “gene-chips”.¹⁸ In general, arrays of this type are constructed on glass microscope slides by robotic pin-printers. Such devices create arrays by releasing small volumes of solution onto glass slides with controlled registry. In addition to the commercial availability of gene chips, it is possible to make custom gene chips via widely available pin-printing technology. Much of this technology is reliable due to the chemical simplicity and robustness of DNA. The extension of robotic pin-printing and fluorescence-based reading to protein arrays is not straightforward due to added complexities.

Because proteins can vary in their size, structural stability and chemistry, including post-translational modifications, not all proteins can be immobilized under the same conditions. Variations in surface activity and conformational stability among proteins can also lead to variations in reactivity changes among proteins and inhomogeneity within pin-printed spots. Homogeneity can be affected further in the preparation of pin-printed protein arrays due to the typically high concentrations buffer salts present in protein solutions. Because of the high surface-to-volume ratio of small spots, rapid drying typically follows deposition of protein spots. The resulting co-deposition of large amounts of buffer salts can affect the homogeneity within and among the spots. Yet another difficulty in applying gene-chip technology towards proteins is the relative scarcity of large libraries of proteins. While automated synthesis has been a key enabling technology in genomics research, no technology exists for the preparation of protein libraries on the same scale. In addition, while nucleotide chemistry benefits greatly from the amplification of small amounts of material via the polymerase chain reaction, there is no analogous technique for protein amplification. Thus, it remains a

challenge to produce and manipulate large numbers of proteins which may only be present in small quantities. The benefits of enhancements in this area would include increased ability to profile protein markers of disease. For example, it would be advantageous to be able to directly analyze protein expression patterns over numerous affected proteins since this would lead to more accurate disease profiling than reliance on only a single protein marker.¹⁹ One of the key limitations in the successful implementation of protein microarrays has been the establishment of a suitable surface chemistry for the global attachment of proteins.

3. Tailoring surface chemistry

Self-assembled monolayers (SAMs) represent a popular and heavily investigated means of creating a chemically well-defined surface. One of the most attractive systems over the past decade has been alkylthiolates adsorbed to a gold surface. Since the initial report of this type of monolayer,²⁰ there has been a wealth of detail uncovered regarding the structural characteristics of such systems. Alkylthiolate monolayers may be generated by simple gas-phase or solution exposure of a clean gold surface to a molecule containing a disulphide,²⁰ sulphhydryl (thiol),²¹ or thiosulphate²² moiety. While sulphides may also bind to gold, the resultant monolayers are not of the same quality as with the other groups.²³ Much research has been focused on monolayers formed by thiol-containing groups due to the speed of formation and high quality possible.^{21, 24-26} Although the exact chemical reaction taking place at the gold surface has remained something of a mystery, the generally postulated reaction scheme is²⁶



Monolayers formed by the spontaneous assembly of molecules of the type $\text{HS}(\text{CH}_2)_n\text{R}$, where R represents some functional group, have been shown to have a near-crystalline alkyl-chain packing density and order when $n \geq 12$.^{24, 27} In addition, the molecules align themselves in such a way as to present the terminal functionality, R , at the exposed surface of the monolayer (see Fig. 1.03). Disulphides have been shown to form monolayers of similar quality to those formed by thiols, but with slightly slower kinetics. As a result, the chemical functionality of a gold surface can be tailored by use of specific terminal functionalities. The usual way in which such monolayers are generated is to immerse gold into a solution, typically in an organic solvent such as ethanol or methanol, containing the desired alkylthiol. This technique coats the entire exposed surface with a monolayer film, creating polarized covalent bonds between the sulphur and the gold surface.²⁶

The technique of microcontact printing has also been demonstrated to create high quality alkylthiolate monolayers from simple alkylthiols (i.e. $\text{R}=\text{CH}_3$). In this technique, the alkylthiols are partitioned into a slab of poly(dimethylsiloxane) (PDMS) from solution. By pressing the slab against a gold surface, the alkylthiols are transferred rapidly to the surface and a high quality monolayer, reasonably free from defects, is formed in a matter of minutes or even seconds.^{28, 29} If a relief pattern is incorporated into the PDMS, then the monolayer is formed only in the regions of contact between the slab and the gold. In this way, a hydrophobic methyl-terminated monolayer can be generated

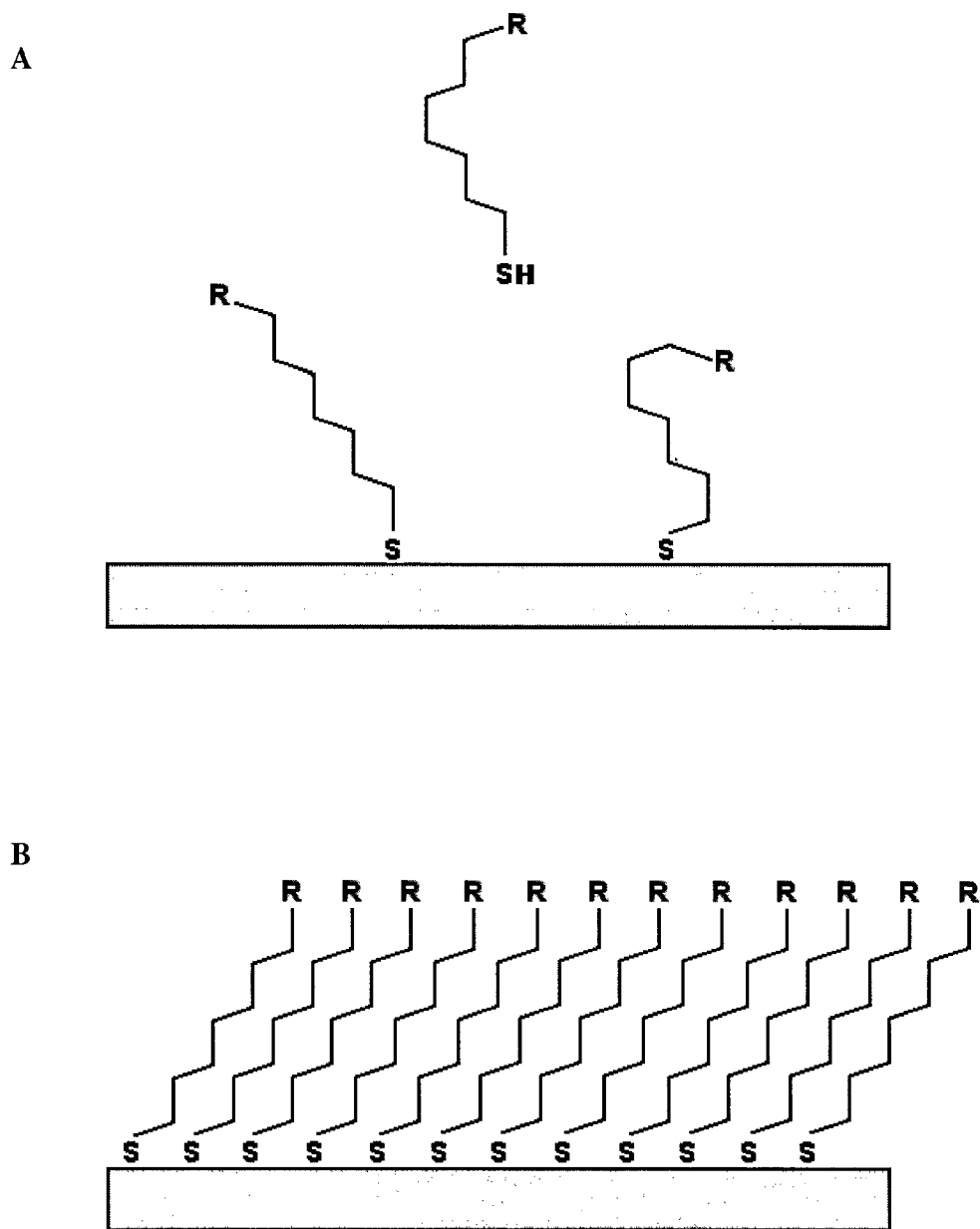


Figure 1.03. Monolayers of alkylthiolates form spontaneously upon exposure of a gold surface to a solution of alkylthiols. (A) Initial adsorption and bonding to the gold surface is rapid. (B) With time, defects are annealed and the alkyl chains align in all-trans configuration.

in a known spatial pattern. The unmodified areas, in which the PDMS was not contacting the gold, can then be further modified by simple immersion into an ethanolic solution of a second alkylthiol. The result of this procedure, outlined in Figure 1.04, is a chemically patterned gold surface with alternating chemical functionalities.

Another means of patterning any smooth surface is to place a surface in conformal contact with microfluidic channels through which adsorbates can be flowed over the surface (Fig. 1.05). Researchers at IBM in Zurich have shown the utility of PDMS microchannels for the patterning of proteins in line arrays.^{30, 31} In addition, by starting with a uniform surface coverage of a SAM with a reactive terminal group, line arrays can be created by flowing reactants over the reactive surface through PDMS microchannels. The research group of R. M. Corn has demonstrated this method for the production of line arrays of carbohydrates³² as well for localizing interactions between line arrays of peptide epitopes and antibodies flowed over the peptides via a second set of microchannels.³³ In addition to the chemical patterning of gold surfaces, the work in this thesis also explores methods for the analysis of surfaces.

4. Scanning Force Microscopy

The term scanning probe microscopy (SPM) describes a family of analytical techniques which involve raster-scanning a physical probe over a surface in order to generate a microscopic (or smaller) image of the surface. The atomic force microscope (AFM),³⁴ also referred to as the scanning force microscope (SFM), was used in this work

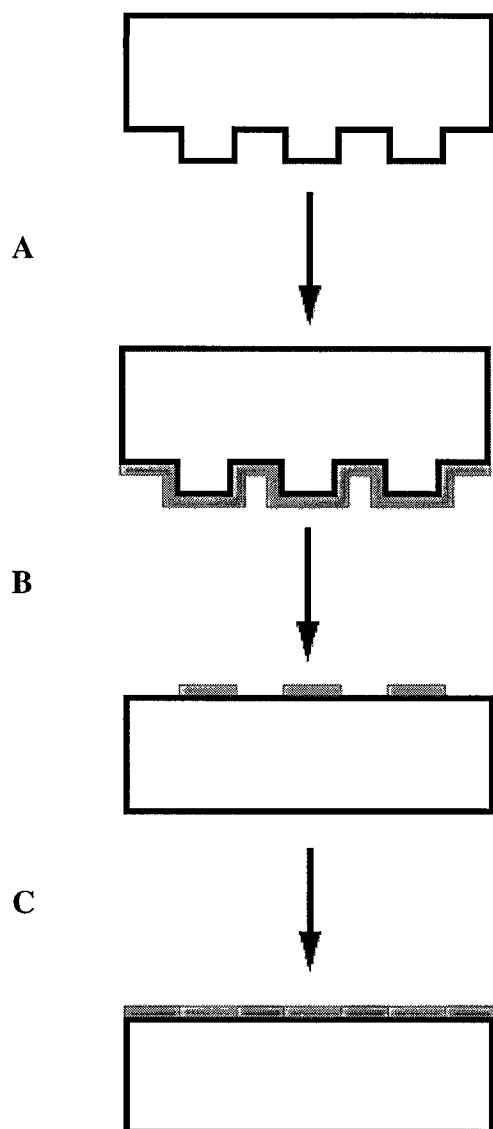


Figure 1.04. Surface chemistry patterning with microcontact printing. (A) Ink PDMS stamp with alkanethiol. (B) Pattern monolayer by placing stamp in conformal contact with gold substrate. (C) Remove stamp and place substrate in solution of a second thiolate-generating species to fill in bare gold regions.

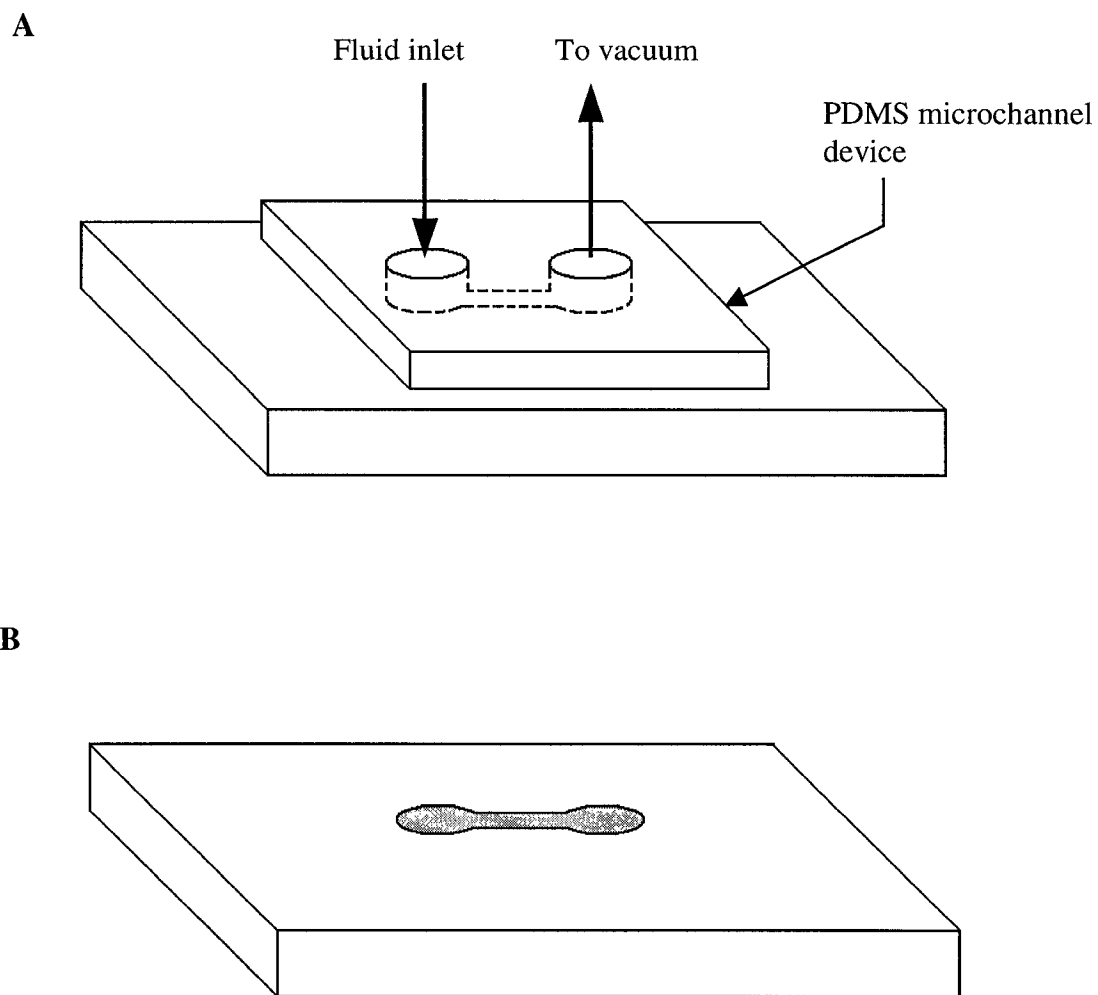


Figure 1.05. Surface patterning via microfluidic channels. (A) PDMS microchannels allow fluid to be introduced to a solid substrate in confined areas. (B) After a period of adsorption/reaction, only the surface area defined by the channel geometry is affected.

in order to generate several types of data. The abbreviation SFM shall be used to denote both the microscope and the process of scanning force microscopy in this work.

SFM can generate topographic images of a surface by tracking the vertical deflections of a stylus-like probe as it is scanned over a sample while maintaining constant tip-sample force (Fig. 1.06). The vertical deflections encountered as the probe encounters topographic variations inform a feedback loop to change the distance between the probe tip and the sample so as to maintain a constant contact force. The perturbations arising from the dragging of a solid probe over a sample surface are particularly problematic in the imaging of soft samples. Hence, in order to image biological samples with a lower degree of lateral, or shear, force, intermittent contact, or tapping-mode, means of imaging were developed.^{35, 36} In such a configuration, the same probe tip is oscillated vertically while scanning. The shear forces are greatly reduced due to the shorter contact times during lateral motion. Of course, this description neglects the effects of probe penetration into the sample and adhesion between the sample and probe, but does illustrate the general decrease in lateral forces when imaging in the tapping-mode.

A further benefit of tapping-mode SFM (TM-SFM) is the generation of an output waveform whose phase in relation to the input can vary with the interactions at the tip-sample contact (Fig. 1.07). It has been shown that the lag in phase between the probe and the input ($\Delta\Phi$) is a function of the energy dissipated by the tip-sample interaction.^{37, 38} For a sinusoidally driven cantilever at its resonance frequency (ω_0) with a typically high

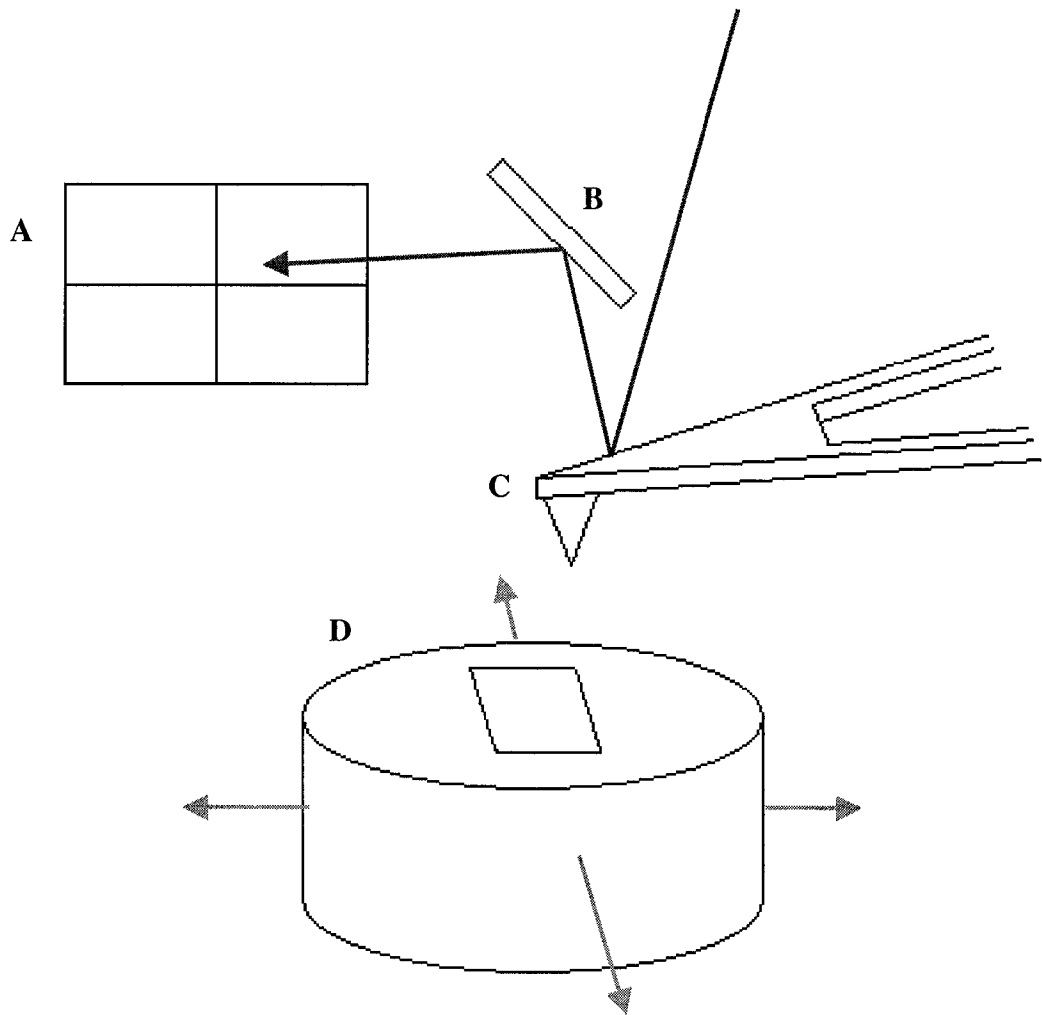


Figure 1.06. Schematic diagram of scanning force microscope. Red arrow indicates laser light path; green arrows indicate scanner tube motion. (A) Photodiode detector. (B) Mirror. (C) Cantilever probe. (D) Scanner tube with sample.

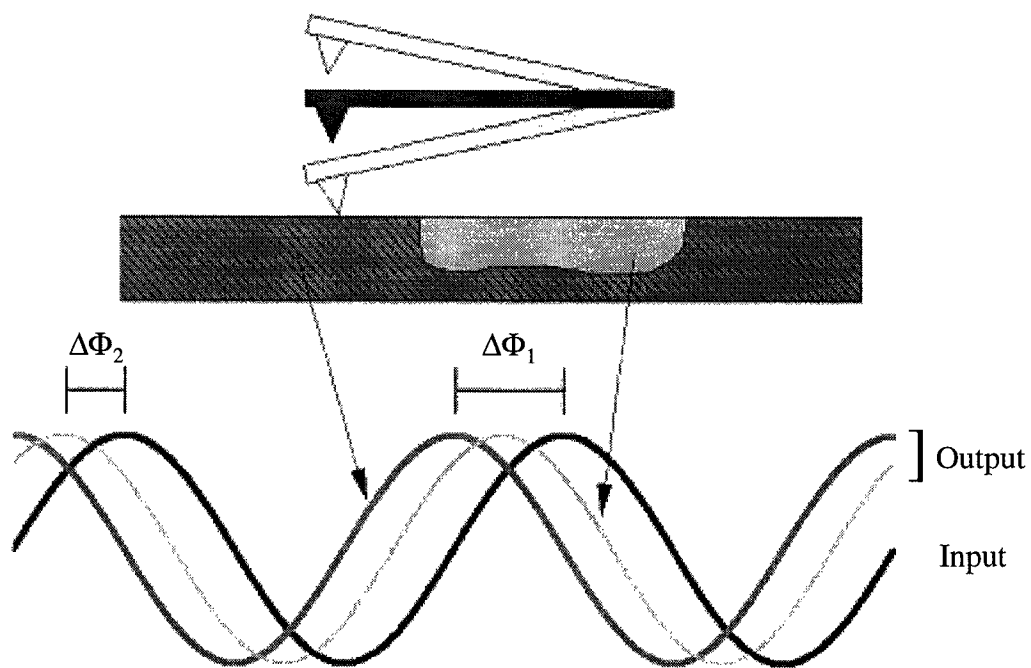


Figure 1.07. Tapping-mode AFM involves oscillating the cantilever probe while scanning. The phase lag ($\Delta\Phi$) of the measured oscillation relative to the input waveform depends on the interactions with the surface.

quality factor ($Q_0 \gg 1$), the power dissipated by tip-sample contact over one oscillation ($\overline{P_{ip}}$) can be obtained by the equation

$$\overline{P_{ip}} = \frac{kA^2\omega_0}{2Q_0} \left[\left(\frac{A_0}{A} \right) \sin(\Delta\Phi) - 1 \right] \quad (1.2)$$

where A is the oscillation amplitude, A_0 is the free oscillation amplitude of the non-interacting cantilever probe, and k is the spring constant of the cantilever. Thus, it is possible to relate the phase lag of the damped oscillation to the energy lost by the tip-sample interaction. Given that the dissipation processes may vary over a heterogeneous sample, the phase lag can be used to generate an image, simultaneous to the topographic image, of the energy dissipation over the surface.

In addition to scanning, the SFM probe can be held in a fixed lateral position and oscillated vertically. This operational mode is used to generate graphs of applied force versus tip-sample separation distance. Such graphs, known as force curves, can illuminate several additional properties of a surface. Figure 1.08 illustrates the steps in the generation of force curves.

5. Surface Plasmon Resonance Imaging

Surface plasmon resonance (SPR) is an optical phenomenon which can be used to probe adsorption at the interface between a metal film and a liquid or gas. Surface plasmons are standing evanescent waves which decay in intensity exponentially into the

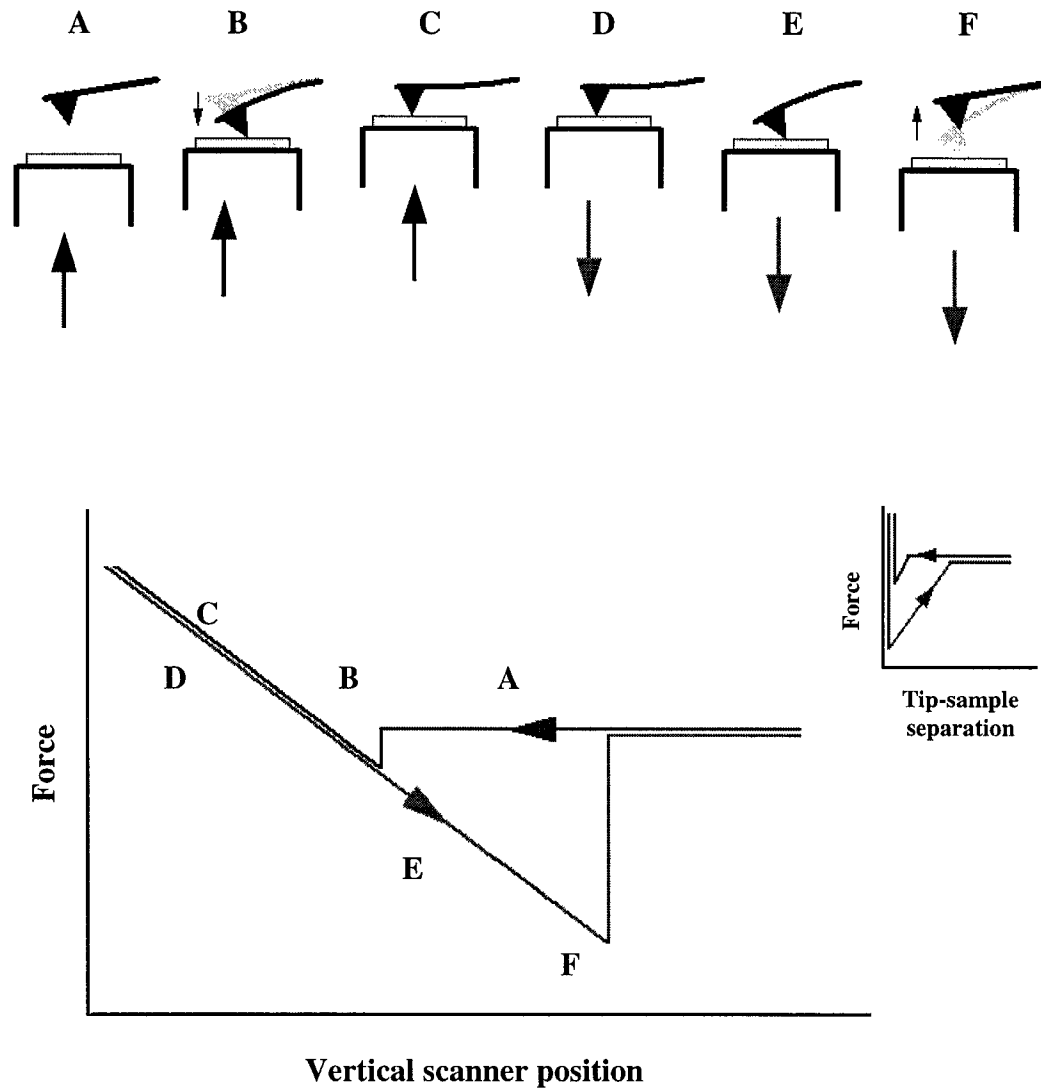


Figure 1.08. Force curves trace the deflection of the cantilevered probe as it approaches and retracts from a surface. (A) Sample approaches cantilever. (B) Probe tip snaps into contact with sample. (C, D) Cantilever bends against sample. (E) Adhesion to sample causes probe tip to bend lower than the original position. (F) As sample continues to retract, probe tip snaps out of contact. Graph inset shows how the same data can be plotted as a graph of force against tip-sample separation.

adjacent medium.^{39, 40} The effect results when a p-polarized beam of light is shone on a metal film at the rear surface of a prism or grating. At certain conditions of incident angle and wavelength the incoming photon energies are coupled to electrical oscillations in the plane of the metal film, resulting in attenuation of the reflected light. The angle and wavelength at which this occurs depends on the refractive index of the medium within a few hundred nm from the metal surface.⁴⁰ The SPR phenomenon is very sensitive to changes in refractive index within the surface region penetrated by the evanescent field and, hence, can be used to monitor adsorption at the metal surface. The equation describing the dispersion relation for a surface plasmon is as follows:

$$k_p = \frac{\omega}{c} \sqrt{\frac{\epsilon_d \times \epsilon_m}{(\epsilon_d + \epsilon_m)}} \quad (1.3)$$

where k_p represents the plasmon wave vector, ω is the oscillation frequency, c is the speed of light in vacuum, ϵ_m is the dielectric constant of the metal film, ϵ_d is the dielectric constant of the dielectric medium adjacent to the metal film.³⁹

Typically, one may expect to undertake a chemical reaction and separation procedure in order to impart an adsorbate with a measurable secondary characteristic, especially in the case of biomolecular binding studies. This type of labelling may allow sensitive detection by fluorescence if the label used is an organic chromophore⁴¹⁻⁴³ or a nanoparticle.^{44, 45} A problem with such labelling procedures is the possible change in binding activity of the labelled proteins due to the introduction of an extra component, whether or not the actual recognition site is directly affected. One of the strengths of the

SPR technique is that, by relying on changes in refractive index caused by the addition of mass at the solid-fluid interface, the labelling of binding partners is avoided.

Figure 1.09 describes the experimental set up for SPR imaging. The standard configuration for SPR, employed by the popular Biacore instrument, involves measuring reflected intensity of polarized monochromatic light over a photodiode array in order to determine the angular shift in the minimum intensity. In the SPR imaging configuration, a polarized white light source is used, and an interference filter selects a wavelength band for collection by a CCD camera. The angle of observation is also fixed, resulting in the observation of changes in light intensity from the metal film surface with adsorption or desorption. By imaging the surface in this way, it is possible to design sensor surfaces as arrays and capture numerous interactions in parallel. This configuration is advantageous for examining binding selectivity and maximizing throughput while minimizing the amount of binding material needed to study each interaction.

6. Research Objectives

The research presented herein is focused on the study of proteins at solid/liquid interfaces and the manipulation of surfaces for patterning and analysis. Interfacial protein behaviour is important to studies of implantable biomaterials, biosensors, separations and purifications. In other words, the behaviour of proteins at solid surfaces in contact with biological fluids is of salient technological relevance. Two examples of applied research areas in which the interfacial activity of proteins is a crucial consideration are prevention of fouling in the food production industry and minimizing

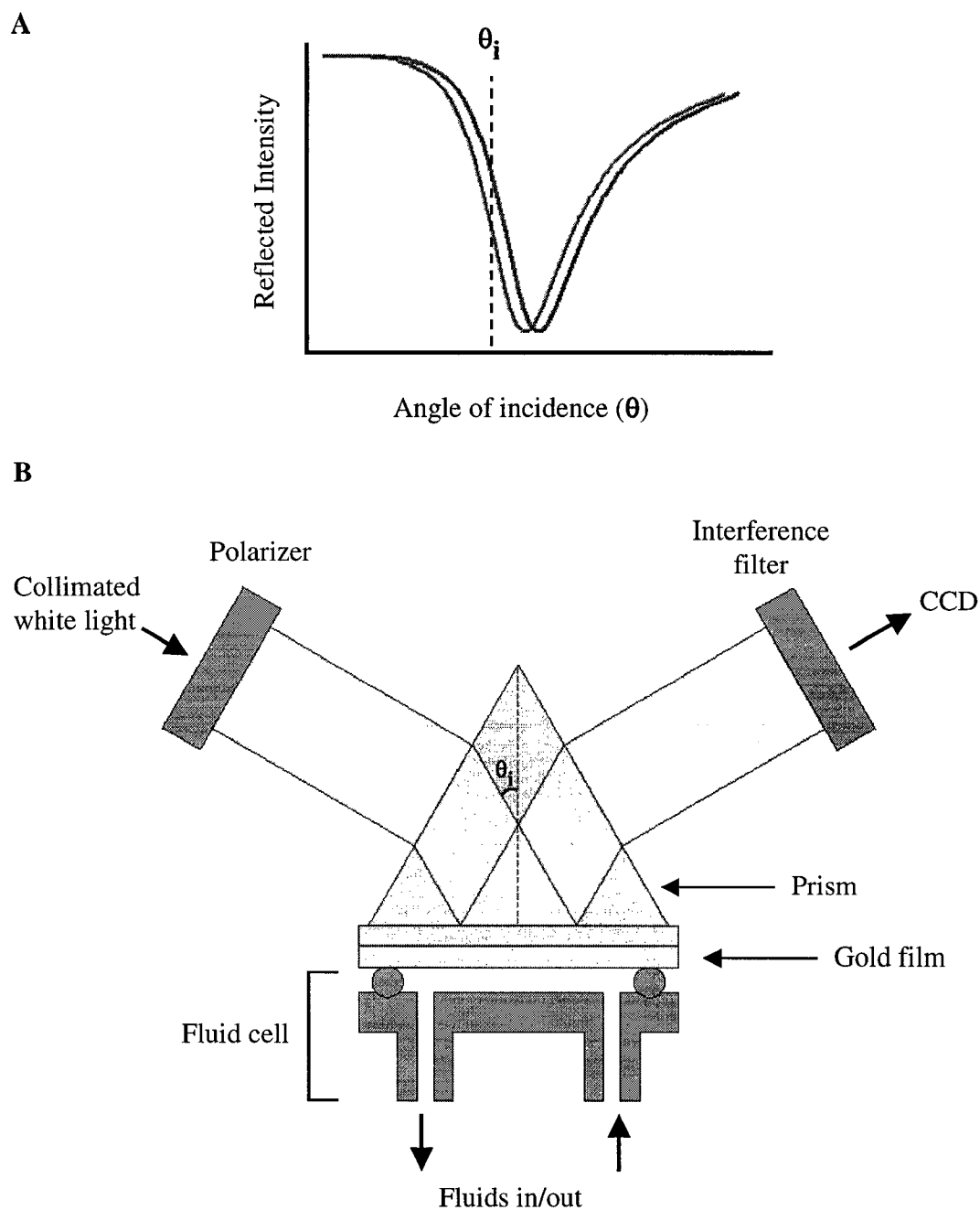


Figure 1.09. (A) The light reflected from a gold film is attenuated most strongly at a particular incidence angle of light θ_i . The angle at which the minimum occurs shifts with the adsorption of material at the solution interface of the film. The dashed line illustrates the increase in intensity upon such a shift when viewing the surface at a constant angle. (B) A schematic representation of a surface plasmon resonance imager.

the hostile response of bodily tissues to xenobiotic implants. Due to the importance of protein adsorption phenomena at solid-liquid interfaces, there is a need for analytical techniques which can probe such interfaces. The development of surface analytical techniques for the analysis of proteins at solid/liquid interfaces was a key motivation of this work. The examples of scanning probe microscopy and surface plasmon resonance presented in this work will illuminate the state of the art in such analyses.

In addition, surface preparation strategies were developed so as to provide reliable means for patterning and studying surface chemistry and protein adsorption. The strategies presented herein, and their application to microarray analysis, represent scientific advances enabling studies over a broad cross-section of biomolecular interactions.

7. References

- (1) Brash, J. L.; Horbett, T. A. In *Proteins at Interfaces II: Fundamentals and Applications*; Horbett, T. A., Brash, J. L., Eds.; American Chemical Society: Washington, D. C., 1995, pp 1-23.
- (2) Norde, W.; Haynes, C. A. In *Interfacial Phenomena and Bioproducts*, 1 ed.; Brash, J. L., Wojciechowski, P. W., Eds.; Marcel Dekker, Inc.: New York, 1996; Vol. 23, pp 123-144.
- (3) Feldman, K.; Hahner, G.; Spencer, N. D.; Harder, P.; Grunze, M. *J. Am. Chem. Soc.* **1999**, *121*, 10134-10141.

- (4) Chapman, R. G.; Ostuni, E.; Takayama, S.; Holmlin, R. E.; Yan, L.; Whitesides, G. M. *J. Am. Chem. Soc.* **2000**, *122*, 8303-8304.
- (5) Luk, Y.-Y.; Kato, M.; Mrksich, M. *Langmuir* **2000**, *16*, 9604-9608.
- (6) Huang, N.-P.; Michel, R.; Voros, J.; Textor, M.; Hofer, R.; Rossi, A.; Elbert, D. L.; Hubbell, J. A.; Spencer, N. D. *Langmuir* **2001**, *17*, 489-498.
- (7) Tegoulia, V. A.; Rao, W.; Kalambur, A. T.; Rabolt, J. F.; Cooper, S. L. *Langmuir* **2001**, *17*, 4396-4404.
- (8) Ostuni, E.; Chapman, R. G.; Holmlin, R. E.; Takayama, S.; Whitesides, G. M. *Langmuir* **2001**, *17*, 5605-5620.
- (9) Ta, T. C.; Sykes, M. T.; McDermott, M. T. *Langmuir* **1998**, *14*, 2435-3443.
- (10) Sit, P. S.; Marchant, R. E. *Thromb. Haemost.* **1999**, *82*, 1053-1060.
- (11) Ta, T. C.; McDermott, M. T. *Anal. Chem.* **2000**, *72*, 2627-2634.
- (12) Wertz, C. F.; Santore, M. M. *Langmuir* **2001**, *17*, 3006-3016.
- (13) Wertz, C. F.; Santore, M. M. *Langmuir* **2002**, *18*, 706-715.
- (14) Bergkvist, M.; Carlsson, J.; Oscarsson, S. *J. Biomed. Mater. Res.* **2003**, *64A*, 349-356.
- (15) Feng, L.; Andrade, J. D. In *Proteins at Interfaces II: Fundamentals and Applications*; Horbett, T. A., Brash, J. L., Eds.; American Chemical Society: Washington, D. C., 1995, pp 66-79.
- (16) Liddell, E. In *The Immunoassay Handbook*, 2nd ed.; Wild, D., Ed.; Nature Publishing Group: New York, 2001, pp 118-139.

- (17) Wojciechowski, P. W.; Brash, J. L. In *Interfacial Phenomena and Bioproducts*; Brash, J. L., Wojciechowski, P. W., Eds.; Marcel Dekker: New York, NY, 1996, pp 1-18.
- (18) Schena, M. *Microarray Analysis*; John Wiley & Sons, Inc.: Hoboken, NJ, 2003.
- (19) Wilson, D. S.; Nock, S. *Angew. Chem. Int. Ed.* **2003**, *42*, 494-500.
- (20) Nuzzo, R. G.; Allara, D. L. *J. Am. Chem. Soc.* **1983**, *105*, 4481-4483.
- (21) Bain, C. D.; Troughton, E. B.; Tao, Y.-T.; Evall, J.; Whitesides, G. M.; Nuzzo, R. *J. Am. Chem. Soc.* **1989**, *111*, 321-335.
- (22) Lukkari, J.; Meretoja, M.; Kartio, I.; Laajalehto, K.; Rajamaki, M.; Lindstrom, M.; Kankare, J. *Langmuir* **1999**, *15*, 3529-3537.
- (23) Jung, C.; Dannenberger, O.; Xu, Y.; Buck, M.; Grunze, M. *Langmuir* **1998**, *14*.
- (24) Porter, M. D.; Bright, T. B.; Allara, D. L.; Chidsey, C. E. D. *J. Am. Chem. Soc.* **1987**, *109*, 3559-3568.
- (25) Widrig, C. A.; Alves, C. A.; Porter, M. D. *J. Am. Chem. Soc.* **1991**, *113*, 2805-2810.
- (26) Sellers, H.; Ulman, A.; Shnidman, Y.; Eilers, J. E. *J. Am. Chem. Soc.* **1993**, *113*, 9389-9401.
- (27) McDermott, M. T.; Green, J.-B. D.; Porter, M. D. *Langmuir* **1997**, *13*, 2504-2510.
- (28) Xia, Y.; Whitesides, G. M. *Angew. Chem. Int. Ed.* **1998**, *37*, 550-575.
- (29) Eberhardt, A. S.; Nyquist, R. M.; Parikh, A., N.; Zawodzinski, T.; Swanson, B. I. *Langmuir* **1999**, *15*, 1595-1598.
- (30) Delamarche, E.; Bernard, A.; Schmid, H.; Michel, B.; Biebuyck, H. *Science* **1997**, *276*, 779-781.

- (31) Delamarche, E.; Bernard, A.; Schmid, H.; Bietsch, A.; Michel, B.; Biebuyck, H. *J. Am. Chem. Soc.* **1998**, *120*, 500-508.
- (32) Smith, E. A.; Thomas, W. D.; Kiessling, L. L.; Corn, R. M. *J. Am. Chem. Soc.* **2003**, *125*, 6140-6148.
- (33) Wegner, G. J.; Lee, H.-J.; Corn, R. M. *Anal. Chem.* **2002**, *74*, 5161-5168.
- (34) Binnig, G.; Quate, C. F.; Gerber, C. *Phys. Rev. Lett.* **1986**, *56*, 930-933.
- (35) Zhong, Q.; Inniss, D.; Kjoller, K.; Elings, V. B. *Surf. Sci. Lett.* **1993**, *290*, L688-L692.
- (36) Hansma, P. K.; Cleveland, J. P.; Radmacher, M.; Walters, D. A.; Hillner, P. E.; Bezanilla, M.; Fritz, M.; Vie, D.; Hansma, H. G.; Prater, C. B.; Massie, J.; Fukunaga, L.; Gurley, J.; Elings, V. *Appl. Phys. Lett.* **1994**, *64*, 1738-1740.
- (37) Cleveland, J. P.; Anczykowski, B.; Schmid, A. E.; Elings, V. B. *Appl. Phys. Lett.* **1998**, *72*, 2613-2615.
- (38) Anczykowski, B.; Gotsmann, B.; Fuchs, H.; Cleveland, J. P.; Elings, V. B. *Appl. Surf. Sci.* **1999**, *140*, 376-382.
- (39) Knoll, W. *Annu. Rev. Phys. Chem.* **1998**, *49*, 569-638.
- (40) Brockman, J. M.; Nelson, B. P.; Corn, R. M. *Annu. Rev. Phys. Chem.* **2000**, *51*, 41-63.
- (41) MacBeath, G.; Schreiber, S. L. *Science* **2000**, *289*, 1760-1763.
- (42) Sapsford, K. E.; Charles, P. T.; Patterson Jr., C. H.; Ligler, F. S. *Anal. Chem.* **2002**, *74*, 1061-1068.
- (43) Angenendt, P.; Glokler, J.; Sobek, J.; Lehrach, H.; Cahill, D. J. *J. Chrom. A* **2003**, *1009*, 97-104.

- (44) Chan, W. C. W.; Nie, S. *Science* **1998**, *281*, 2016-2018.
- (45) Schultz, S.; Smith, D. R.; Mock, J. J.; Schultz, D. A. *Proc. Natl. Acad. Sci. USA* **2000**, *97*, 996-1001

Chapter II

Probing Surface Chemistry Induced Variations in Protein Films with Tapping-Mode Scanning Force Microscopy

1. Introduction

The ability to directly observe the effects of substrate chemistry upon protein film properties is of potential interest to studies involving protein patterning and, more generally, the exposure of materials to biological fluids. The spontaneous adsorption of proteins to a biomaterial is the initial response of a biological system and can influence further responses of the system toward the “foreign” matter.¹ The work presented in this chapter describes an effort to characterize properties, including conformational rearrangements, of proteins adsorbing at interfaces. Previously, it has been shown that lateral-force SFM is able to map differences in the frictional properties of protein films adsorbed to alkylthiolate monolayers on gold.² The frictional contrast was attributed to differences in adsorbed conformational states. An important caveat to this interpretation, however, is that the attribution of the image contrast to conformational differences is in itself somewhat complicated and begs some consideration.

Fibrinogen so readily adsorbs at the solid-liquid interface that it is a commonly used probe for protein-resistance in biomaterials science.³⁻⁵ The large size (340 kDa) and well-characterized domain structure indicate that the molecule incorporates a large amount of water, ~33% by volume,⁶ in its native structure. The expulsion of some of this

water would be a significant entropic driving force for adsorption at the solid-liquid interface.^{7, 8} Given that proteins are well known to change structurally to maximize hydrophobic contacts upon adsorption, the degree of structural alteration would can vary with the hydrophobicity of the surface. In addition, it is possible for a protein to orient itself in a manner such that the more hydrophobic regions of the molecule would be more hidden from the aqueous phase. These factors have been the underpinnings of the paradigmatic association of increased sorbent hydrophobicity with greater protein binding strength.⁸ While the adsorption of protein species can be approached at the level of single molecules, fibrinogen has been shown explicitly to exhibit lateral intermolecular interactions at solid-liquid interfaces.⁹ In considering applications to biomaterials research, it is somewhat more useful to consider a complete film rather than isolated molecules when attempting to assess the ensemble properties such formations may possess.

In situ tapping-mode scanning force microscopy (TM-SFM) is a powerful and relatively non-destructive means of imaging adsorbed proteins.^{10, 11} By comparison, contact mode SFM is not well-suited for weakly bound protein films, which may be displaced or distorted by the probe tip. In addition, many real biomaterials exhibit a rough topography that will contribute to lateral shearing or frictional forces. These limitations provide the motivation to use TM-SFM as a tool for the analysis of adsorbed proteins. The lower lateral interactions between the tip and surface in TM-SFM reduce tip-induced conformational changes and/or displacement of adsorbed species. In addition, TM-SFM is able to generate compositionally sensitive phase images in the presence of large topographic variations.¹²

It has been shown that the phase lag ($\Delta\Phi$) of an oscillating cantilever in TM-SFM depends on the energy dissipated during tip-sample contact¹³⁻¹⁵ and is, therefore, sensitive to the surface composition of the sample. Phase imaging is able to differentiate bilayer structures with chemical sensitivity based on the functional groups presented at the interface, indicating the sensitivity of the phase lag towards surface chemistry.¹² In addition, differences in mechanical properties such as viscoelasticity and elasticity have been shown to contribute to the generation of phase contrast.^{15, 16} Holland and Marchant have demonstrated the utility of phase imaging for the observation of segregated protein molecules on standard reference biomaterials.¹⁷ In this chapter, the ability of phase contrast TM-SFM to map conformational variations of proteins in complete protein films is demonstrated. This result potentially extends the utility of SFM in the characterization of biomaterials and the study of ensemble properties of protein films.

2. Experimental

All aqueous solutions were prepared using water from a Nanopure purification system (Barnstead, Dubuque, IA). Fraction I, 95% clottable human fibrinogen (HFG), bovine fibrinogen (BFG) and bovine serum albumin (BSA) were obtained from Sigma (St. Louis, MO). All protein solutions were prepared by weight in 1 mM phosphate-buffered saline (PBS; 0.2 mM KH_2PO_4 , 0.8 mM Na_2PO_4 , 10 mM NaCl, 1 mM KCl) at pH 7.4 and filtered through a 0.22 μm low-protein binding filter (Millex-GV; Millipore, Bedford, MA).

Octadecanethiol (ODT), undecanethiol (UDT), and 16-mercaptohexadecanoic acid (MHA) were obtained from Aldrich and used as received, with the exception of ODT, which was recrystallized from acetone. 11-Mercaptoundecanoic acid (MUA) was synthesized in accordance with published procedure:¹⁸ 11-bromoundecanoic acid (Aldrich) was refluxed in water with a slight excess of thiourea for several hours before adding two equivalents NaOH and refluxing a few further hours. The mixture was acidified using HCl, taken up in toluene and concentrated by rotary evaporation. The resulting MUA was purified by flash chromatography on silica gel with 3% MeOH in CH₂Cl₂ as eluent.

Substrates for SPM imaging were prepared by sputter coating 40 nm of Au on to Ti-primed silicon. Higher resolution images were obtained using H₂-flame annealed gold (300 nm thickness) on Tempax glass (Berliner Glass).¹² Deposition of self-assembled monolayers (SAMs) was effected by immersion of a gold substrate into 1 mM ethanolic solutions of a given alkylthiol for at least 1 h. For patterned surfaces, polydimethylsiloxane (PDMS) stamps were soaked in 1 mM ethanolic ODT for 1-2 min., rinsed with ethanol and dried under argon prior to contact with the substrate for 1-2 min. Subsequent self-assembly of MHA was carried out by immersion of the substrate in a 1 mM ethanolic solution of MHA. Images were obtained using a Digital Instruments Nanoscope IIIa with Extender module for phase imaging. Silicon nitride cantilevers (NanoProbes, Digital Instruments, Santa Barbara, CA) with nominal spring constants of 0.06 and 0.58 N/m were used for both tapping-mode and contact-mode imaging in a Digital Instruments fluid cell; all images were obtained under PBS. Tapping-mode images were collected at 20-50% of free oscillation amplitudes. For force-distance

analysis, cantilever probes were coated with 40 nm Au (10 nm Ti adhesion layer) by thermal evaporation and further modified with a monolayer of 1-(mercaptoundec-11-yl)tri(ethylene glycol) methyl ether (EG3-OMe; gift from Prof. G. M. Whitesides, Harvard University). Force-distance curves were collected at vertical scan rates of ~1 Hz.

Infrared reflectance absorbance spectroscopy (IRRAS) was performed on a Mattson Infinity spectrometer with an externally housed low noise MCT-A detector. Spectra were generated from 500 scans at 2 cm⁻¹ resolution. Substrates were glass slides coated with 10 nm Ti for adhesion and 300 nm Au.

SPR sensorgrams were obtained on a Biacore 2000 instrument (Biacore, Uppsala, Sweden). Bare gold sensor chips from Biacore were modified with either ODT or MHA SAMs. All solutions were deaerated and filtered in order to prevent the distortion of sensorgram signals by particulates or air bubbles. Four analysis channels were run separately per sensor chip and the results averaged for each experiment.

3. Results and Discussion

3.1. Phase imaging of HFG films

Substrates exhibiting segregated chemical domains were employed to observe and compare the effects of surface chemistry on protein adsorption within a single image. Figure 2.01 provides an example of the kind of perturbation that can be caused by scanning a protein film while a constant force load is maintained between the probe tip and the film. Figure 2.01(A) shows a BFG film deposited on a patterned ODT/MHA

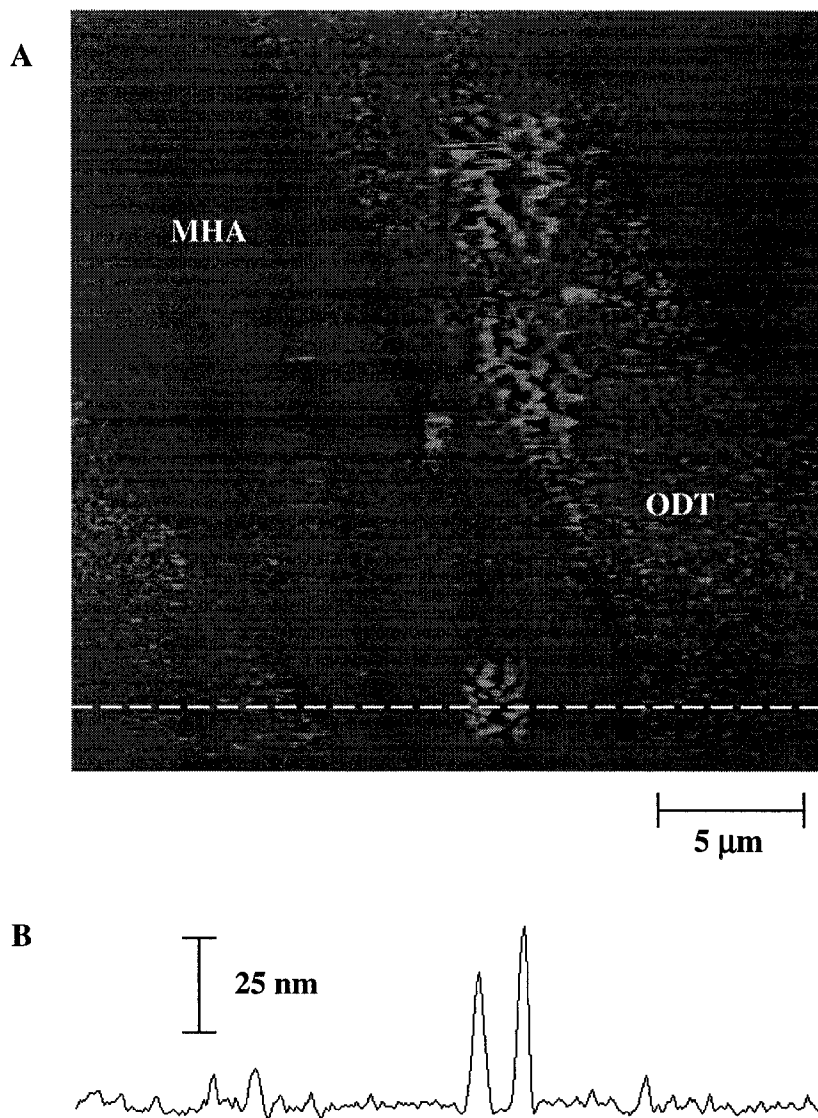


Figure 2.01. Distortion of protein patterns by lateral scanning of probe tip in contact mode SFM.

SAM from a 20 $\mu\text{g/mL}$ solution. Several smaller scans at various loads had already been performed over parts of the surface. The square regions indicate locations at which a higher load force had been applied during scanning. The line profile in Fig. 2.01(B) provides a measurement of the topographic changes. The lateral scanning of the probe at high normal forces had resulted in the formation of protein aggregates with heights on the order of tens of nanometres. It can be seen quite easily using such a perturbation that there is protein adsorbed to both monolayers.

While the use of contact-mode SFM has been shown to be effective in elucidating differences in properties between protein films on different chemical surfaces, TM-SFM was known to cause less sample perturbation. The use of imaging by monitoring the phase lag in the oscillating cantilever, or phase imaging, was thought to be able to illuminate additional physical properties of the protein films. Figure 2.02 contains topographic and phase images of a patterned ODT/MHA SAM before and after exposure to HFG. The $30 \times 30 \mu\text{m}^2$ topographic image in Fig. 2.02(A) indicates little difference between the ODT and MHA monolayers, which are expected to differ by only ~ 0.3 nm. Figure 2.02(B) shows the corresponding phase image. The darker contrast on the methyl-terminated ODT regions corresponds to greater phase lag ($\Delta\Phi$) indicating greater tip-sample energy dissipation than on the carboxylate surface.^{14, 15, 19} The differences in $\Delta\Phi$ (i.e. $\Delta(\Delta\Phi)$) observed between patterned regions in Figure 2.02(B), approximately 10° as measured by the cross-sectional profile (inset), can be attributed predominantly to surface chemistry. It has been demonstrated that mechanical differences are negligible for alkyl chains longer than 10 methylene units, such as those involved in this study.²⁰ Our analysis of force-distance curves consistently reveals a higher adhesion hysteresis

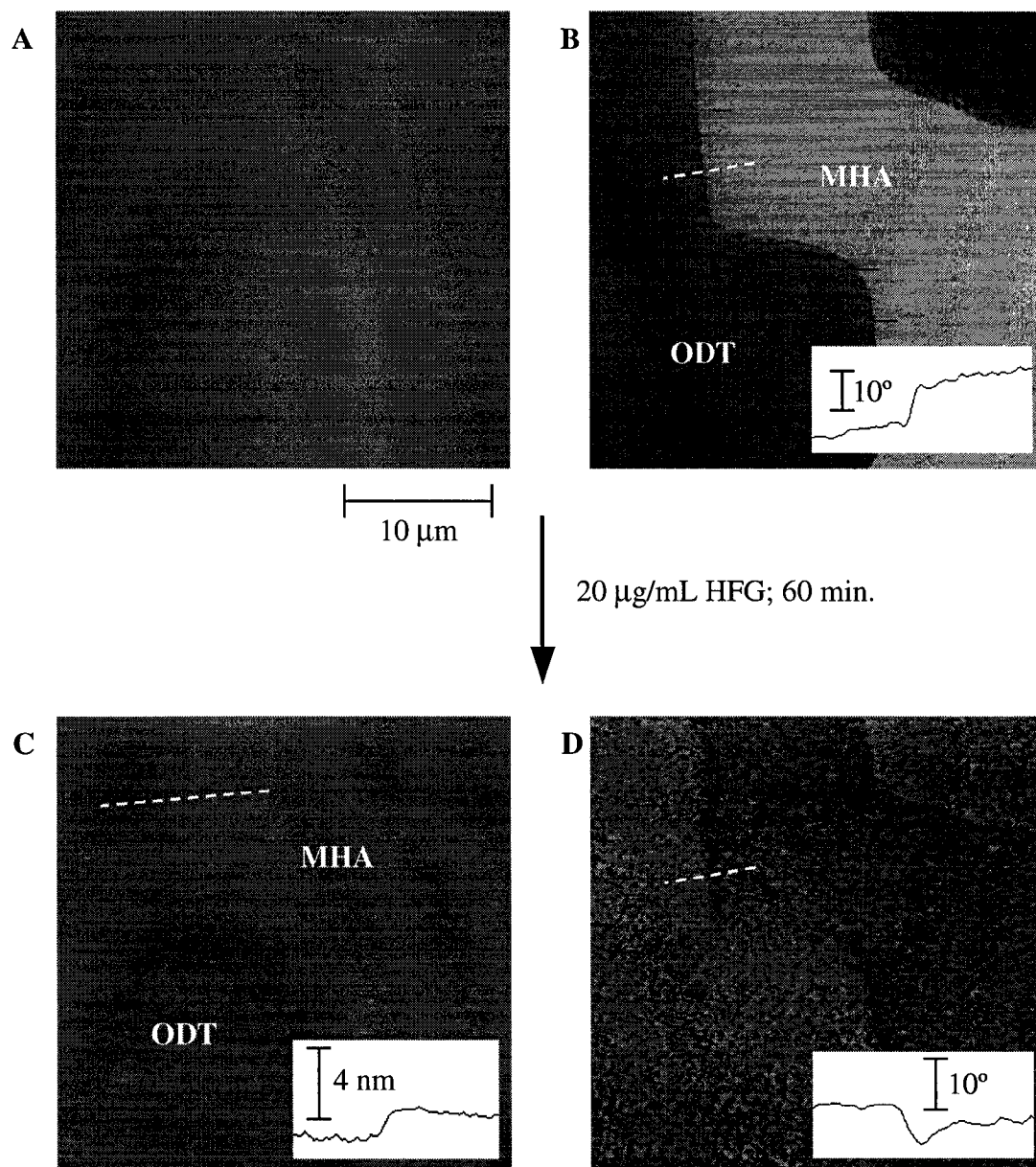


Figure 2.02. Tapping-mode images of a patterned surface before (A, B) and after (C, D) adsorption of HFG. Topographic (A, C) image scale, z-scale=40 nm, and phase (B, D), z-scale=60°. Insets show cross-sectional profiles indicated by the dashed lines in the images.

between the tip and ODT monolayer relative to the tip and MHA monolayer. For example, at a MHA monolayer, the measured adhesion hysteresis of an unmodified Si₃N₄ tip was negligible for 40 force-distance curves while on a different substrate bearing an ODT layer a value of 1.5 ± 0.6 nN was measured with the same cantilever/tip. The greater adhesion observed at the ODT interface is primarily due to a high energy of solvation for the hydrophobic surface in the aqueous buffer.^{21, 22} That is, there is a large entropy loss when rehydrating the hydrophobic surface upon tip-sample separation. Thus, it is likely that variations in adhesion energy hysteresis govern the differences in energy dissipation which result in observed $\Delta(\Delta\Phi)$ in Figure 2.02(B).¹³

After exposing the substrate to 20 $\mu\text{g/mL}$ HFG in PBS for 30 min. in the TM-SFM fluid cell, and subsequent flushing with protein-free PBS, the topographic difference becomes more pronounced. Figure 2.02(C) shows a greater height for the HFG layer on the carboxylate-terminal MHA surface than on the methyl-terminated ODT surface. The height difference was measured at different regions of the surface to be between 1.4-1.7 nm higher on the carboxylate layer. The phase image in Figure 2.02(D) shows a prominent phase contrast that is reversed from that of the substrate (-4° for MHA compared to ODT regions). The spatial arrangement of the contrast correlates with the underlying substrate implying that the contrast is governed by surface chemistry. Further studies were performed in order to illuminate the factors responsible for the observation of phase contrast in Fig. 2.02(D)

3.2. Sample properties affecting the generation of phase contrast

The observation of the contrast in Figure 2.02(D) can be attributed to variations in the 2-dimensional structure of HFG films (e.g. coverage, packing density) on each

chemically distinct region and/or variations in the state (conformation and orientation) of the adsorbed proteins. Infrared spectroscopy was used to further investigate the difference in adsorbed HFG film structure.

IRRAS was used to examine the adsorption of HFG to carboxylate- and methyl-terminated monolayers. In this case, MUA and UDT (both C₁₁) were used in order to have the same alkyl chain length in the monolayer. It has been shown that the intensity of the amide II band (1480-1600cm⁻¹) varies nearly linearly with protein concentration.^{23,}
²⁴ Thus, IRRAS was used to assess the likelihood of a difference in surface protein coverage contributing to the observed difference in phase contrast.

Figure 2.03 shows the spectra in the characteristic amide stretching region for HFG on ODT and MHA SAMs. Table 2.1 summarizes the results of the analysis of peak positions and intensities for the spectra in Fig. 2.03. The amount of protein adsorbed to each surface, as measured by the amide II intensity, is similar, with 18% less on the carboxylate surface. With a slightly larger amount of protein adsorbed on the ODT surface, the reversal of image contrast in Fig. 2.02(D) becomes difficult to rationalize on the basis of a difference in surface coverage.

In order to further investigate the surface coverage of adsorbed fibrinogen on ODT and MHA monolayers, real-time SFM imaging of HFG film formation was employed by other members of our research group. By observing the film formation in real-time imaging experiments on crystalline gold, it was shown that after 30 min., an HFG film uniformly covered the surface of both ODT and MHA SAMs. The presence of Au(111) step-edges, which became uniformly covered by the protein film, displaying neither regions of incomplete HFG coverage nor any multilayer formation, was used as a

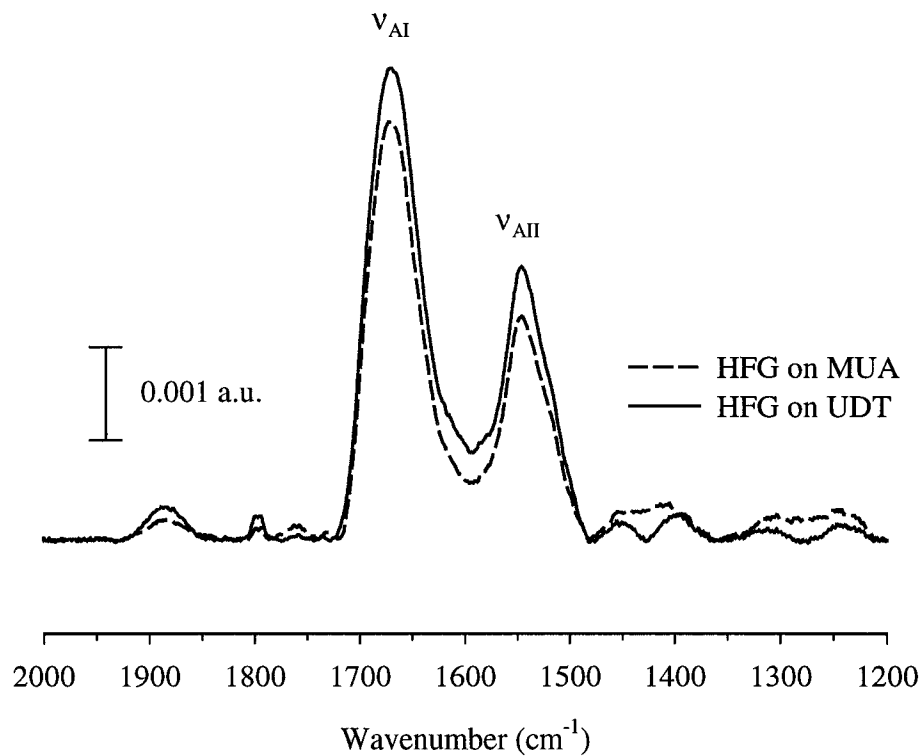


Figure 2.03. IRRAS spectra of HFG films in the amide stretching region show that the amide II band at 1545 cm^{-1} is higher on MUA than on UDT.

diagnostic.²⁵ Thus, it had been shown that HFG forms uniform monolayer films with no observable vacancies on MHA and ODT when adsorbed from 20 $\mu\text{g}/\text{mL}$ solutions.

With no indication of vacancies, the indication from the IRRAS experiments is that while the surface coverages are similar enough to be an unlikely source of the observed phase contrast in Fig. 2.02(D), there may be a greater packing density on the ODT surface. Since there were no observed defects in the complete films on either SAM, however, a difference in packing density would indicate some compression of the proteins on the hydrophobic SAM relative to the proteins on the hydrophilic SAM. Table 2.1 shows evidence for a change in conformation upon adsorption.

It has been previously shown that infrared peak shifts of the amide I band correlate with conformational change upon adsorption.²⁶⁻³¹ The shifts in peak position have been correlated with the loss of α -helical content relative to disordered and β -sheet structural elements.^{27, 28} Variations in conformation of adsorbed HFG relative to the bulk protein can be assessed with IR spectroscopy. IRRAS spectra of adsorbed species revealed that the amide I band position was blue shifted by $\sim 20\text{ cm}^{-1}$ for each of the adsorbed films relative to the spectrum of the crystal (Table 2.1). Liedberg *et al* showed the amide I band position to occur at 1649 cm^{-1} for native fibrinogen.²⁶ Work in our lab has revealed a similar amide I position for native HFG.³² Samples that represent a more native conformation of HFG yield amide I band positions at significantly lower wavenumbers from the adsorbed films. These data indicated that HFG changes conformation during the adsorption process to either methyl or carboxylate surfaces. This assertion is consistent with the generally accepted occurrence of surface-induced changes in protein conformations.^{1, 6, 7} Although the observed change in conformation is

	Native	Adsorbed	
		UDT	MUA
$\nu_{\text{AI}} (\text{cm}^{-1})$	1649	1670	1670
amide I intensity (a.u.)	n/a	0.005046	0.004466
$\nu_{\text{AII}} (\text{cm}^{-1})$	1547	1546	1546
amide II intensity (a.u.)	n/a	0.002930	0.002404

Table 2.1. IRRAS was performed on HFG films formed on complete monolayers of UDT and MUA. Native values from ref. 22.

exacerbated by the necessary drying of the samples for IRRAS, the peaks on the adsorbed proteins are also shifted relative to spectra from the dry solid HFG, which place the amide I position at 1650 cm^{-1} .³² Because the conformation of HFG is altered from its native state upon adsorption, it is possible that differences in the average adsorbed conformations on each surface chemistry are a factor in determining the observed phase contrast in TM-SFM. Thus, infrared spectroscopy has shown that HFG adsorbs to both carboxylate and methyl-terminated SAMs in similar amounts, and is denatured in the process. In order to further explore the bound state of the proteins, surface plasmon resonance (SPR) was employed.

Figure 2.04 shows SPR sensorgrams obtained for adsorption of $20\text{ }\mu\text{g/mL}$ HFG to ODT and MHA surfaces. The increase in signal corresponds to the angle shift in the minimum light intensity, or SPR angle shift. The results of the SPR experiments were a change in signal of 2680 ± 170 for adsorption of HFG to the ODT surface and 4320 ± 430 on the MHA surface. The response units (RU) of the Biacore instrument represent an angle shift of 0.0001° .³³ The difference indicates that a greater mass concentration of protein accumulates on the MHA surface than on ODT. Using an approximation of 1 pg/mm^2 in surface mass concentration for each RU,³⁴ the estimated mass concentration is roughly 2.7 ng/mm^2 on ODT and 4.3 ng/mm^2 on MHA. Although this estimate can only be taken as a gross approximation, given that denaturation can alter the thickness, and possibly the refractive index, of a protein layer, the observed difference in surface mass concentration confirms that the protein surface density is dependent on the surface chemistry.

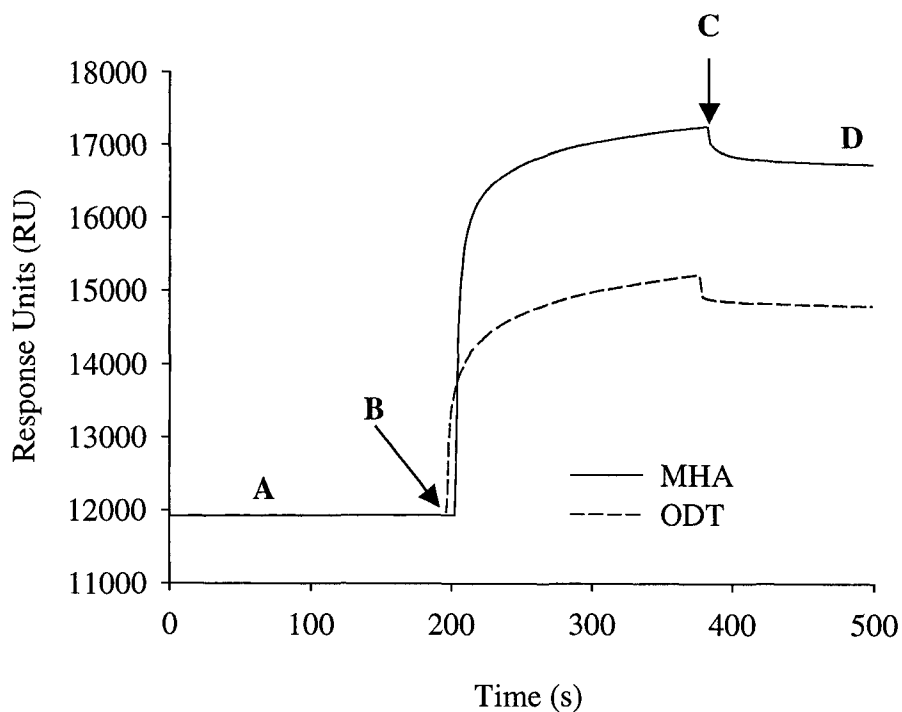


Figure 2.04. SPR sensorgrams of HFG adsorption to MHA and ODT SAMs. (A) PBS flow. (B) Injection of 20 $\mu\text{g/mL}$ HFG. (C) PBS rinse flow removes weakly sorbed proteins. (D) New steady state signal. By calculating the difference between the signal levels at (D) and (A), the overall change due to HFG adsorption is obtained.

This difference in surface density does not correlate well with the observation of a greater amount of HFG observed on the hydrophobic surface as seen with IRRAS. The difference may be indicative of differences in the mass transport conditions, for while the HFG films in the IRRAS and TM-SFM studies were adsorbed from a stagnant solution for one hour, the SPR experiments were carried out under flow for shorter intervals. This ceaseless flow was a property of the instrument, and the short times were found to reflect the same relative values as developed over longer adsorption times. However, results obtained in our laboratory have confirmed the much higher signal observed for HFG adsorbing on carboxylate surfaces by SPR imaging, in which the solution is allowed to sit stagnant for one hour.³² In addition, the difference in HFG adsorption on methyl- and carboxylate-terminated SAMs measured by SPR (-38% on methyl) appeared to contradict that observed by IRRAS (+18% on methyl).

The root cause of the difference between the two techniques may lie in different average orientations adopted by the proteins and/or differences in the levels of conformational alterations on each surface. If the protein denatured more, the thickness of the layer formed may be lower. As a result, the volume of intersection with the evanescent field from the surface plasmons may be diminished, causing a lower signal than that of the less denatured protein even for a comparable or greater surface density. Thus, because the SPR signal difference for the HFG on the two monolayers is so much larger than that observed by IRRAS, there may be a substrate-induced effect on how compressed the protein layer becomes.

Based on these results, the $\Delta(\Delta\Phi)$ observed in Figure 2.02(D) can be attributed to some difference in the adsorbed state of the protein film on each functional group. Conformation and orientation characterize the state of an adsorbed protein and it is generally difficult to differentiate the nature of the contribution of each of these factors to observable phenomena.

It is known that surface hydrophobicity is a key element governing the extent of conformational change of fibrinogen upon adsorption.^{6, 27, 35} This observation suggests that the conformational changes are likely to differ between the surfaces of methyl- and carboxylate-terminated SAMs. Thus, it appears that the height difference shown in Figure 2.02(C) is the result of a greater degree of denaturation of HFG on the hydrophobic ODT surface. Based on the combined weight of the above results, it can be concluded that the presence of a distinct phase contrast in the protein film shown in Fig. 2.02(D) is indicative of an overall difference in the conformational relaxation of HFG on each functional group. The orientations of adsorbed proteins that are denatured from their native conformations are difficult to assess at this time. Due to the unlikelihood of a single orientation or conformation at either surface, phase images provide a map of differences in average adsorbed states.

Any difference in average orientations is likely to be a negligible contributor to the SPR results since the large size, flexibility and oblong shape of the fibrinogen molecule would make side-on interactions with the surface more favourable than end-on binding. Given that the molecular dimensions of the molecule are 47 nm in length and 6 nm in width, the structure can be approximated as a cylinder. Rotations of the cylinder about its axis while adsorbing with that axis parallel to the surface will not greatly

influence the footprint occupied by the molecule on the surface. However, there may be a greater range of binding orientations on hydrophobic surfaces since the initial adhesive contacts may not be as reversible as on hydrophilic surfaces.³⁶ As a result, some molecules on the hydrophobic surface will adsorb in different orientations as further surface contacts are made by the initially attached proteins. Thus, while some orientations may result in greater topography (e.g. “end-on” adsorption), the observation, oft-repeated within our laboratory, that the height of fibrinogen layers is larger on carboxylate surfaces than methyl surfaces suggests that the HFG layer is more compact overall on methyl-terminated SAMs. This compression may be a result of differing degrees of protein structural alteration rather than differences in average orientations. Thus, it seems that the differing degrees of substrate-induced denaturation on the two SAMs are a plausible reason for the observed phase contrast. Further work was undertaken in order to gain insights into the mechanisms responsible for the generation of phase contrast of the protein layers.

3.3. Investigation of dissipation mechanisms responsible for phase contrast

The phase contrast observed for protein films adsorbed to patterned substrates may be caused at least in part by differences in tip-protein adhesion energy hysteresis. The results of contact mode imaging with the same sample-substrate system have shown frictional contrast,² suggesting that the adhesion properties at the solution interface of the adsorbed protein surface may be a factor in the phase contrast as well. Viscoelastic interactions and differences in sample stiffness may also play a role in determining

$\Delta(\Delta\Phi)$.¹⁵ In order to gain further insight into the nature of the differences in energy dissipation, HFG films were probed with force-distance analysis.

A series of force curves obtained separately for HFG on ODT and MHA films revealed complex retraction curves owing to the higher-order structural properties of the adsorbates. The retraction portion of the force curve refers to the profile of cantilever deflections as a function of distance as a probe tip in contact with the sample is lifted away from the surface. The force curves were obtained using a gold-coated probe tip modified with a protein-resistant SAM of EG3-OMe in order to limit the observed protein interaction events to those caused by the protein film on the sample surface. It should be noted that the phase contrast observed in Fig. 2.02(B, D) was also observed using EG3-OMe coated probe tips.

Figure 2.05 shows three examples of the types of retraction curves observed for HFG surfaces on each functional group. The data have been recalculated to display force as a function of tip-sample separation. Hence, what is seen is a result of pulling a probe tip to which a surface-bound protein film has adhered. On both monolayers, HFG exhibits a complicated behaviour owing to the multiple peaks in the observed unloading force. This type of interaction has been observed during the forced extension of modular proteins with multiple folded domains.³⁷⁻³⁹ When the force exerted on a multi-domain system causes one of the domains to spontaneously unfold, there is a sudden release of the energy stored in the folded structure, causing the cantilever to snap back to the unloaded position. The presence of multiple peaks in the force curves in Fig. 2.05 thus reflects the unfolding of multiple protein domains and, possibly, breaking of intermolecular attractions. An important feature of the force curves is the extension of

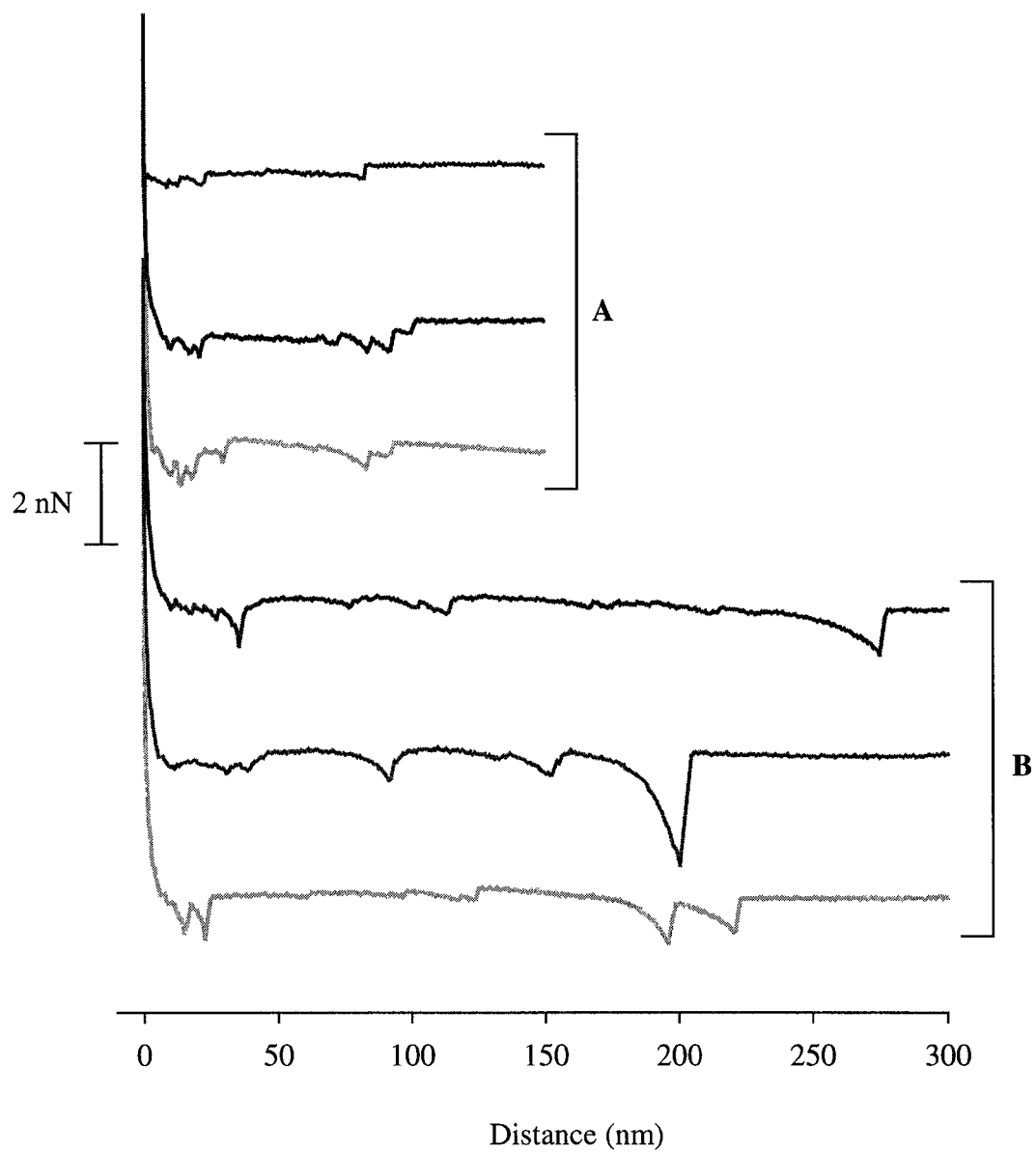


Figure 2.05. Typical force vs. tip-sample separation curves for HFG on (A) ODT and (B) MHA SAMs.

the film to distances longer than the 47 nm native length of HFG. It was also generally observed that the unfolding distances indicated greater extension lengths on the MHA surface than on the ODT surface, as shown in Fig. 2.05. These observations point to the formation of a film with greater lateral inter-protein interactions on the MHA surface. A laterally networked film of HFG would be able to delaminate from the surface to longer retraction distances than any individual molecule.

This interpretation is consistent with the real-time imaging performed in our lab, which had demonstrated that film formation occurs via the growth of fibre-like structures across mica, which, like MHA on gold, has a negatively charged, hydrophilic surface.⁹ Of the force curves measured, all HFG retraction curves on MHA exhibited some adhesive interaction with the probe tip. On the ODT surface, however, 50% of the attempted force curves resulted in no adhesion between the protein film and the probe tip. This observation, in conjunction with the observation of shorter stretching distances for the HFG film on the ODT surface, indicate that the film is bound more strongly to the hydrophobic surface.

Figure 2.06 is a histogram of the observed peaks resulting from unfolding events. The data represent the measurements of 56 force curves on MHA and 30 force curves on ODT. It is readily apparent from this graph that the film formed on the MHA surface is able to extend to longer distances. In addition, the HFG layer exhibits more unfolding events per attempted force curve. On average, 6 peaks at various separation distances were observed for each force curve on HFG/MHA and 3 peaks for the HFG/ODT system. Thus, the HFG on the hydrophobic surface is more tenaciously bound and, as previous data had shown, more compressed than on the hydrophilic surface. These observations

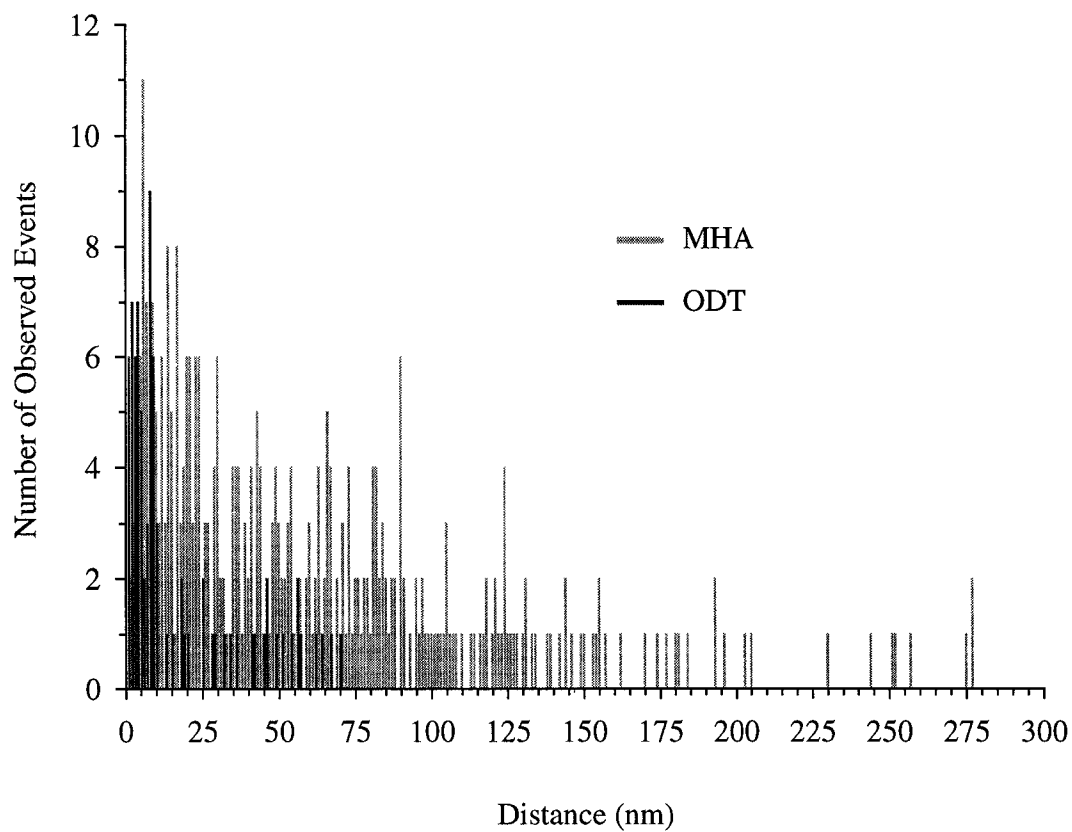


Figure 2.06. Histogram of maximum distances for disengagement of probe tip from HFG film on ODT and MHA.

lend further credence to the hypothesis that the protein is more denatured on the hydrophobic surface. The formation of an interconnected sheet of proteins may result in an enhanced ability to dissipate energy. A somewhat analogous situation is the dissipation of the collision energy of flying insects by the interconnected strands of silk in the 2-dimensional capture webs of orb-weaving spider. The web is able to dissipate the shock of the impact through the unfolding of interconnected globular protein domains along each strand, resulting in the ensnaring of airborne prey without breakage of the web.⁴⁰ As a result of greater interconnections among the HFG molecules on the MHA surface, as well as the greater tenacity of the adsorption to the ODT surface, it is conceivable that the film on the more hydrophilic MHA surface is able to dissipate more energy from a SFM probe. Given that phase imaging is able to map surface properties based on differences in dissipated energy, the contrast observed in Fig. 2.02(D) may be due to the domain unfolding dissipative mechanism revealed by the force curve analysis. For comparison, a phase imaging experiment was performed using another less structurally complex protein.

BSA is a smaller molecule (66 kDa) and has a globular structure due to the folding of a single polypeptide chain. Figure 2.07 shows the topographic and phase images before and after adsorption of BSA to a patterned SAM. From Figs. 2.07(B, D) it is apparent that there is a surface chemistry-directed difference in the structural properties of the BSA film; this allows a phase contrast to develop. Force curves collected on BSA did not display the multiple unfolding events as did HFG, but were more typical in appearance (see Fig. 1.08). Literature examples of force curves for BSA have also shown this simplified behaviour.⁴¹ Given that albumin has been shown to undergo

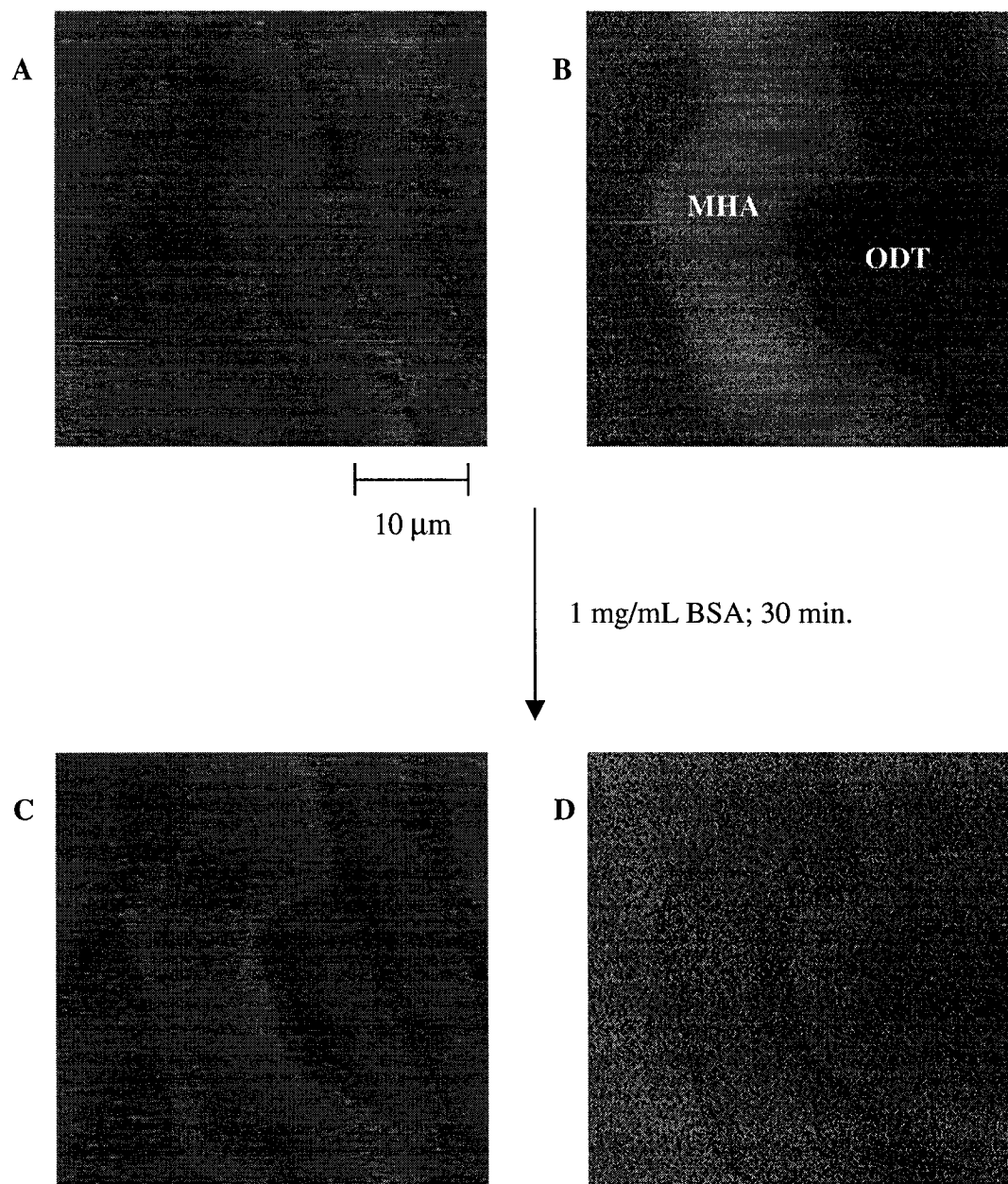


Figure 2.07. Topographic (A, C) and phase (B, D) images of a patterned ODT/MHA monolayer before and after adsorption of BSA. Height scales are 80 nm (A) and 30 nm (C); phase scales are 80° (B) and 30° (D).

conformational rearrangements at the solid-liquid interface, it seems that the differences in the denaturation of the protein on differentially hydrophobic surfaces play a key role in the generation of phase contrast during tapping-mode imaging. In addition, the evolution of a phase contrast for BSA on different surface chemistries does not appear to be dependent on the dissipative mechanism postulated earlier for the HFG films. As a result, the dissipation of energy in the retraction portion of the cantilever oscillation by the unfolding of molecular domains is not likely to be the correct mechanism.

A more likely mechanism is a difference in the viscoelastic damping of the cantilever motion by proteins in different surface conformations. In order to adsorb at a hydrophobic surface, proteins must displace a water layer relatively dense compared to the bulk.⁴² In addition, when proteins adsorb, expulsion of hydration water from the protein occurs, allowing hydrophobic regions to contact the surface.⁴³ The expulsion of water at the interface between hydrophobic protein regions and a surface is a driving force for the strong interaction between proteins and hydrophobic surfaces. Further conformational changes, which may occur after the initial adsorption, may be a result of slow rearrangements to maximize hydrophobic contacts and expel more water from the interior of the protein and cause greater compaction of the proteins.

Phase imaging has shown that the more compact protein layer on the hydrophobic ODT surface dissipates less energy from an oscillating cantilever. Thus, the critical factor in determining phase contrast can be viewed as the degree of dehydration experienced by the proteins at the interface. This dehydration is influenced by the hydrophobicity of the surface to which adsorption occurs. Given the established mechanisms by which energy can be dissipated in TM-SFM, the energy dissipation in the

present case must depend on differences in the viscoelasticity and/or adhesion energy hysteresis of the tip-sample contact of the protein layer on different surface chemistries.¹³ No case has ever been shown in the literature to unambiguously ascribe the underlying physical mechanism for phase contrast in viscoelastic systems, the most commonly studied of which are polymers.

Viscoelasticity is a property characterized by a response to deformation in between that of viscous flow and elastic response. The response of a viscoelastic material to a sudden deformation or indentation is to return to its original state, as would an elastic solid, but in a time-dependent manner characteristic of viscous liquids.⁴⁴ Thus, a possible explanation for the phase contrast observed is that the viscoelastic response of the protein layers is altered by the degree of dehydration. Differences in stiffness alone do not contribute to phase contrast. Because a more compliant sample can be indented further, the area of contact between a probe tip and a sample can increase. The resulting increase in adhesive contact could then allow more energy dissipation via adhesion energy hysteresis. Adhesion energy hysteresis being the term which describes the energy loss due to the irreversible path between the approach and retraction phases of a force curve.

More clarity regarding the phase contrast mechanism was sought by imaging HFG in the absence of intermolecular interactions. Figure 2.08 shows a high resolution tapping mode image of HFG adsorbed to an MHA surface from a 50 ng/mL solution. The low concentration results in a sub-monolayer coverage. The use of the amplitude signal to generate images is similar to typical topographic imaging, but results in better sensitivity to the edges of topographic features. This occurs because the signal used is

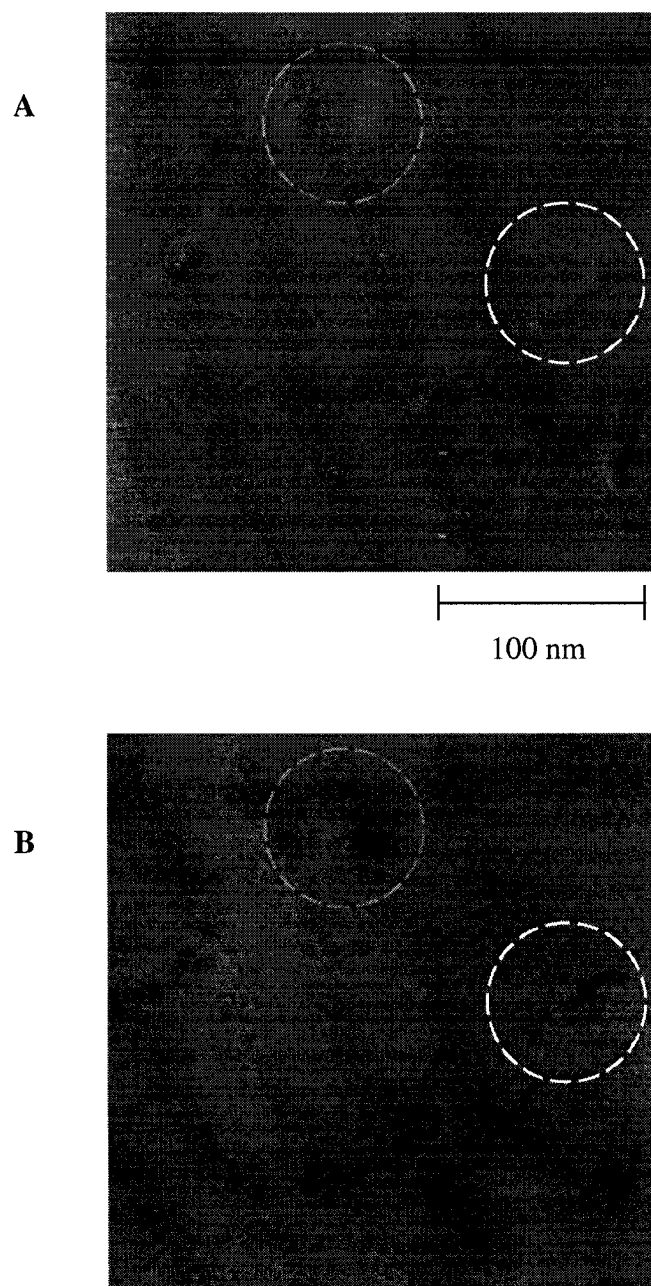


Figure 2.08. High-resolution tapping-mode images show individual trinodal HFG molecules (white) as well as larger globular structures (green) adsorbed to a MHA SAM. Protein features in amplitude image (A), z-scale=1.5 nm are reproduced as areas of phase lag, or darker regions, in the corresponding phase image (B), z-scale=15°.

the immediate change in amplitude of the cantilever experienced at a step in height, whereas topographic images are a map of the separation between the sample substrate and the cantilever necessary to maintain a target oscillation amplitude. Individual molecules of HFG are clearly visible in Fig. 2.07(A). In addition, several globular aggregates are also observed. For either globular aggregates or individual molecules, there is a corresponding phase lag. Thus, in the absence of the ability to dissipate energy via unfolding of linked molecular domains, a phase contrast is still generated between proteins and the MHA substrate. Two individual molecules (cf. Fig. 1.02(A)) are clearly visualized in the amplitude image and neither has been translated or deformed by the interactions with the cantilever over several scan lines. Given that molecular unfolding events resulting from a strong interaction with the tip would perturb the geometry of the molecule, the observation of the characteristic barbell shape of HFG strongly suggests that domain unfolding events do not occur for the individual molecules or small aggregates during tapping-mode imaging.

While the unfolding of molecular domains may not be responsible for the observed phase shift, it is still not possible to rule out adhesion energy hysteresis as a factor in the generation of a phase contrast. Another plausible mechanism by which the adhesion energy hysteresis can cause a difference in $\Delta\Phi$ on the two protein layers is that the two layer types have different stiffnesses as a result of the conformational relaxations. If the more compacted film on the hydrophobic surface has a higher modulus than the protein film on the hydrophilic surface, the probe tip will indent further on the hydrophilic surface. As a result, the tip-sample contact area will be larger and will result in a greater dissipative interaction.¹⁹ This explanation assumes that there is a negligible

average difference in the adhesive properties of the surfaces of the proteins exposed to the probe tip. In addition, differences in the viscoelastic responses cannot be ruled out by the existence of any differences in the stiffness. Thus, the dissipative mechanism responsible for the phase contrast in Fig. 2.02(D) remains unclear.

4. Conclusions

Tapping mode SFM was shown to be able to map substrate-induced differences in protein films on a patterned methyl- and carboxylate-terminated SAMs. Phase imaging revealed that more energy was dissipated by HFG films on MHA than on ODT. Because the interaction with a more hydrophobic surface is more dehydrating to adsorbing proteins, the conformations are altered to a greater degree than on hydrophilic surfaces. Force curve analysis of HFG films revealed that one of the consequences is more tenacious binding to hydrophobic surfaces. In addition, the force curve analysis revealed domain unfolding during forced extension as a plausible mechanism for the energy dissipation observed in the phase imaging. Further investigation revealed this to be an unlikely cause of the differences in energy dissipation. Contributions from tip-sample adhesion energy hysteresis and viscoelastic damping by HFG films dehydrated to different degrees on surfaces of differing hydrophobicities were presented as possible reasons for the observed phase contrast. Despite the lack of a clear mechanism, phase imaging was shown to be of use in differentiating films comprised of proteins conformationally altered by interactions with the substrate.

5. References

- (1) Brash, J. L.; Horbett, T. A. In *Proteins at Interfaces II: Fundamentals and Applications*; Horbett, T. A., Brash, J. L., Eds.; American Chemical Society: Washington, D. C., 1995, pp 1-23.
- (2) Ta, T. C.; McDermott, M. T. *Anal. Chem.* **2000**, *72*, 2627-2634.
- (3) Feldman, K.; Hahner, G.; Spencer, N. D.; Harder, P.; Grunze, M. *J. Am. Chem. Soc.* **1999**, *121*, 10134-10141.
- (4) Huang, N.-P.; Michel, R.; Voros, J.; Textor, M.; Hofer, R.; Rossi, A.; Elbert, D. L.; Hubbell, J. A.; Spencer, N. D. *Langmuir* **2001**, *17*, 489-498.
- (5) Ostuni, E.; Chapman, R. G.; Holmlin, R. E.; Takayama, S.; Whitesides, G. M. *Langmuir* **2001**, *17*, 5605-5620.
- (6) Sit, P. S.; Marchant, R. E. *Thromb. Haemost.* **1999**, *82*, 1053-1060.
- (7) Norde, W.; Haynes, C. A. In *Interfacial Phenomena and Bioproducts*, 1 ed.; Brash, J. L., Wojciechowski, P. W., Eds.; Marcel Dekker, Inc.: New York, 1996; Vol. 23, pp 123-144.
- (8) Lin, F.-Y.; Chen, W.-Y.; Hearn, M. T. W. *Anal. Chem.* **2001**, *73*, 3875-3883.
- (9) Ta, T. C.; Sykes, M. T.; McDermott, M. T. *Langmuir* **1998**, *14*, 2435-3443.
- (10) Hansma, P. K.; Cleveland, J. P.; Radmacher, M.; Walters, D. A.; Hillner, P. E.; Bezania, M.; Fritz, M.; Vie, D.; Hansma, H. G.; Prater, C. B.; Massie, J.; Fukunaga, L.; Gurley, J.; Elings, V. *Appl. Phys. Lett.* **1994**, *64*, 1738-1740.
- (11) Radmacher, M.; Fritz, M.; Hansma, H. G.; Hansma, P. K. *Science* **1994**, *265*, 1577-1579.

- (12) Finot, M. O.; McDermott, M. T. *J. Am. Chem. Soc.* **1997**, *119*, 8564-8565.
- (13) Tamayo, J.; Garcia, R. *Appl. Phys. Lett.* **1997**, *71*, 2394-2396.
- (14) Cleveland, J. P.; Anczykowski, B.; Schmid, A. E.; Elings, V. B. *Appl. Phys. Lett.* **1998**, *72*, 2613-2615.
- (15) Garcia, R.; Tamayo, J.; Calleja, M.; Garcia, F. *Appl. Phys. A* **1998**, *66*, S309-S312.
- (16) Bar, G.; Brandsch, R.; Bruch, M.; Delineau, L.; Whangbo, M.-H. *Surf. Sci.* **2000**, *444*, L11-L16.
- (17) Holland, N. B.; Marchant, R. E. *J. Biomed. Mater. Res.* **2000**, *51*, 307-315.
- (18) Aherne, D.; Rao, S. N.; Fitzmaurice, D. *J. Phys. Chem. B* **1999**, *103*, 1821-1825.
- (19) Anczykowski, B.; Gotsmann, B.; Fuchs, H.; Cleveland, J. P.; Elings, V. B. *Appl. Surf. Sci.* **1999**, *140*, 376-382.
- (20) McDermott, M. T.; Green, J.-B. D.; Porter, M. D. *Langmuir* **1997**, *13*, 2504-2510.
- (21) Hoh, J. H.; Cleveland, J. P.; Prater, C. B.; Revel, J.-P.; Hansma, P. K. *J. Am. Chem. Soc.* **1992**, *114*, 4917-4918.
- (22) Hudson, J. E.; Abruna, H. D. *J. Am. Chem. Soc.* **1996**, *118*, 6303-6304.
- (23) Jakobsen, R. J.; Brown, L. L.; Winters, S.; Gendreau, R. M. *J. Biomed. Mater. Res.* **1983**, *16*, 199-201.
- (24) Gendreau, R. M.; Leininger, R. I.; Winters, S.; Jakobsen, R. J. In *Biomaterials: Interfacial Phenomena and Applications*; Cooper, S. L., Pappas, N. A., Eds.; American Chemical Society: Washington, D.C., 1982, pp 371-394.
- (25) Ta, T. C.; Ph. D. Thesis, University of Alberta, Edmonton, 2001.

- (26) Liedberg, B.; Ivarsson, B.; Lundstrom, I. *J. Biochem. Biophys. Methods* **1984**, *9*, 233-243.
- (27) Lu, D. R.; Park, K. *J. Colloid Interface Sci.* **1991**, *144*, 271-281.
- (28) Lenk, T. J.; Ratner, B. D.; Gendreau, R. M.; Chittur, K. K. *J. Biom. Mater. Res.* **1989**, *23*, 549-569.
- (29) Jakobsen, R. J.; Wasacz, F. M.; Brasch, J. W.; Smith, K. B. *Biopolymers* **1986**, *25*, 639-654.
- (30) Wasacz, F. M.; Olinger, J. M.; Jakobsen, R. J. *Biochemistry* **1987**, *26*, 1464-1470.
- (31) Cheng, S.-S.; Chittur, K. K.; Sukenik, C. N.; Culp, L. A.; Lewandowski, K. J. *Coll. Interface Sci* **1994**, *162*, 135-143.
- (32) Nsiah, F.; M. Sc. Thesis, University of Alberta, Edmonton, 2003.
- (33) Biacore Inc.: http://www.biacore.com/technology/spr_technology.lasso, 2003.
- (34) Stenberg, E.; Persson, B.; Roos, H.; Urbaniczky, C. *J. Coll. Interface Sci.* **1991**, *143*, 513-526.
- (35) Wertz, C. F.; Santore, M. M. *Langmuir* **2001**, *17*, 3006-3016.
- (36) Wertz, C. F.; Santore, M. M. *Langmuir* **2002**, *18*, 706-715.
- (37) Rief, M.; Gautel, M.; Oesterhelt, F.; Fernandez, J. M.; Gaub, H. E. *Science* **1997**, *276*, 1109-1112.
- (38) Smith, B. L.; Schaffer, T. E.; Viani, M.; Thompson, J. B.; Frederick, N. A.; Kindt, J.; Belcher, A.; Stucky, G. D.; Morse, D. E.; Hansma, P. K. *Nature* **1999**, *399*, 761-763.
- (39) Oberdorfer, Y.; Fuchs, H.; Janshoff, A. *Langmuir* **2000**, *16*, 9955-9958.

- (40) Becker, N.; Oroudjev, E.; Mutz, S.; Cleveland, J. P.; Hansma, P. K.; Hayashi, C. Y.; Makarov, D. E.; Hansma, H. G. *Nat. Mater.* **2003**, *2*, 278-283.
- (41) Dupont-Gillain, C. C.; Fauroux, C. M. J.; Gardner, D. C. J.; Leggett, G. J. *J. Biomed. Mater. Res.* **2003**, *67A*, 548-558.
- (42) Israelachvili, J. *Intermolecular and Surface Forces*, 2nd ed.; Academic Press: Toronto, 1992.
- (43) Ostuni, E.; Grzybowski, B. A.; Mrksich, M.; Roberts, C. S.; Whitesides, G. M. *Langmuir* **2003**, *19*, 1861-1872.
- (44) Christensen, R. M. *Theory of Viscoelasticity: An Introduction*; Academic Press: New York, 1971.

Chapter III

Surface Plasmon Resonance Imaging of Protein Arrays

1. Introduction

Studies of the effect of surface chemistry on protein film properties have shown that surface hydrophobicity can influence the degree of conformational relaxations in adsorbing proteins. Given that protein adsorption is a fundamental process underlying a range of technologies, analysis of the influence of substrate chemistry can highlight useful pathways to technological applications. One application of particular interest in the field of bioanalysis is immunoassays. The strong, specific binding of an antibody to its antigen has been widely exploited in clinical applications as well as in sensor design. The most common approach to immunoassays is to immobilize either the antibody or antigen to a solid support and to detect binding with a labeled partner. Labels for immunoassays have had a range of composition and detection mechanisms and include enzymes,¹ fluorescent molecules,²⁻⁴ nanoparticles^{5, 6} and radiolabels.⁷ Recently, the widespread application of DNA microarrays (gene chips) for massively parallel analysis has prompted researchers to develop multisensing immunoassays in microarray format.⁸⁻¹⁰ As well, the high throughput demands of proteomics have driven development in the fabrication and reading of microarrays of a variety of proteins.^{2, 4, 11}

Microarrays of immunoreagents and other proteins continue to be developed largely by extending technologies used for gene chips² but remain much more

problematic. For example, the fluorescence detection methods that are so successful for gene chips are much less convenient with protein chips due to synthetic challenges, multiple label issues and the potential for interfering with the binding site. Also, signal producing reactions catalyzed by commonly used enzyme-linked antibodies are difficult to implement in immunoassay microarray format. Strategies for the immobilization of proteins in the most efficient orientation and conformation for interactions with binding partners are much more complex.¹² Non-specific adsorption is also a much greater problem for proteins than for DNA. Finally, it is unlikely that a standard set of proteins having a large enough scope to meet all needs will be made readily available in the future. As such, custom-made protein chips that are easy to fabricate will be needed. In this paper, a facile method for creating arrays of antigen proteins on gold is demonstrated. Interactions of unlabeled antibodies at these microarrays are detected by surface plasmon resonance (SPR) imaging.

Microarrays are generally prepared by robotic pin printing biomolecules on glass slides.^{2, 13} A number of labs have shown that microfluidic networks formed in poly(dimethylsiloxane) (PDMS) can be employed to pattern and array a number of different types of biomolecules.^{8, 14} Corn and co-workers have applied these techniques to create arrays of peptides,¹⁵ carbohydrates¹⁶ and proteins¹⁷ on thin gold films and read interactions at these arrays in a label-free format with SPR imaging. SPR detects changes in refractive index within a short distance, on the order of hundreds of nanometers,^{18, 19} from the surface of a thin metal film as variations in light intensity reflected from the back of the array. Along with SPR imaging²⁰ other label free methods such as mass spectrometry,²¹ ellipsometry¹⁰ and Raman spectroscopy²² are also being developed for

microarray reading. It is our belief that the strategies for both the attachment and patterning of proteins on surfaces that are compatible with label free reading schemes will be important for widespread application of protein microarrays.

Described herein are two facile methods employing PDMS microfluidic networks to pattern proteins on SPR imaging sensor chips. In the first method developed, proteins are patterned on a carboxylate-terminated monolayer to give a line array. The second method involves patterning lines of amine- and oligoethylene glycol-terminated monolayers upon which proteins are adsorbed through a second set of microchannels. Label-free antibody binding to the array is monitored with SPR imaging. Given that SPR detects non-specifically, it was of paramount importance to develop surface treatments that would allow for unambiguous interpretation of signal changes. In the first method, the background was blocked with bovine serum albumin (BSA) in order to passivate the surface against nonspecific protein adsorption, and a surfactant, Tween 20, was employed in order to minimize non-specific binding.²³ In the second method, ethylene glycol-terminated alkyl thiol monolayers were used to create a protein resistant background between antigen spots. SPR imaging was shown to provide a useful detection scheme for immunoassay microarrays and for yielding quantitative information on the antibody-antigen binding characteristics.

2. Experimental

Mercaptoundecylamine hydrochloride (MUAM; Dojindo Laboratories, Japan) and 16-mercaptohexadecanoic acid (MHA; Aldrich) were purchased and used as

received; 1-mercaptoundec-11-yl)tri(ethylene glycol) methyl ether, $\text{HS}(\text{CH}_2)_{11}(\text{OCH}_2\text{CH}_2)_3\text{OCH}_3$ (EG3-OMe) was synthesized in general agreement with published methods.²⁴ An outline of the synthetic procedure follows. Tri(ethylene glycol) monomethyl ether (Fisher) was refluxed in 50% $\text{NaOH}_{(\text{aq})}$ for 2 hours; all reaction steps in this procedure were carried out in an inert argon atmosphere. 11-Bromoundec-1-ene (Aldrich) was added dropwise and the mixture was refluxed overnight. The mixture was cooled and then extracted six times with hexanes. The organic fractions were combined, dried over anhydrous sodium sulphate, and concentrated by rotary evaporation. The resulting oil was purified by flash chromatography on silica gel using 1:1 hexanes:ethyl acetate as the eluent. In order to visualize the content of the eluting fractions, thin-layer chromatography was performed and the plates developed with KMnO_4 staining. The product, undec-1-en-11-yltri(ethylene glycol) monomethyl ether, was dissolved to ~300 mM in methanol along with 15 mg AIBN and 3-4 g (excess) thioacetic acid. The stirring mixture was irradiated with a mercury vapour arc lamp for 5-6 hours. The resulting mixture was concentrated by rotary evaporation and purified on silica with 1:2 hexanes:ethyl acetate as eluent. The resulting thioacetate was converted to the thiol by refluxing in 0.5 M HCl in methanol for 5-6 hours, then stirring overnight at room temperature. The final product was obtained by purification on silica with 1:1 ethyl acetate:methylene chloride as eluent. TLC plates were developed with an ethanolic sulphuric acid stain. Electrospray mass spectrometry verified the correct mass (373.23840; Na adduct) and nuclear magnetic resonance spectroscopy confirmed the structure. The NMR spectrum also indicated that ~1/3 was present as the disulphide, which presented no problem for SAM formation.

Proteins used in this work were obtained in the highest available purity and used as received. Ovalbumin (OVA), bovine serum albumin (BSA), bovine fibrinogen (BFG) and Fraction I 95% clottable human fibrinogen (HFG) were obtained from Sigma and used as received. Anti-human fibrinogen, bovine and goat immunoglobulin G (bIgG and gIgG) and polyclonal rabbit antisera to these IgGs, as well as antisera to OVA, HFG and BSA, were obtained from ICN Biomedicals (Aurora, OH). All protein solutions were prepared in phosphate-buffered saline (PBS: 8.1 mM Na₂HPO₄, 1.5 mM KH₂PO₄, 137 mM NaCl, 2.7 mM KCl in 18MΩ water). PBS containing 0.01% Tween 20 will be referred to as PBS^T.

Poly(dimethylsiloxane) (PDMS) microfluidic channels were fabricated according to established methods.²⁵ Briefly, a relief pattern of photoresist on a silicon wafer was created photolithographically. By curing the prepolymer and cross-linker (Sylgard 184, Dow Corning; Midland, MI) 10:1 by weight against this relief structure, a negative of the relief was formed in the PDMS. The microchannels measured 200 μm wide by 10-15 μm deep. The PDMS device was also through-bored at the ends of the channels to allow fluids access to the channels when the PDMS device was applied to a surface. Fluid flow was driven by applying vacuum to one access point on the microchannel while connecting the other access point to a reservoir of solution.

The antigen arrays were constructed on a 45 nm gold thick film deposited on SF10 glass (Schott; Toronto, ON, Canada) with a 1 nm adhesive layer of chromium. The arrays were imaged using the GWC Instruments SPRImager (GWC Instruments; Madison, WI). Experiments were performed at fixed viewing angles; the interference filter produced a bandpass of 1.5 nm (FWHM) at 795 nm. Antibody solutions and buffer

solutions are introduced to the entire array surface via peristaltic flow through a fluid cell. Presented images were generated by averaging 100 individual snapshot images.

For analysis of antibody binding curves, the surface was blocked with 1% BSA in PBS within the fluid cell for 1 h prior to the introduction of antibodies. Each antibody solution was introduced to the array, in sequence from lowest to highest concentration, and allowed to adsorb for 1 h before being flushed out with PBS.

3. Results and Discussion

Initial attempts to observe parallel antibody binding events by SPR imaging utilized arrays created on self-assembled monolayers (SAMs) of MHA (Figure 3.01). Drawing on previous experience (see Chapter 2) in the use of SAMs for protein adsorption, MHA was used as the adsorptive surface. The rationale was that of the two most familiar SAM types, methyl- and carboxylate-terminal, the carboxylate-terminated monolayer would be less denaturing. Proteins were adsorbed through the microchannels from 100 $\mu\text{g}/\text{mL}$ PBS solutions for a period of 1 h. The protein patterning procedure described here differs from that described previously by Delamarche *et al.*¹⁴ in that the use of unmodified PDMS allows for a strongly sealed contact between the PDMS device and the substrate. In addition, by using vacuum pressure to drive fluid flow, we are able to incorporate rinsing steps directly within each channel. As a result, PBS can be used to displace the protein solutions from the channels and remove weakly sorbed material prior to the removal of the PDMS channel device from the substrate, reducing the likelihood of cross-contamination or loss of spatial resolution. Figure 3.02 shows the binding of

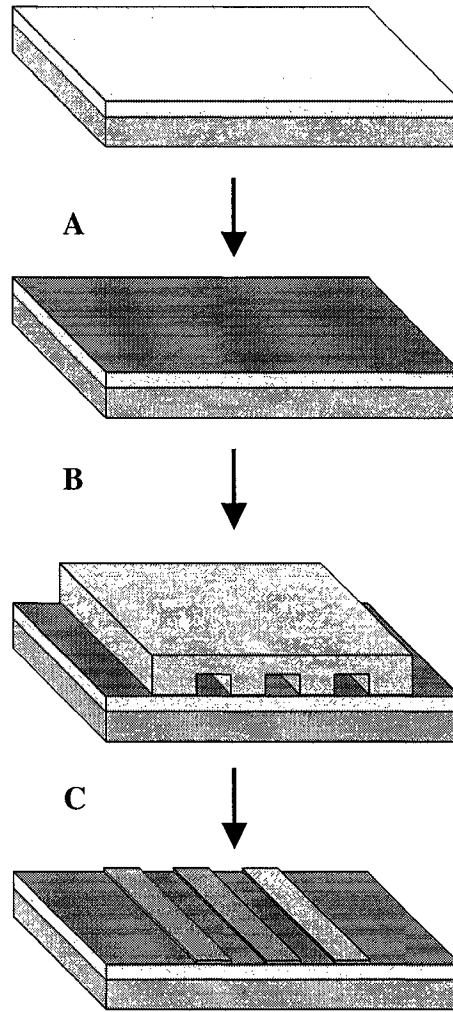


Figure 3.01. Protein patterning via microfluidic channels (μ FCs) in PDMS. (A) MHA SAM formed on gold SPR sensor surface. (B) PDMS device is placed on sensor surface, forming μ FCs. (C) Proteins are patterned in lines via μ FCs.

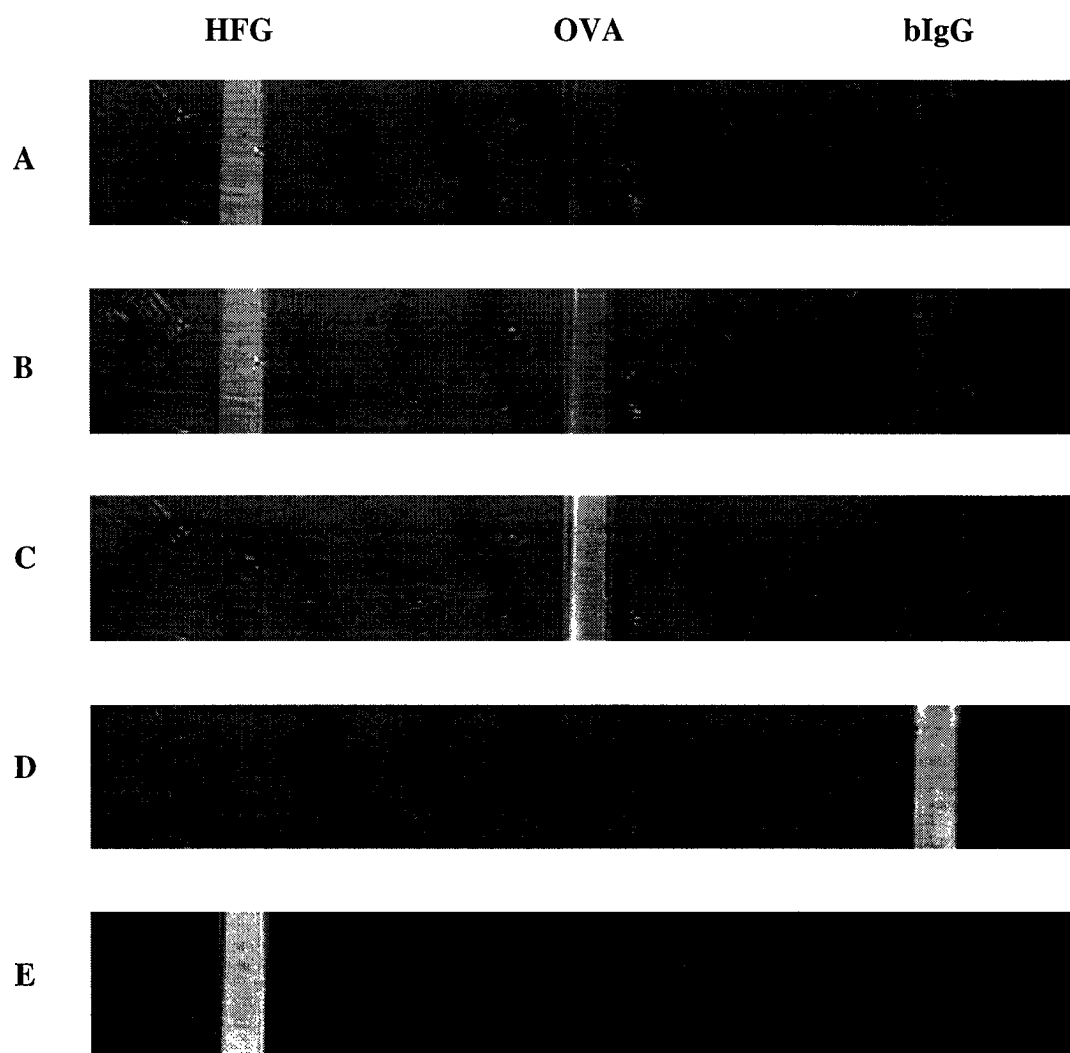


Figure 3.02. Three proteins on MHA surface. (A) Initial image. (B) Image after exposure to anti-OVA. (C) Difference image highlights changes between first two images. (D) Difference image after exposure of array to anti-bIgG. (E) Difference image after exposure of array to anti-HFG.

antibodies from PBS^T to an array of three proteins on a MHA SAM. Importantly, the contrast generated in SPR difference images is due to the change in refractive index resulting from the localized binding of the antibodies and requires no labeling of the antibodies. The images record differences in reflected light intensity from the backside of the chip as captured by the CCD camera. In the difference imaging process, the array image in Fig. 3.02(A) was subtracted from Fig. 3.02(B), the image taken after anti-OVA had been exposed to the array for ten minutes. The resulting image in Fig. 3.01(C) shows that the central protein, OVA, has a higher, or brighter, signal than the other proteins and the background area. The subsequent images in Figs 3.01(D, E) show successive difference images on the same array after exposures to anti-bIgG and anti-HFG, respectively. Cross-sectional graphs of the array before and after the antibody exposures are shown in Figure 3.03.

The cross-section of the unmodified array shows a somewhat sloped background due to variation in light intensity across the array. Unlike the images shown in Fig. 3.02, in which each difference image was produced by subtracting the previous image, the difference images used for cross-sectional analysis in Figure 3.03 were produced by subtraction of the initial array image from each image captured after antibody binding.

The first cross-section shows the difference signal across the array resulting from subtraction of the initial cross-section of the unmodified array from that produced by the anti-OVA exposure. The cross-section shows that the background is leveled by subtraction and also that the change in the background level is non-zero. The indication is that the antibody and/or surfactant adsorbed on the background MHA region. The subsequent antibodies were then effectively blocked from the surface by this initial layer;

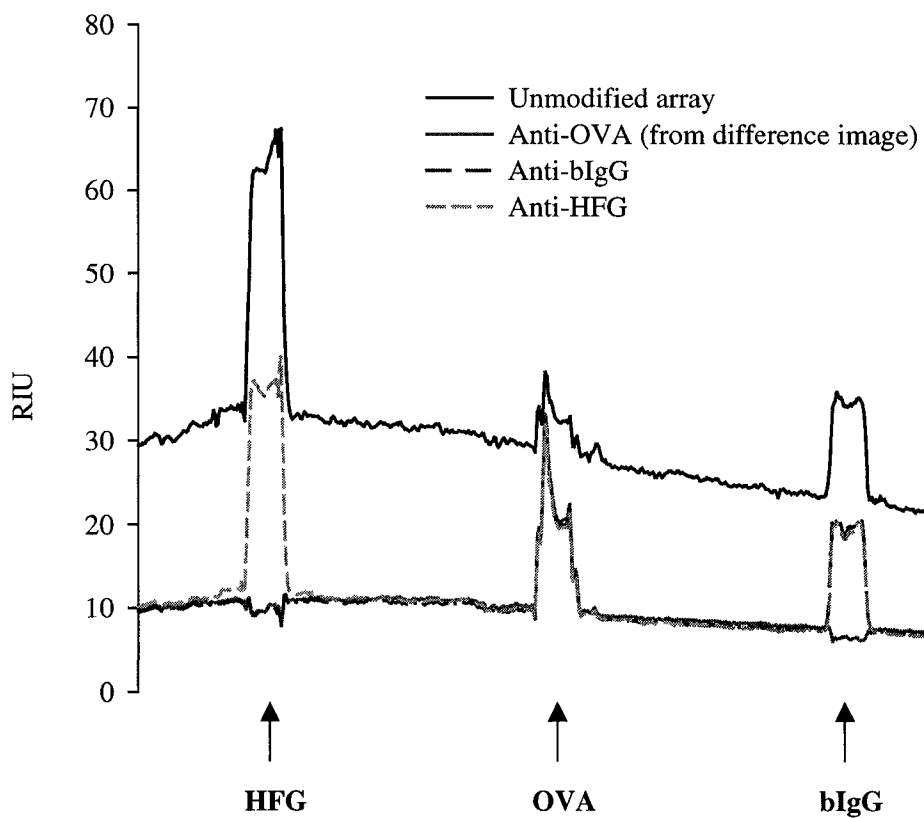


Figure 3.03. Column profiles show changes in total signal after exposure of the array to antibodies.

subsequent cross-sections show no change in their baselines. The attribution of the unchanging baseline to blocking of subsequent background antibody adsorption after the initial exposure rather than to the development of a steady-state equilibrium is borne out by the fact that the antibodies were present at different concentrations. Hence, if the antibodies were reversibly binding to the surface so as to maintain surface coverages proportional to their solution concentrations, the baseline would shift. Even in the case of a mixed Tween 20/antibody layer maintaining a steady state solution-surface equilibrium for changing antibody concentrations, any difference in refractive index or thickness between the surfactant ($n=1.468$)²⁶ and the protein ($n=1.45-1.55$)^{19, 27} could potentially cause some shift. Note that after the first exposure, the shifts in the levels of the other proteins had also increased, though to a slightly lower degree than the background. The conclusion reached was that the initial antibody exposure using this method created a barrier layer over the background, and had an indeterminate effect on the other arrayed antigens.

In an effort to counter these problems, BSA was used to block the surface against non-specific adsorption prior to antibody exposures. BSA is a ubiquitous blocking agent in surface assays.²⁸ Figure 3.04 shows two difference images of a four-protein array after exposures to anti-bIgG and anti-HFG. The difference image in Fig. 3.04(A) shows the expected increase in intensity at the bIgG line after exposure to the complementary antibody. After exposure of the array to anti-HFG, it is apparent that not only was an increase in the signal at the HFG line observed, but a significant increase was caused to the BFG line as well. This pointed to a cross-reactivity between the two species' fibrinogens. The cross-sections in Fig. 3.03(C) show that the BSA blocking caused

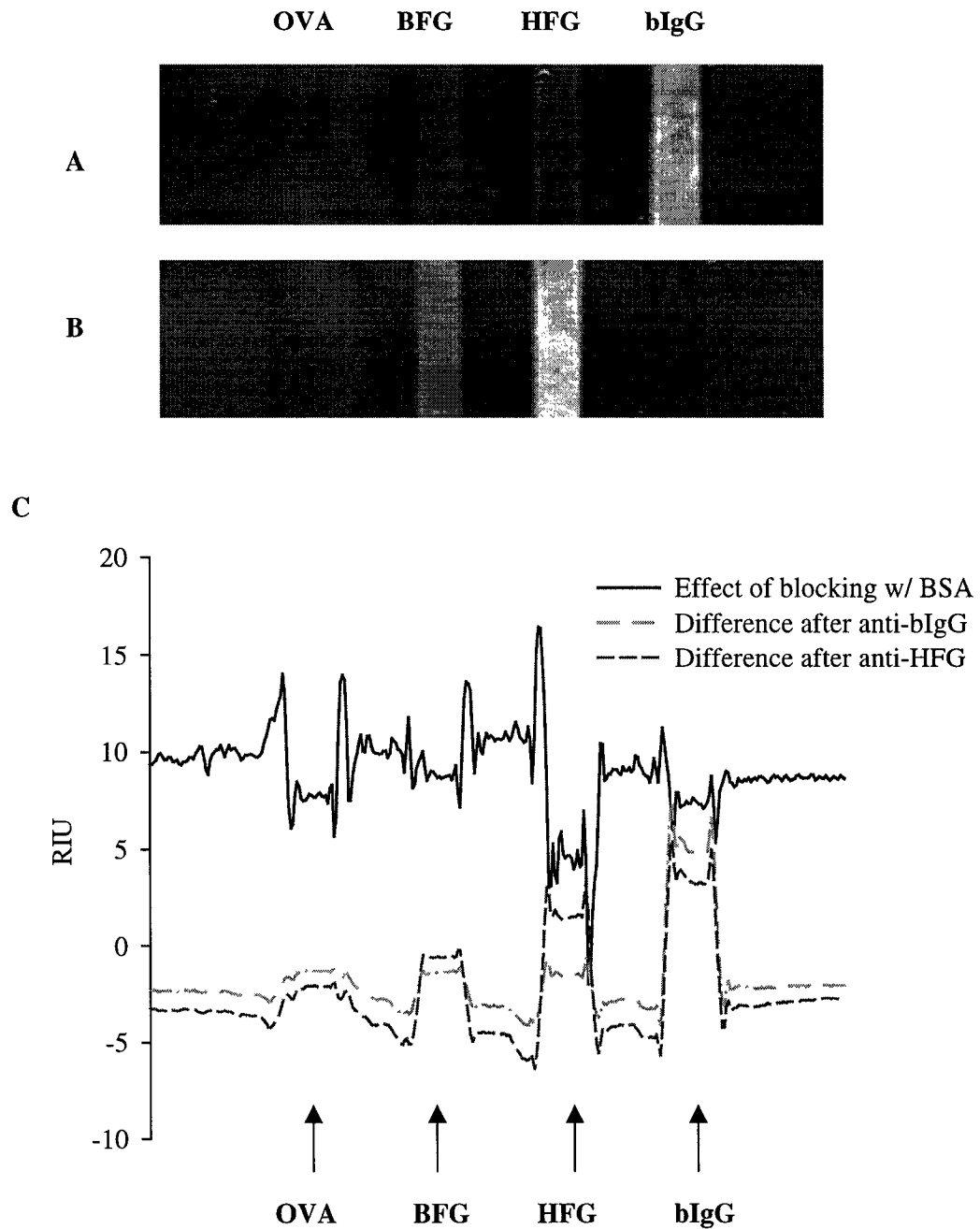


Figure 3.04. Effect of blocking surface with BSA (A) Difference image after binding of anti-bIgG. (B) Difference image after exposure to anti-HFG, showing cross-reactivity with BFG. (C) Cross-sectional profiles.

increases on the protein regions once again. The differences in the increases among the different proteins may have been caused by the different surface coverages and/or differential susceptibilities to displacement by the BSA. The cross-sectional profiles showing the differences after antibody adsorption, again from PBS^T, have a decreasing baseline signal. This may be due to the slow removal of weakly bound BSA after multiple solutions and rinses with PBS^T. More likely, however, is the possibility of shift in the refractive index of the solution. As was seen in Figure 3.03, the solution exposure steps did not remove the protein antigens. One possible reason for this may have been the drying step between the fabrication of the array and the placement of the sensor chip in the SPR imager under buffer. The time for this transfer was typically less than 5 min. Given previous experience with ex-situ BSA blocking, it was expected that such a procedure would result in a surface with uneven BSA distribution. In order to achieve a stable background level for SPR measurements, a new patterning approach was employed.

Slight changes in refractive index during the course of an experiment could lead to undesirable shifts in the baseline position. In addition, a BSA blocking layer deposited from a high concentration solution, as is conventional, may not be stable over the course of an experiment. While this is not a factor when using labelled reporter molecules in immunoassays, a change in surface mass concentration of BSA during numerous rinsing and reagent introduction steps would result in a shifting baseline in SPR imaging. As such, a surface chemistry highly impervious to protein adsorption would be of great use in establishing a reference plane within the images. Given that monolayers of alkylthiolates containing oligoethylene glycol groups have been demonstrably effective

in resisting protein adsorption at gold surfaces,^{29, 30} EG3-OMe was employed to give a strongly protein-resistant background region. In addition to the incorporation of an invariant reference plane, the experimental design took into consideration the need to adsorb proteins to the surface without a high degree of conformational perturbation. Drawing on the use of polyamines in assays which require proteins to be bound via physisorption,^{9, 31} an amine-terminated monolayer^{9, 31} was used to localize adsorbing antigens from solution. MUAM SAMs were observed to adsorb larger amounts of protein than either methyl or carboxylate terminal SAMs.

Arrays of antigenic proteins were fabricated using microfluidic channels formed in PDMS as shown in Fig. 3.05. First, a PDMS microchannel device was brought into conformal contact with the gold surface of the chip. Figure 3.05(A) shows how a 3.5 to 7 mM aqueous solution of MUAM was introduced into all channels in order to form a monolayer. The thiol molecules were adsorbed for 10 min., the channels rinsed with water and the PDMS removed from the gold. This resulted in a pattern of 200 μm wide lines of amine-terminated monolayer on the chip surface. Prior experience had shown that using aqueous solutions within the channels was the best means of preserving the conformal seal between the PDMS and the gold substrate. The substrate was then immersed in an ethanolic solution of EG3-OMe for at least 8 h to modify the remaining gold surface with a layer that resists protein adsorption, as indicated in Fig. 3.05(B). After removing the chip from the EG3-OMe solution, rinsing and drying, a second PDMS microchannel device was placed with its channels perpendicular to the $-\text{NH}_2$ lines (Fig. 3.05(C)). Different protein solutions (100 $\mu\text{g}/\text{mL}$ in PBS) were introduced to each channel and the proteins physisorbed for 1 h. Due to the protein resistant nature of the

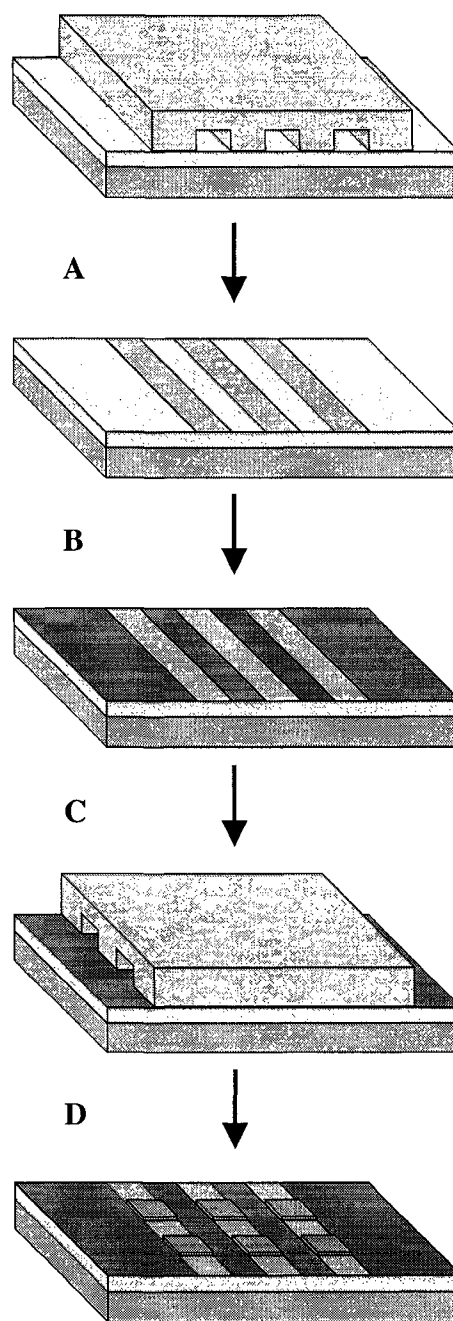


Figure 3.05. Surface patterning via microfluidic channels (μ FCs) in PDMS. (A) Monolayers are patterned through μ FCs. (B) Gold is backfilled with EG3-OMe. (C) Second set of μ FCs is placed perpendicular to patterned lines. (D) Proteins are patterned across lines via μ FCs.

EG3-OMe monolayer, adsorption of the antigen proteins occurred primarily to the $-NH_2$ terminal MUAM regions, as described by Fig. 3.05(D). Thus, the microfluidic channels were used to confine the adsorption of the antigens in one direction and the patterned surface chemistry to control adsorption perpendicular to the channels. This procedure resulted in a chip featuring spots of physisorbed protein supported on an amine-terminated monolayer.

A SPR image of a chip containing spots of three proteins is shown in Figure 3.06(A). The localized adsorption of antigen proteins to regions of the MUAM monolayer generates a change the refractive index at the solid surface, resulting in the observed pattern of contrast. A solution of ~ 133 nM polyclonal anti-goat IgG was introduced into the flow cell for 10 min. After flushing the cell with PBS, the image in Figure Figure 3.06(B) was collected. The net result of the anti-goat IgG binding to the chip is more apparent in the difference image of Figure 3.06(C), which was produced from the subtraction of Figure 3.06(A) from Figure 3.06(B). The results contained in Figure 3.06 are explored quantitatively in Figure 3.07.

SPR signal intensities can be measured from cross-sectional profiles. Figure 3.07 contains the difference image following anti-gIgG binding shown in Figure 3.06(C) as well as several cross sections collected along various lines through the image. Cross-sections A, B and C correspond to the SPR signal increase observed on the gIgG, bIgG and BSA spots, respectively. The largest signal increase for anti-gIgG binding occurs, as expected, at the immobilized gIgG spots (42 ± 12 RIU over 4 spots). A significant signal (26 ± 7 RIU) is also observed at the bIgG spots due to cross reactivity with the anti-gIgG. The polyclonal anti-goat IgG used here is directed against whole IgG and may bind to

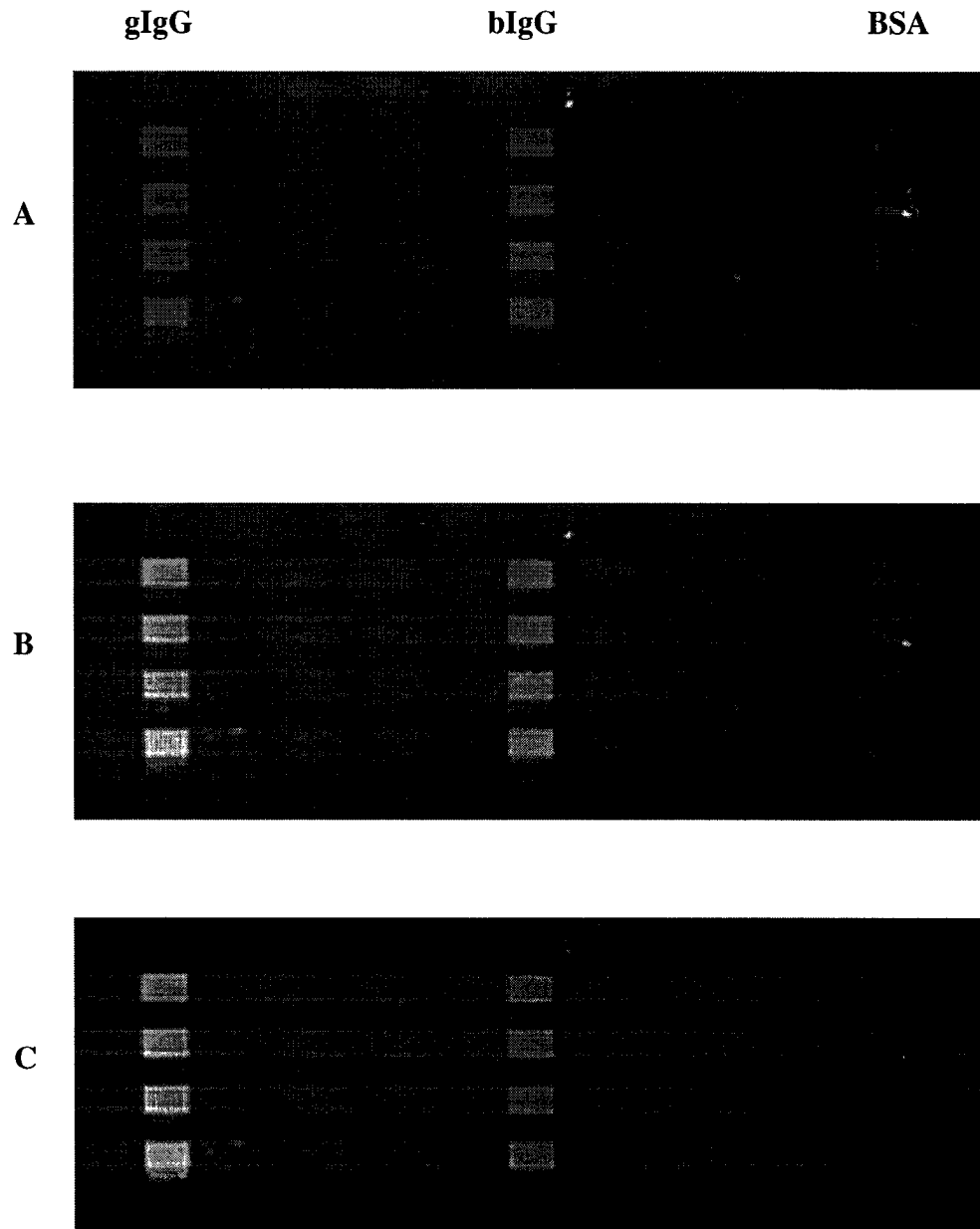


Figure 3.06. (A) Three proteins patterned across MUAM lines with an EG3-OMe background. (B) Image after binding of anti-bIgG. (C) Difference image showing inter-species cross-reactivity with gIgG. Note the low level of binding at the BSA spots.

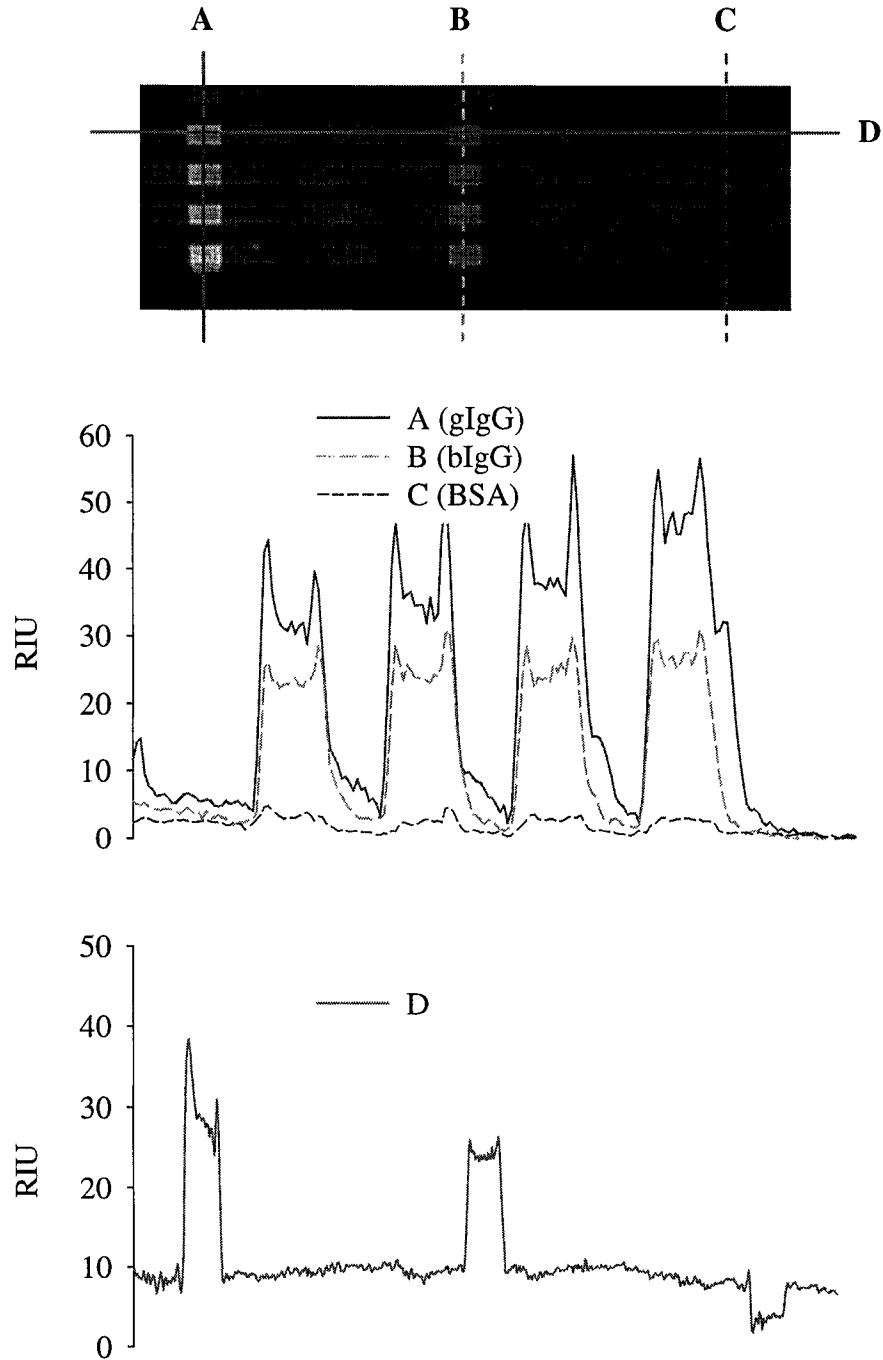


Figure 3.07. Line profiles of the anti-gIgG difference image show (A) that the target was bound, (B) significant cross-reactivity with bIgG and (C) that non-specific adsorption to the BSA was minimal. The horizontal line profile (D) shows the relative increase in signal due to physisorption of the antibody on the MUAM lines.

epitopes common among the IgGs of different animal species so this cross reactivity is expected. A negligible signal change is observed at the BSA spots (3 ± 3 RIU), suggesting minimal non-specific binding to the protein spots.

It is crucial that the background signal of the chip remains low following antibody exposure for sensitive and accurate quantitative binding analysis. Although the earlier experiments gave reasonable results with a 1 hour blocking step, it was desirable to have a background region whose signal level was independent of protein exposure and rinsing steps. In profiles A and B, the signal in the regions between and outside the spots is generally less than 2 RIU due to the resistance of the EG3-OMe groups to non-specific protein adsorption. This is contrasted by profile D, which traces along a MUAM line. The regions between spots in profile D show significant signal (~ 10 RIU) due to the non-specific adsorption of anti-IgG to the amine-terminated monolayer. Importantly, the use of EG3-OMe to give a reference plane allowed the use of antibody solutions diluted in PBS with no added surfactants. As a result, the changes in the baseline are minimized and can, even in the case of changes in solution refractive index, be used as a baseline signal level.

Figure 3.08 demonstrates that our chip chemistry and detection method function well for sequential sample solution introductions. Following the incubation in unlabeled anti-IgG, the array was exposed to $5.8 \mu\text{M}$ anti-BSA. The difference image in Fig. 3.08 shows a large signal change at the BSA spots (57 ± 17 RIU) and negligible signal on the other spots indicating exclusive binding to the immobilized BSA. The signal at the EG3-OMe regions remains low (< 2 RIU) reflecting minimal nonspecific adsorption to the background after multiple successive antibody solutions.

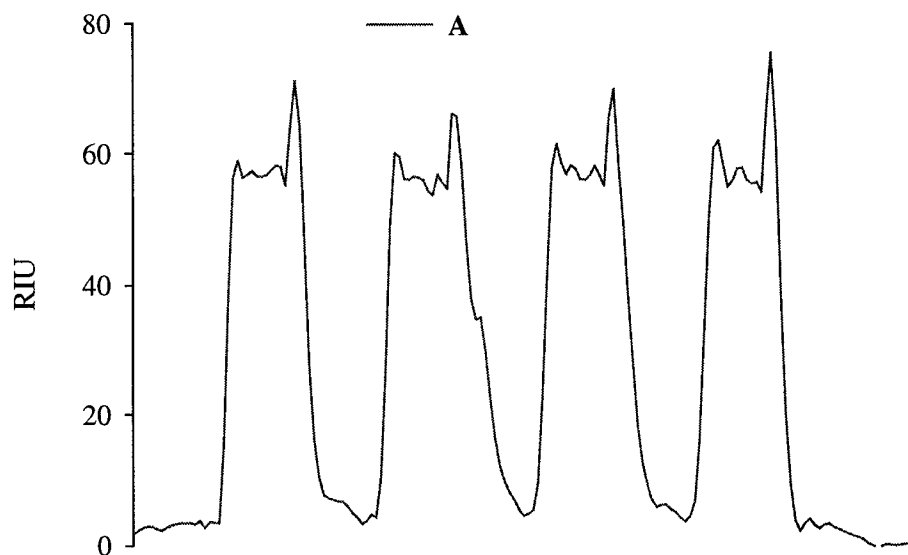
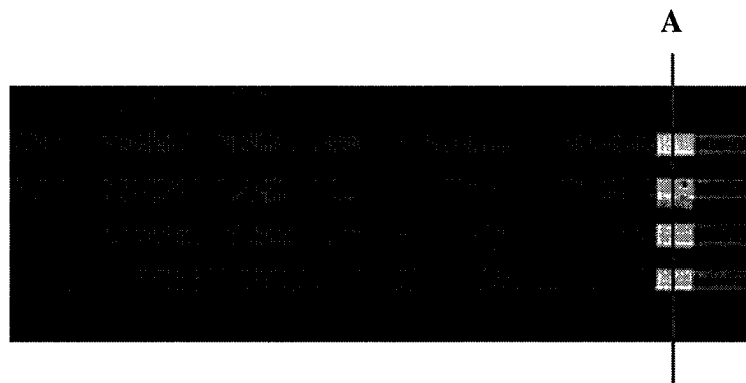


Figure 3.08. The line profile (A) following the binding of anti-BSA to the same array from Figure 3.07 shows the utility of the array for sequential antibody introductions.

The unique advantage of biomolecule arrays is in the ability to simultaneously monitor interactions between a number of different immobilized array elements and solution species. This enables, for example, the optimization of conditions for immobilization of biomolecules in the microarray.¹⁵ In our antibody capture format, we explored the effect of the surface density of the immobilized antigen on the antibody capture. The surface density can be simply controlled by varying the antigen concentration in solution. An array was prepared consisting of bovine IgG immobilized from solutions of different concentrations. Figure 3.09 shows an SPR image of such an array after exposure to 667 nM of anti-bovine IgG and rinsing with PBS. As shown in the cross-sectional profile, the amount of antibody binding that is detected scales with the solution concentration used to deposit the antigen and thus the surface density of antigen. A number of covalent schemes,^{2, 32, 33} specific interactions requiring fusion proteins^{13, 17} as well as nonspecific physisorption^{9, 34, 35} have been used to immobilize proteins in microarrays. It is notable that the method applied here, simple physisorption to an amine-terminated monolayer, can be used to predictably control the surface density of arrayed proteins and thus optimize the observed readout signal.

Single channel SPR is widely employed to measure binding strength of biological interactions.³⁶ Isotherms were constructed for the binding of anti-bIgG to immobilized bIgG arrayed as shown in Figure 3.09(A). Line profiles of the immobilized bovine IgG elements were integrated for increasing concentrations of anti-bovine IgG. These isotherms are shown in plots of changes in percent reflectivity ($\Delta\%R$) vs. antibody

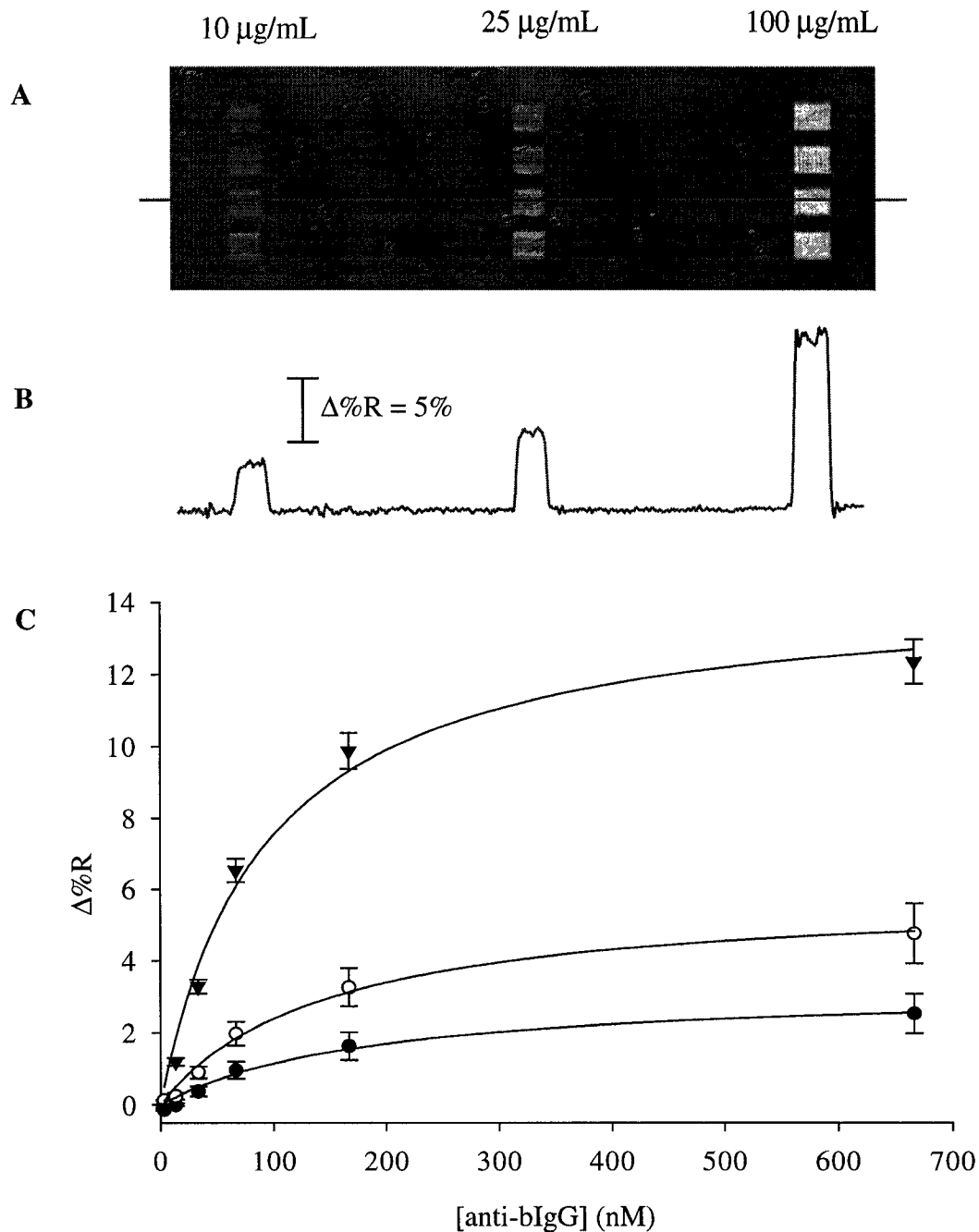


Figure 3.09. (A) SPR difference image of bIgG arrayed at three concentrations after adsorption of 667 nM anti-bIgG. (B) Line profile shows relative magnitudes of antibody binding. (C) Langmuir fits to antibody binding data for spots from each solution bIgG concentration: 10 (filled circles), 25 (open circles) and 100 µg/mL (filled triangles).

concentration in Figure 3.09(C). The value of %R, or $\Delta\%R$ in the case of difference images, is obtained from the reflected intensity units (RIU) by the following equation:³⁷

$$\%R = \frac{0.85I_p}{I_s} \times 100\% \quad (3.1)$$

where I_s refers to the light intensity detected using s-polarized light. Given that s-polarized radiation will not couple to surface plasmons, I_s gives the maximum reflectivity value at a given viewing angle. Therefore, the maximum reflectivity is obtained by capturing the image of a surface viewed with s-polarized light.

A convenient way to deduce binding constants is by fitting of adsorption signal changes over a range of concentrations to the Langmuir adsorption isotherm

$$\theta = \frac{\Delta\%R}{\Delta\%R_{\max}} = \frac{K_{\text{ads}}[A]}{1 + K_{\text{ads}}[A]} \quad (3.2)$$

where θ is the signal as a fraction of the maximum $\Delta\%R_{\max}$ is the asymptotic maximum value of the difference signal, K_{ads} is the adsorption coefficient, and $[A]$ represents the solution concentration of the adsorbate. Wegner et al. demonstrated that SPR imaging could be used to measure binding isotherms and determine adsorption coefficients (K_{ads}), which are inversely related to dissociation constants obtained by the fitting of data to the Langmuir equation.¹⁷ When $\theta=0.5$, equation 3.2 can be solved for the solution concentration of adsorbate corresponding to half-maximal surface coverage. At this

concentration, $[A]=K_{ads}^{-1}$; thus, the value of the adsorption coefficient corresponds to the inverse of the concentration at half-saturation coverage. Fitting parameters for the binding curves are listed in Table 3.1.

Two observations are noteworthy from the plots in Figure 3.09(C). First is that the maximum amount of antibody binding is governed by the surface density of antigen. This implies that SPR signals are mainly due to antibody-antigen interactions with little contribution from nonspecific adsorption. We would expect that the steric limit for maximum antibody coverage would be similar for a nonspecifically adsorbed layer and a layer that was specifically bound to antigen. Thus, if the observed SPR signals were due to a combination of nonspecific adsorption and specific binding, the maximum $\Delta\%R$ for each antigen spot type would be similar in Figure 3.09(C). In addition, the ability to control signal levels by varying the surface densities of the array elements is especially useful for SPR imaging detection as the signal is linear with surface concentration only for $\Delta\%R$ of about 10% or less.³⁸

Secondly, K_{ads} values determined from the Langmuir fit increase with increasing surface density of antigen. Although the magnitude of $\Delta\%R$ at the spots prepared from 667 nM bovine IgG slightly exceeds 10% and K_{ads} for those data is less accurate, the trend is borne out even with exclusion of the single offending point. Smith et al. have noted that while K_{ads} values obtained from Langmuir fits are not equivalent to binding association constants, K_{ads} values can be used to rank binding strengths in similar systems.¹⁶ Thus, the trend in K_{ads} from Figure 3.09(C) implies stronger antibody binding to spots with a higher surface density of antigen. This may be due to variations in the orientation or conformation of the adsorbed antigens as a function of surface density.

Solution [bIgG] ($\mu\text{g/mL}$)	K_{ads} (M^{-1})	$\Delta\%R_{\text{max}}$	R^2
10	$5.3(1.3) \times 10^{-6}$	3.3 (0.3)	0.91
25	$6.9(1.2) \times 10^{-6}$	5.9 (0.4)	0.94
100	$1.09(0.10) \times 10^{-7}$	14.4 (0.5)	0.98

Table 3.1. Curve-fitting parameters for anti-bIgG binding curves. Values in parentheses are standard deviations of the indicated values.

The finding is also consistent with a recent report showing that the affinity between immobilized antibodies and their antigens increases at high surface density.³⁹ The postulated reason for the change was a decrease in the apparent dissociation rate constant at higher surface densities due to the decreasing diffusion distances between adsorption sites for a dissociated antibody. Figure 3.09 shows that microarrays with controlled surface density of antigens can be fabricated using PDMS microfluidic networks and patterned monolayer substrates. SPR imaging provides both quantitative and qualitative evaluation of antibody binding in a label-free format.

4. Conclusions

A simple method for the fabrication and reading of antigen microarrays was demonstrated. This work provides further demonstration of the use of SPR imaging for label free reading of microarrays. The use of self-assembled monolayers and microfluidic networks enabled the patterning of surface chemistry to support proteins in array elements and created a background plane on which there was a very low level of non-specific adsorption. The differential imaging technique employed was able to study antibody binding and cross-reactivity while confirming the absence of non-specific adsorption for multiple solution exposures to the chip. We have studied the effect of bovine IgG surface density on SPR imaging signal changes upon polyclonal anti-bovine IgG binding. The affinity between the immobilized bIgG and its antibody increases with antigen surface density.

5. References

- (1) Ngo, T. T., Ed. *Nonisotopic Immunoassay*; Plenum Press: New York, 1988.
- (2) MacBeath, G.; Schreiber, S. L. *Science* **2000**, *289*, 1760-1763.
- (3) Sapsford, K. E.; Charles, P. T.; Patterson Jr., C. H.; Ligler, F. S. *Anal. Chem.* **2002**, *74*, 1061-1068.
- (4) Angenendt, P.; Glokler, J.; Sobek, J.; Lehrach, H.; Cahill, D. J. *J. Chrom. A* **2003**, *1009*, 97-104.
- (5) Schultz, S.; Smith, D. R.; Mock, J. J.; Schultz, D. A. *Proc. Natl. Acad. Sci. USA* **2000**, *97*, 996-1001.
- (6) Chan, W. C. W.; Nie, S. *Science* **1998**, *281*, 2016-2018.
- (7) Chard, T. *Introduction to Radioimmunoassay and Related Techniques*; Elsevier: New York, 1995.
- (8) Rowe, C. A.; Scruggs, S. B.; Feldstein, M. J.; Golden, J. P.; Ligler, F. S. *Anal. Chem.* **1999**, *71*, 433-439.
- (9) Kusnezow, W.; Hoheisel, J. D. *J. Mol. Recognit.* **2003**, *16*, 165-176.
- (10) Wang, Z. H.; Jin, G. *Anal. Chem.* **2003**, *75*, 6119-6123.
- (11) Winson, D. S.; Nock, S. *Angew. Chem. Int. Ed.* **2003**, *42*, 494-500.
- (12) Wilchek, M.; Miron, T. *J. Biochem. Biophys. Methods* **2003**, *55*, 67-70.
- (13) Zhu, H.; Bilgin, M.; Bangham, R.; Hall, D.; Casamayor, A.; Bertone, P.; Lan, N.; Jansen, R.; Bidlingmaier, S.; Houfek, T.; Mitchell, T.; Miller, P.; BDean, R. A.; Gerstain, M.; Snyder, M. *Science* **2001**, *293*, 2101-2105.

- (14) Delamarche, E.; Bernard, A.; Schmid, H.; Michel, B.; Biebuyck, H. *Science* **1997**, *276*, 779-781.
- (15) Wegner, G. J.; Lee, H.-J.; Corn, R. M. *Anal. Chem.* **2002**, *74*, 5161-5168.
- (16) Smith, E. A.; Thomas, W. D.; Kiessling, L. L.; Corn, R. M. *J. Am. Chem. Soc.* **2003**, *125*, 6140-6148.
- (17) Wegner, G. J.; Lee, H.-J.; Marriott, G.; Corn, R. M. *Anal. Chem.* **2003**, *75*, 4740-4746.
- (18) Knoll, W. *Annu. Rev. Phys. Chem.* **1998**, *49*, 569-638.
- (19) Brockman, J. M.; Nelson, B. P.; Corn, R. M. *Annu. Rev. Phys. Chem.* **2000**, *51*, 41-63.
- (20) Morrill, P. R.; Millington, R. B.; Lowe, C. R. *J. Chrom. B* **2003**, *793*, 229-251.
- (21) Su, J.; Mrksich, M. *Angew. Chem. Int. Ed.* **2002**, *41*, 4715-4718.
- (22) Grow, A. E.; Wood, L. L.; Claycomb, J. L.; Thompson, P. A. *J. Microb. Meth.* **2003**, *53*, 221-233.
- (23) Harlow, E.; Lane, D. P. *Antibodies: A Laboratory Manual*; Cold Spring Harbor Laboratory: Cold Spring Harbor, NY, 1988.
- (24) Pale-Grosdemange, C.; Simon, E. S.; Prime, K. L.; Whitesides, G. M. *J. Am. Chem. Soc.* **1991**, *113*, 12-20.
- (25) Xia, Y.; Whitesides, G. M. *Angew. Chem. Int. Ed.* **1998**, *37*, 550-575.
- (26) *Aldrich Catalogue Handbook of Fine Chemicals*; Sigma-Aldrich Canada Ltd., 1998-1999.
- (27) Fischer, B.; Heyn, S. P.; Egger, M.; Gaub, H. E. *Langmuir* **1993**, *9*, 136-140.

- (28) Christofides, N. D. In *The Immunoassay Handbook*, 2nd ed.; Wild, D., Ed.; Nature Publishing Group: New York, 2001, pp 61-77.
- (29) Prime, K. L.; Whitesides, G. M. *Science* **1991**, *252*, 1164-1167.
- (30) Harder, P.; Grunze, M.; Dahint, R.; Whitesides, G. M.; Laibinis, P. E. *J. Phys. Chem. B* **1998**, *102*, 426-436.
- (31) Chen, S.; Liu, L.; Zhou, J.; Jiang, S. *Langmuir* **2003**, *19*, 2859-2864.
- (32) Ng, H. T.; Fang, A.; Huang, L.; Li, S. F. Y. *Langmuir* **2002**, *18*, 6324-6329.
- (33) Levit-Binnun, N.; Lindner, A. B.; Zik, O.; Eshhar, Z.; Moses, E. *Anal. Chem.* **2003**, *75*, 1436-1441.
- (34) Soeng, S.-Y. *Clin. Diagn. Lab. Immunol.* **2002**, *9*, 927-930.
- (35) Angenendt, P.; Glokler, J.; Konthur, Z.; Lehrach, H.; Cahill, D. J. *Anal. Chem.* **2003**, *75*, 4368-4372.
- (36) Rich, R. L.; Myszka, D. G. *J. Mol. Recognit.* **2003**, *16*, 351-382.
- (37) Weibel, S.; GWC Instruments, Madison, WI; personal communication to author, 2004.
- (38) Nelson, B. P.; Grimsrud, T. E.; Liles, M. R.; Goodman, R. M.; Corn, R. M. *Anal. Chem.* **2001**, *73*, 1-7.
- (39) Giraudi, G.; Rosso, I.; Baggiani, C.; Giovannoli, C. *Anal. Chim. Acta* **1999**, *381*, 133-146.

Chapter IV

Surface Plasmon Resonance Imaging of Protein-Carbohydrate Interactions

1. Introduction

In recent years, much research effort has been directed at the development of microarray methods for the parallel analysis of interactions in proteomics and genomics. In addition to these widely known areas of research, there is a growing interest in the analysis of biological interactions mediated by carbohydrates, or “glycomics”.^{1, 2} The expansion of research efforts in this area is being driven by the growing interest in the role carbohydrate ligands play in mediating various biological phenomena. Research has unraveled a large, diverse family of carbohydrate-mediated interactions between cells and viruses, bacteria, extracellular matrix scaffolds and other cells.³ Cell surfaces can interact with other cells through a variety of interactions involving membrane-bound and extracellular oligosaccharides, glycolipids and glycoproteins.

Among the barriers to entry in the study of carbohydrates is the relative structural complexity of carbohydrate ligands. The presence of multiple branching points, stereochemistry, and functional group modifications in natural systems introduces a higher degree of synthetic difficulty for oligosaccharides in comparison to oligonucleotides and linear polypeptides.^{4, 5}

Much of the functional activity of carbohydrates is governed by highly specific recognition with proteins. Increasing interest in examining the functional characteristics

of carbohydrate ligands as well as the need for throughput and efficiency in the analysis of carbohydrate interactions is leading to a surge in microarray research.^{2, 6-9} The sheer variety of structures and interactions would seem to make a high throughput analysis system such as microarrays a necessity for expansion of research into glycomics.

Lectins are a class of proteins which function as receptors for specific carbohydrate moieties.^{4, 10, 11} The interactions of individual carbohydrate moieties with proteins are weak, with typical dissociation constants in the high micromolar to millimolar range.^{12, 13} As a consequence, many lectins interact with their targets via multiple, homologous binding sites in order to increase affinity. A well-studied example is that of the influenza virus, which binds to cell-surface sialic acids via a homotrimeric lectin group. The initial binding allows other lectin groups on the viral surface to come into contact with more cell-surface sugars, eventually deforming the cell membrane and leading to endocytosis.³ In this chapter, SPR imaging is used to probe two classes of carbohydrates involved in the recognition-mediated virulence of well-known bacterial families.

SPR has previously been applied to the elucidation of binding constants for various carbohydrate-protein interactions.¹⁴ Much research into carbohydrate-protein interactions focuses on the analysis of lectins associated with pathogens.^{3, 15} Some noteworthy examples which have been studied by SPR include the binding of HIV-1 protein gp120 to potential inhibitors comprised of glycodendrimers and sulfated dextran,¹⁶ the binding of the toxin ricin to various synthetic glycolipids^{17, 18} and the interactions of cholera toxin with ganglioside receptors.^{19, 20} The sensitivity and perceived accuracy of the analytical data from SPR measurements, as well as the ease of

use of the popular Biacore instrumentation, have allowed researchers to ascertain binding constants from analysis of kinetic data.

While lectins and their analogues constitute a multivalency-based approach to carbohydrate recognition, the development of high-affinity antibodies for targeting single residues would be advantageous for targeting less densely distributed carbohydrates as well as for immunoassays and therapeutic applications. While IgG antibodies can also engage in bivalent binding via two identical binding sites, the possibility exists for the enhancement of affinities via somatic mutations. Three disaccharides presented by the cell surface of *Salmonella* were used to determine the binding specificity and strength of the monoclonal antibody Se155-4. The epitopes defined by the terminal saccharides were associated with each of serogroup A, B, and D₁ *Salmonella*. This particular antibody was the first to have been characterized in a bound conformation with its carbohydrate target via X-ray crystallography.²¹ The study of this system by SPR imaging would allow for evaluation of the binding characteristics in a heterogeneous assay somewhat analogous to the cell-surface. In addition, this assay would help to determine the utility of the antibody line in assays and therapeutic applications.

The *Escherichia coli* bacterium produces toxins implicated in a number of gastrointestinal maladies including diarrhea, hemorrhagic colitis and the hemolytic uremic syndrome.²² The verotoxins belong to a class of toxins also known as Shiga-like toxins (SLTs) due to their structural similarity to the Shiga-toxin produced by *Shigella dysenteriae* type I. The *E. coli* toxins consist of a 38.4 kDa pentameric B₅ subunit, which is responsible for the recognition of cell-surface oligosaccharide units, and a 32 kDa enzyme portion, the A subunit, which damages ribosomal RNA once internalized by the

cell.²³ The cell surface recognition is a necessary step in allowing the toxin to be internalized and, hence, fulfill its enzymatic function. It has been shown that the binding sites of the B₅ subunit can be blocked with synthetic ligands containing multiple copies of the P^k trisaccharide unit.²³ The five-fold quasi-symmetric ligands can bind to all five of the strong binding sites on the B₅ subunit simultaneously, effectively inhibiting the toxin.^{23, 24} This well-characterized system is used to establish the utility of SPR imaging for studies of binding inhibition.

2. Experimental

The synthesis of HS(CH₂)₁₁(OCH₂CH₂)₃OCH₃ (EG3-OMe) was described in the previous chapter. A brief description of the synthesis of 11-mercaptoundecanol (MUO)²⁵ follows. 11-Bromo-1-undecanol (Aldrich) was refluxed with a slight excess of thiourea for 6 h. The mixture was further refluxed for a few hours with 2.5 equiv. NaOH to give MUO. MUO was purified by flash chromatography on silica gel using 2% MeOH in CH₂Cl₂ as eluent.

The alkythiol- or alkyldisulphide-modified saccharides and inhibitors were synthesized by the research group of Prof. D. R. Bundle (University of Alberta) for use in this work. The recombinant Shiga-like toxin (SLT) was expressed without the enzymatic A subunit, leaving only the self-assembling B₅ subunit containing the carbohydrate recognition sites. 1.6 mg/mL SLT was received in PBS with 0.02% NaN₃ as preservative. The monoclonal antibody Se155-4 (MAb) was received in 6.15 mg/mL solution in 0.05 M Tris buffer with 0.15 M NaCl and 0.02% NaN₃. The SLT and Se155-

4 were gifts from Prof. D. R. Bundle. All protein solutions were diluted in phosphate-buffered saline (PBS: 8.1 mM Na₂HPO₄, 1.5 mM KH₂PO₄, 137 mM NaCl, 2.7 mM KCl in 18M Ω water).

Poly(dimethylsiloxane) (PDMS) microfluidic channels were fabricated according to established methods.²⁶ Briefly, a relief pattern of photoresist on a silicon wafer was created photolithographically. By curing polydimethylsiloxane prepolymer and cross-linker (Sylgard 184, Dow Corning; Midland, MI) 10:1 by weight against this relief structure, a negative of the relief was formed in the PDMS. The microchannels measured 200 μ m wide by 10-15 μ m deep. The device was also through-bored at the ends of the channels to allow fluids access to the channels when the PDMS device was applied to a surface. Fluid flow was driven by applying vacuum to one access point on the microchannel while connecting the other access point to a reservoir of solution. Gold surfaces were modified by exposure to the thiols or disulphides in 1:9 H₂O:MeOH. This solvent ratio allowed for facile solubilization of the thiols and sealing of native PDMS microchannels against the gold sensor surface for 20 minutes. The degree of monolayer formation, while expected to be nearly complete over this time scale, was deemed uncritical due to the dilution of the monolayer by MUO and longer-term annealing of defects by immersion in a solution of EG3-OMe.

All SPR imaging utilized sensing films consisting of 45 nm gold films deposited on SF10 glass (Schott; Toronto, ON, Canada) with a 1 nm adhesive layer of chromium. Imaging was performed using the GWC Instruments SPRImager (GWC Instruments; Madison, WI). Images were averages of 100 individual snapshot images; accompanying image profiles are directional averages over the entire displayed image. Gold substrates

for infrared reflection absorption spectroscopy (IRRAS) were prepared by sputtering 10 nm Ti and 300 nm Au onto clean glass microscope slides. IRRAS spectra were collected on a Mattson Infinity spectrometer with an externally housed low noise MCT-A detector at a resolution of 2 cm^{-1} . SAMs containing saccharide moieties were prepared by pressing a liquid film between a clean glass slide and a gold slide in order to confine the small volume (50-200 μL) of solution.

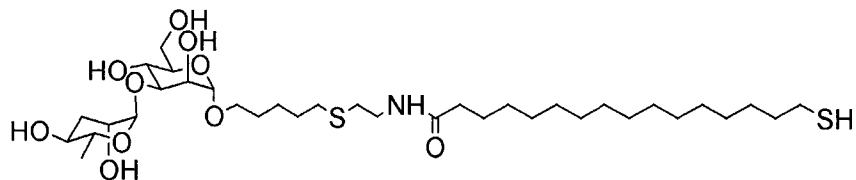
3. Results and Discussion

3.1. Binding of Se155-4 antibody to *Salmonella* epitopes.

The structures of the three *Salmonella* epitopes studied are shown in Figure 4.01. The complementarity-determining moiety is the terminal 3,6-dideoxyhexose, which varies slightly in structure in each of the epitopes shown. The Se155-4 monoclonal antibody has been shown to bind to the SMA-17 epitope, which is presented on the cell surfaces of serogroup B.^{21, 27}

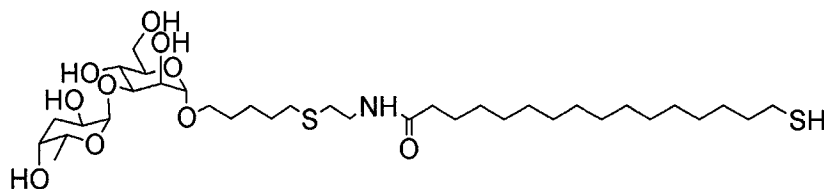
The binding of the MAb was examined on mixed SAMs formed from solutions with varying proportions of SMA-17 and MUO. The variation in antigen density on the surface was examined in order to ascertain an optimal density. The results of SPR imaging of arrayed SMA-17 are shown in Figure 4.02. The initial array image under PBS in Fig. 4.02(A) indicates the differences in epitope density visually, showing an increase in light intensity with increasing density. This is due to the greater height of the epitope-containing molecules on the surface compared with the MUO. An interesting feature of Fig. 4.02(A) is the presence of barely visible domain boundaries on the

A



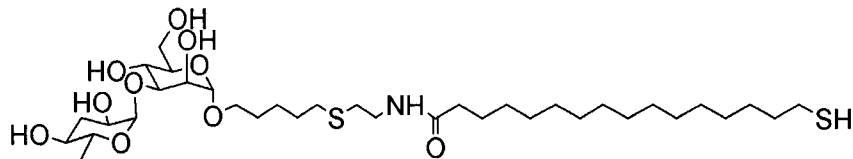
SMA-9; tyvelose

B



SMA-17; abequose

C



SMA-27; paratose

Figure 4.01. Chemical structures of the salmonella epitopes; common names of the terminal saccharides are indicated below each structure. (A) SMA-9, from serogroup D₁ (B) SMA-17, from serogroup B and (C) SMA-27, from serogroup A.

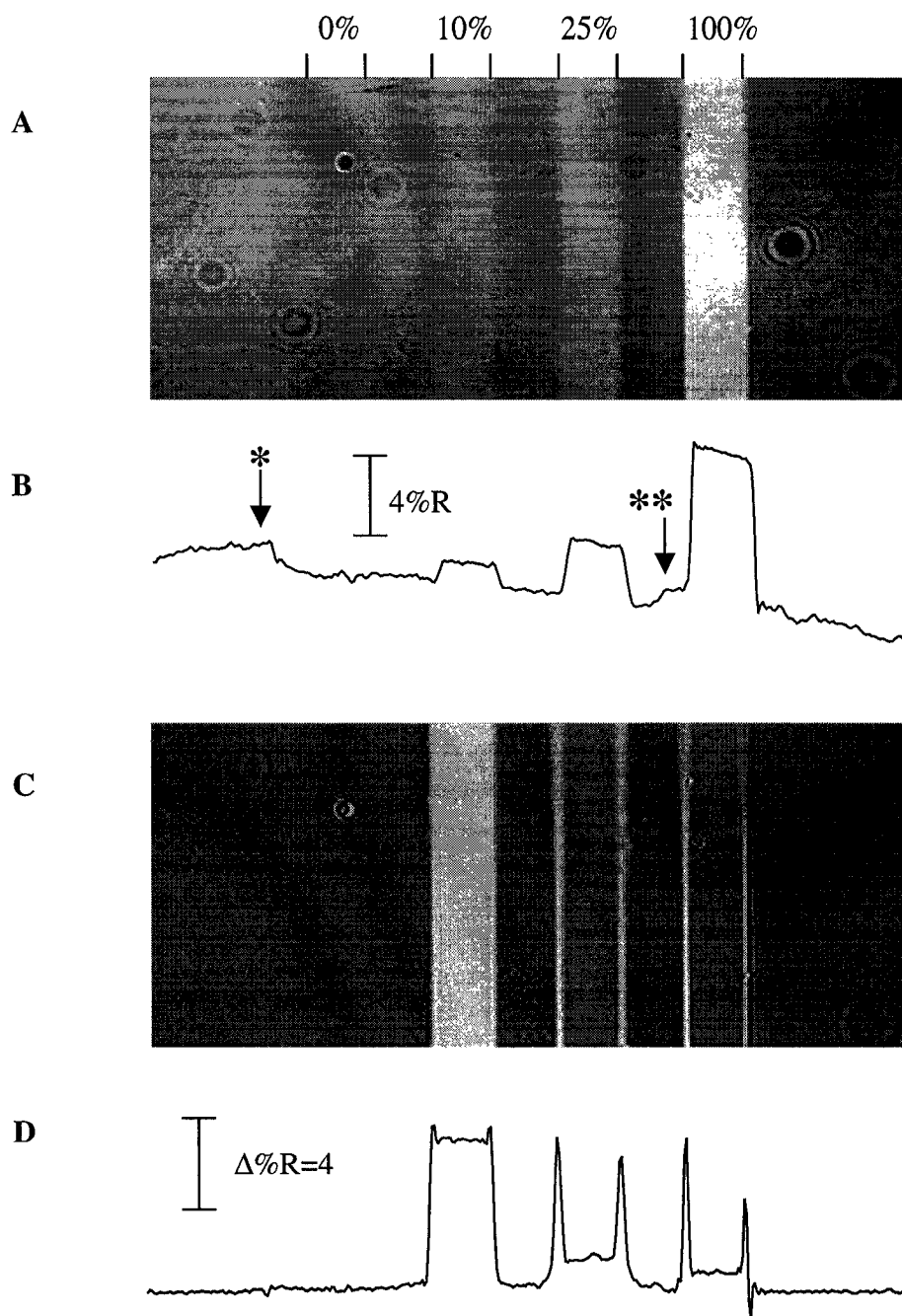


Figure 4.02. (A) SPR image of arrayed SMA-17 at various surface densities. The percentages indicated correspond to the fraction of the total adsorbate concentration comprised of SMA-17 in the forming solution. (B) Cross section showing greater initial signal with increasing SMA-17 concentration. (C) Difference image after exposure of array to 6.15 $\mu\text{g/mL}$ (41 nM) Se155-4 MAb. (D) Cross-section of difference image shows surface-density dependent variations in antibody binding.

background region running parallel to the patterned lines. The arrows marked with asterisks in Fig. 4.02(B) indicate these boundaries as steps in the cross-section. The lower plateau of each of these steps indicates a region in which some MUO had been transferred to the gold substrate beyond the boundaries of the channels by diffusion through the PDMS device during microfluidic patterning. The 100% SMA-17 line contained no MUO; as a result, the areas immediately adjacent to that line are comprised of only EG3-OMe. This is manifested as a higher reflectivity level on these regions than on the regions containing MUO, leading to the step indicated by the double asterisk in Fig. 4.02(B). This loss of pattern resolution was not observed for the saccharide-terminated species due to the presence of the larger hydrophilic groups, which prevented diffusion into the hydrophobic polymer. As a result of the confinement of active species to the geometric areas defined by the microchannels, as well as the observed protein-resistance of MUO, the printing of the MUO did not hinder the analyses performed.

Figure 4.02(C) is a difference image captured after exposure of the array to the Se155-4 MAb. Along with the profile in Fig. 4.02(D), it shows that there was no adsorption to the background regions. It can be seen that on the line consisting of only MUO, there is no observable adsorption; the relative protein resistance of hydroxyl-terminated monolayers has been previously demonstrated. While the resistance to protein adhesion is not as great as with oligo(ethylene glycol)-terminated monolayers, it is sufficient to prevent non-specific adsorption of IgGs at the concentrations used in this work. In addition, the binding of the MAb is maximal at the 10% dilution, and is reduced further as epitope density increases from 25% to 100%. Part of the reason for this may be

steric constraints, since more complete monolayers of SMA-17 may provide a barrier to the incorporation of the disaccharide into the binding site of the MAb.

It has been shown that the binding between Se155-4 and the epitope involves hydrogen-bonding interactions with both of the saccharide groups in a binding pocket 0.8 nm deep by 0.7 nm wide.²¹ More complete monolayers would tend to bury more of these groups, rendering them inaccessible for binding. The tethers on the saccharides used for this study were long enough to allow the protrusion of the epitopes above the MUO and EG3-OMe groups. The apparently enhanced binding at the edges of the 25% and 100% regions is of unclear origin. The most likely explanation is that there was some diffusion of the SMA-17 into the regions adjacent from the channels at the junction of the channel with the solution and gold surface. The resulting high signal is then probably a result of MAb binding to areas in which there was a lower density of SMA-17 than in the regions defined by the channel geometry. The binding of the MAb to these monolayers is further explored in Figure 4.03.

In order to determine the binding tenacity of the MAb to the array, several dilutions of the antibody were run through the instrument in sequence. The binding data was fit using the four-parameter logistic model, which has the following form for a typical x-y coordinate system:²⁸

$$\Delta\%R = \Delta\%R_{\min} + \frac{\Delta\%R_{\max} - \Delta\%R_{\min}}{1 + \left(\frac{[A]}{K_d}\right)^b} \quad (4.1)$$

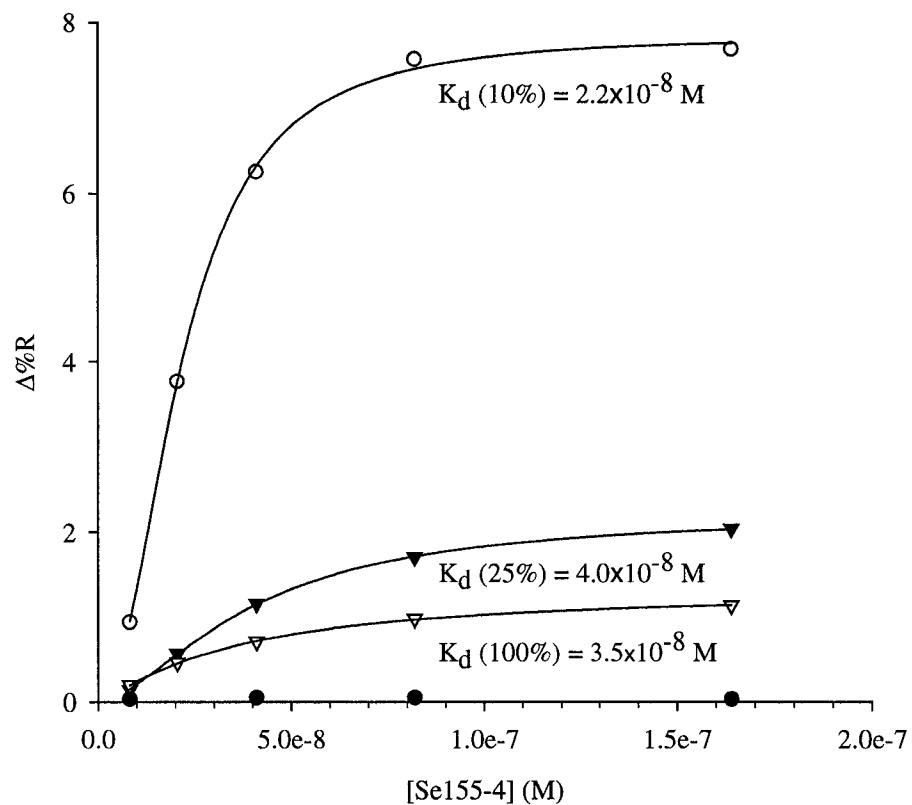


Figure 4.03. Binding data from SPR images of Se155-4 MAb on mixed monolayers of SMA-17 and MUO. Proportions of SMA-17 in the SAMs were 10% (open circles), 25% (filled triangles), 100% (open triangles), and 0% (filled circles). Curvilinear fits are based on equation 4.1.

where $\Delta\%R_{\max}$ and $\Delta\%R_{\min}$ are asymptotic values determined from the regression analysis, $[A]$ is the adsorbate solution concentration, and K_d is the desorption constant. The parameters $\Delta\%R_{\max}$, $\Delta\%R_{\min}$, K_d , and b were obtained from regression fits of the data. The K_d value obtained from the fits reflects the antibody concentration at half-saturation and was used as an estimate of the dissociation constant for the system. When the data is plotted on a log scale in $[A]$, the parameter b reflects the slope of the curve at the inflection point. When $b=1$, the equation reduces to the Langmuir isotherm. Although proposed interpretations for deviations from $b=1$ are that $b<1$ indicates inhomogeneity in binding affinities or negative cooperativity while $b>1$ indicates a positive cooperativity effect,²⁸ any real physical bases for the observed values are somewhat speculative.²⁹ The iterative least-squares solution of this equation, also known as the Hill or Sips plot, is widely used to analyze binding curves in the life sciences.³⁰

Figure 4.03 shows data from the binding of various concentrations of Se155-4 to the array shown in Fig. 4.02. As seen in Fig. 4.03, the saturation binding level was much greater on the 10% SMA-17 monolayer than on those with higher concentrations. In general, dissociation constants for this system tend to fall in the same order of magnitude over different arrays. Table 4.1 lists the fit parameters for the curves in Fig. 4.03. The fitted value of the parameter b from equation 4.1 increases with the decreasing surface density as follows $b_{100\%}=1.2$, $b_{25\%}=1.6$, $b_{10\%}=2.2$. Whether there is any increase in any physical property such as cooperativity is, again, speculative. It can be inferred from the previous explanation of the steric hindrance that at lower epitope densities, steric hindrance is minimized and, thus, can allow for bivalent binding by the antibodies. The value of b at 5% was found to be lower than that at 10%, suggesting that the density of

% SMA-17	$K_d (M^{-1})$	$\Delta\%R_{min}$	$\Delta\%R_{max}$	b	R^2
10	$2.2(0.2) \times 10^{-8}$	0.13 (0.46)	7.86 (0.17)	2.2 (0.4)	0.9993
25	$4.0(0.2) \times 10^{-8}$	0.00 (0.05)	2.24 (0.05)	1.6 (0.1)	0.9998
100	$3.5(0.3) \times 10^{-8}$	0.00 (0.09)	1.32 (0.08)	1.2 (0.2)	0.9996

Table 4.1. Curve-fitting parameters for Se155-4 binding curves in Fig. 4.03. Values in parentheses are standard deviations of the indicated values.

epitopes may become too low for bivalent interactions below 10%. In addition, bivalent binding would require two epitopes to be able to maneuver into the correct orientations, an ability that may be hindered at greater densities.

In order to verify the antigenic specificity of the MAb, SPR imaging was used to examine binding to each of the three epitopes arrayed on a single chip. Figure 4.04 outlines the differences in reactivity observed. The initial array image includes each of the three epitopes at 10% as well as an additional 5% SMA-17 line. The spreading of the pattern due to MUO printing via PDMS is the only noteworthy feature of this image, and is shown in the accompanying cross-sectional profile. The exposure of the array to the MAb resulted in a specific binding to only the SMA-17 epitope, as seen in Fig. 4.04(C, D). Figure 4.05 shows the isotherms for the array in Fig. 4.04, and further confirms that the 10% density may be reasonably close to an optimal level for detection. In addition, the MAb binding is shown to be highly specific, demonstrating the applicability of microarray analysis to antibody screening. Fit parameters for the isotherms in Fig. 4.05 are listed in Table 4.2. Another application area of interest was in the determination of toxin inhibition by synthetic multivalent ligands.

3.2. Inhibition of Shiga-like toxin (SLT) by synthetic inhibitors.

The toxins produced by *E. coli* bind to cell surface Gb₃ receptors through multiple interactions with the homopentameric lectin subunit of the toxin. Figure 4.06 and 4.07 show the Starfish (SF-2) and Daisy ligands used to bind the toxin. Each structure was designed in such a way that the terminal carbohydrate fragments would be able to occupy the strong binding sites of the toxin (there are 10 additional weak binding sites) via specific recognition of the P^k trisaccharide (α -D-Galp-(1-4)- β -D-Galp-(1-4)- β -D-Glcp), a

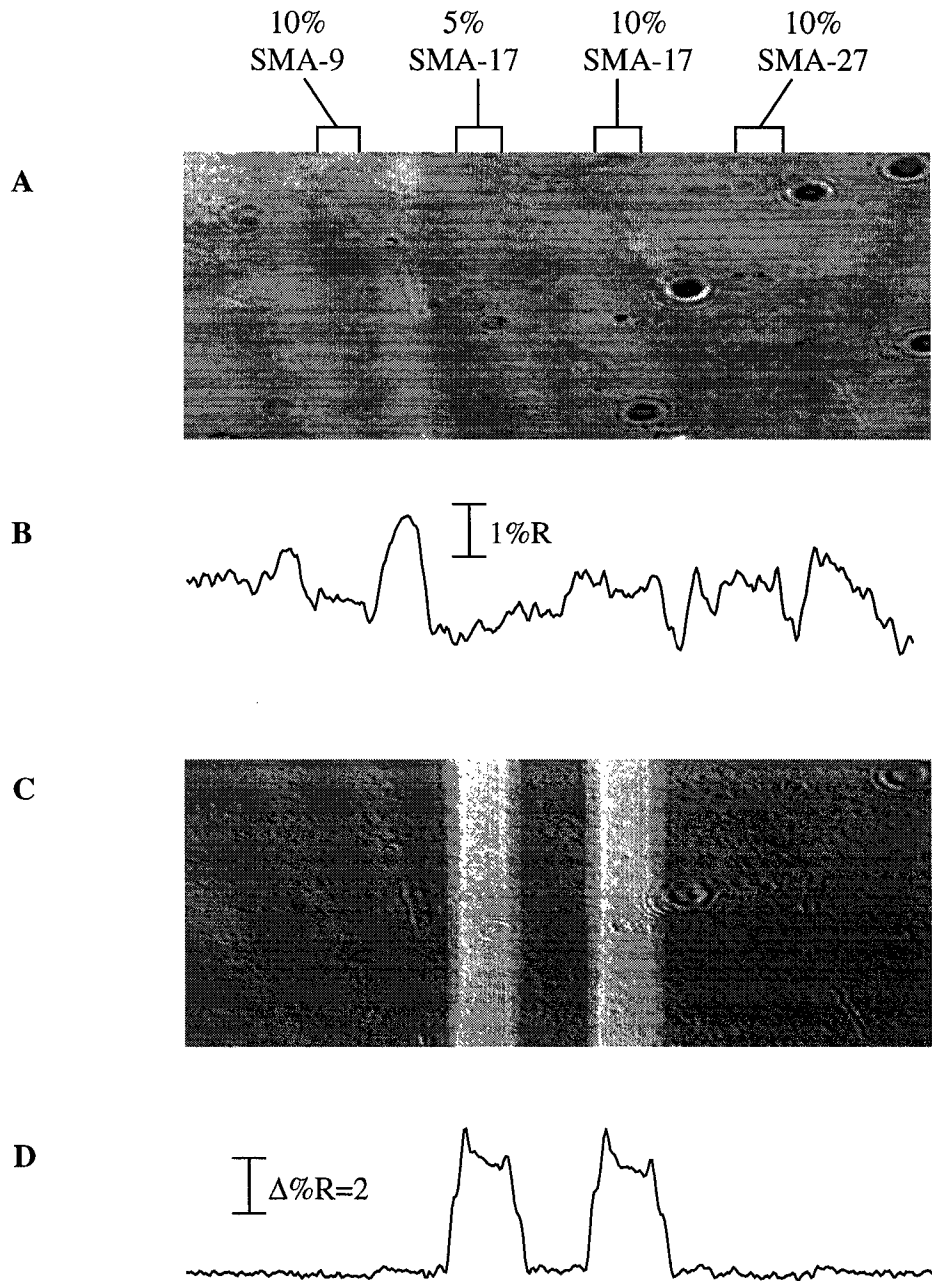


Figure 4.04. (A) Initial SPR image of arrayed epitopes at various surface densities. (B) Cross section showing similar signal intensity for each epitope. (C) Difference image after exposure of array to 3.08 $\mu\text{g}/\text{mL}$ Se155-4 MAb. (D) Cross-section of difference image shows exclusive binding to SMA-17.

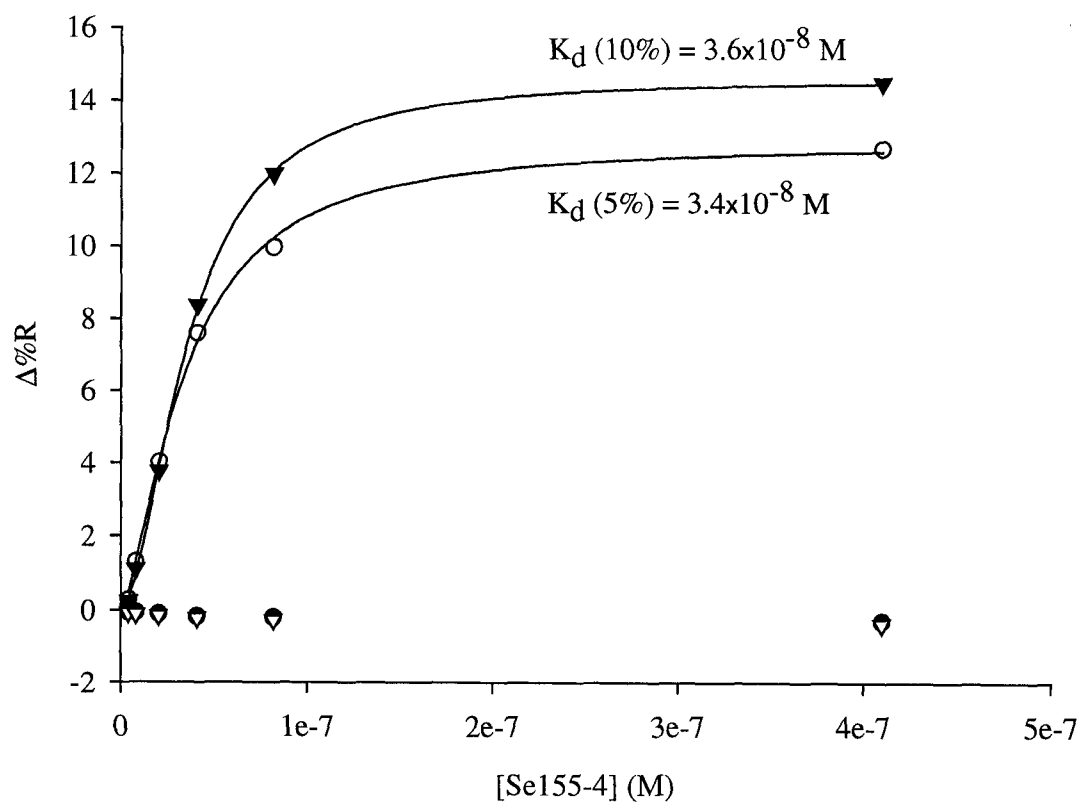


Figure 4.05. Binding of Se155-4 MAb to mixed monolayers of *Salmonella* epitopes and MUO was measured by SPR imaging. Solution proportions of when forming SAMs were 10% SMA-17 (filled triangles), 5% SMA-17 (open circles), 10% SMA-9 (filled circles), and 10% SMA-27 (open triangles). Curvilinear fits are based on equation 4.1.

% SMA-17	K_d (M^{-1})	$\Delta\%R_{min}$	$\Delta\%R_{max}$	b	R^2
5	$3.4(0.3) \times 10^{-8}$	0.0 (0.4)	12.9 (0.4)	1.5 (0.2)	0.9985
10	$3.6(0.1) \times 10^{-8}$	0.1 (0.2)	14.7 (0.2)	1.8 (0.1)	0.9996

Table 4.2. Curve-fitting parameters for Se155-4 binding curves in Fig. 4.05. Values in parentheses are standard deviations of the indicated values.

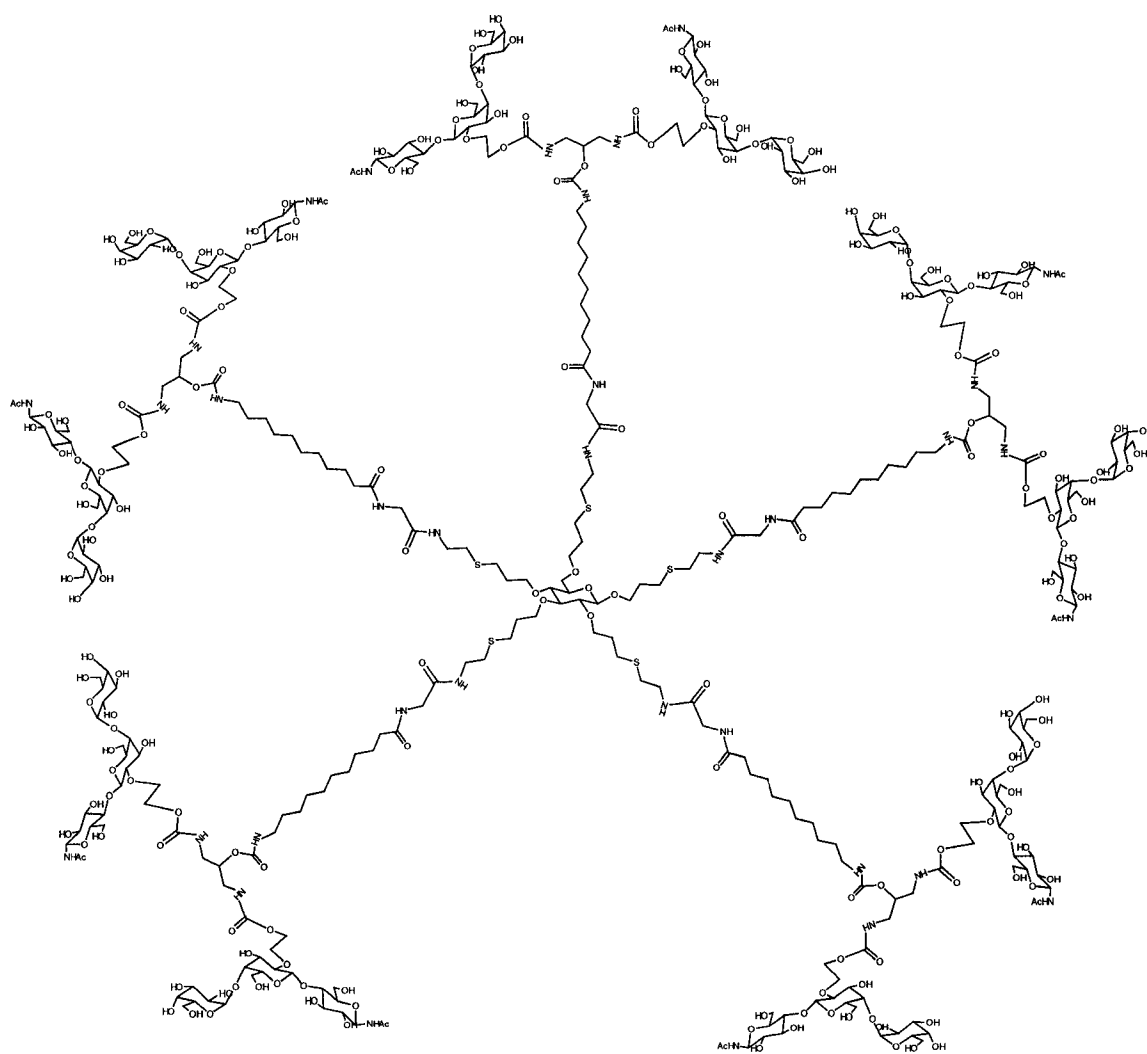


Figure 4.06. Chemical structure of Starfish 2 inhibitor (FW 8703.8847). The P^k trisaccharide unit is presented twice at each end of five radial spacer arms.

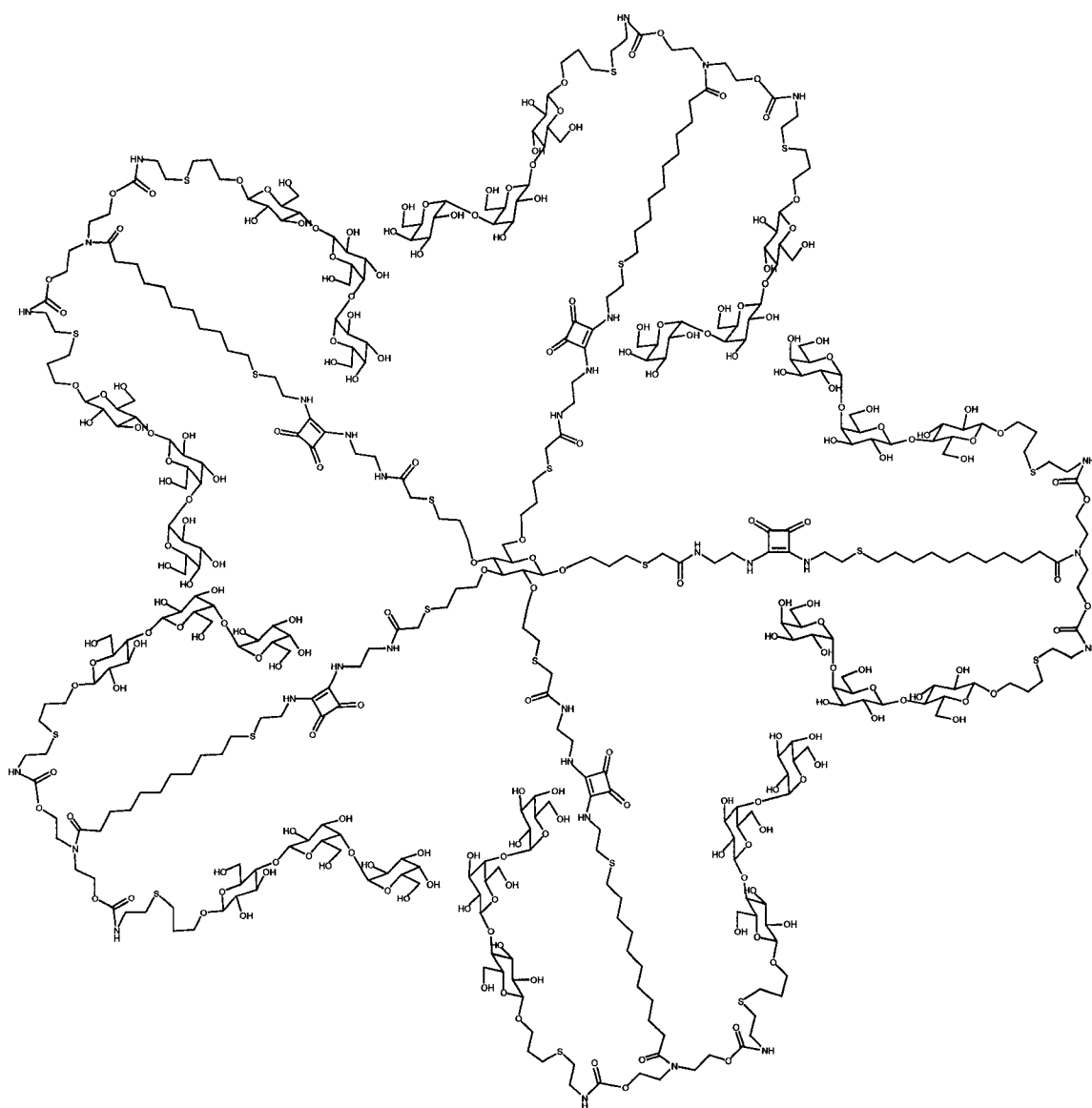
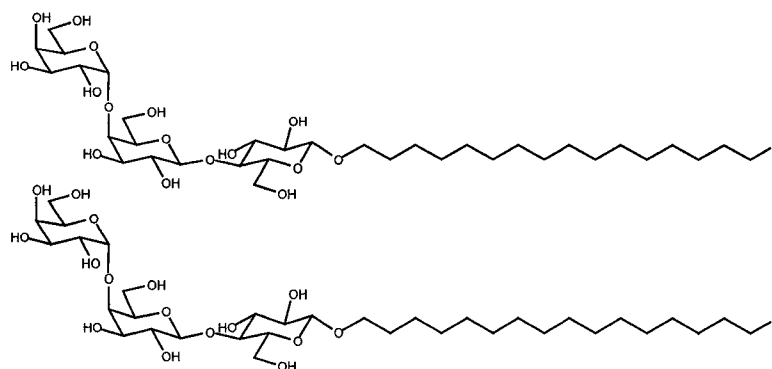


Figure 4.07. Chemical structure of Daisy1 inhibitor (FW 9660.79). The P^k trisaccharide unit is presented twice at each end of five radial spacer arms.

carbohydrate portion of the mammalian Gb₃ receptor. In mammalian cells, the Gb₃ glycolipid is the recognition element responsible for the binding of the Shiga-toxins.³¹ The inhibition of SLT activity by the multivalent Starfish and Daisy ligands has been previously demonstrated by ELISA^{23, 24} and mass spectrometry³¹ as well as by *in vitro*²³ and *in vivo*²⁴ studies. The principal ELISA methods used required separate steps for labeling, blocking, binding interaction and colour development for detection. The inhibition of SLT was studied in order to demonstrate the efficacy and simplicity of microfluidic patterning and SPR imaging as an alternative to ELISA. The arrays for detection of the toxin were produced using mixed monolayers of a disulphide-modified P^k trisaccharide (C₁₆P^k) and an Asialo-GM₂ disaccharide (C₁₆AGM₂) expected to have no interaction with the SLT (Figure 4.08).

The differential binding of SLT by the C₁₆P^k and C₁₆AGM₂ was demonstrated using SPR imaging as shown in Figure 4.09. Fig. 4.09(A, B) describes the array surface initially observed, in which the reflectivity at the P^k addresses was markedly greater than that of the AGM₂. The exposure of the array to 5 µg/mL SLT resulted in an increase in signal on the P^k trisaccharide, with no detectable adsorption on either the AGM₂ or the EG3-OMe background. In this work, it has been a common observation that monolayers presenting oligosaccharide groups at the surface are quite resistant to non-specific protein adsorption. While SAMs presenting mannitol groups at the surface have been shown to be at least as protein-resistant as oligoethylene glycols,³² the observation has not been generalized to the broader class of saccharide-terminated SAMs. The property of protein resistance would come as little surprise given the role of cell surface saccharides in

A



B

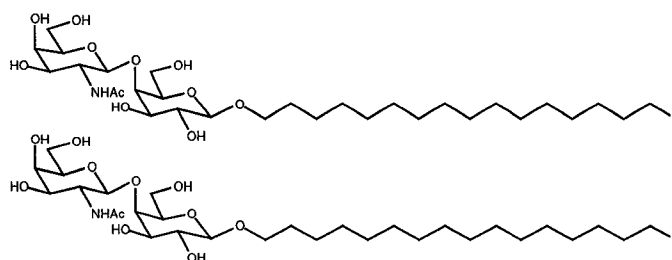


Figure 4.08. Chemical structures of C₁₆ linker-modified (A) P^k trisaccharide and (B) Asialo-GM₂ disaccharide used to produce arrays for studies of SLT inhibition.

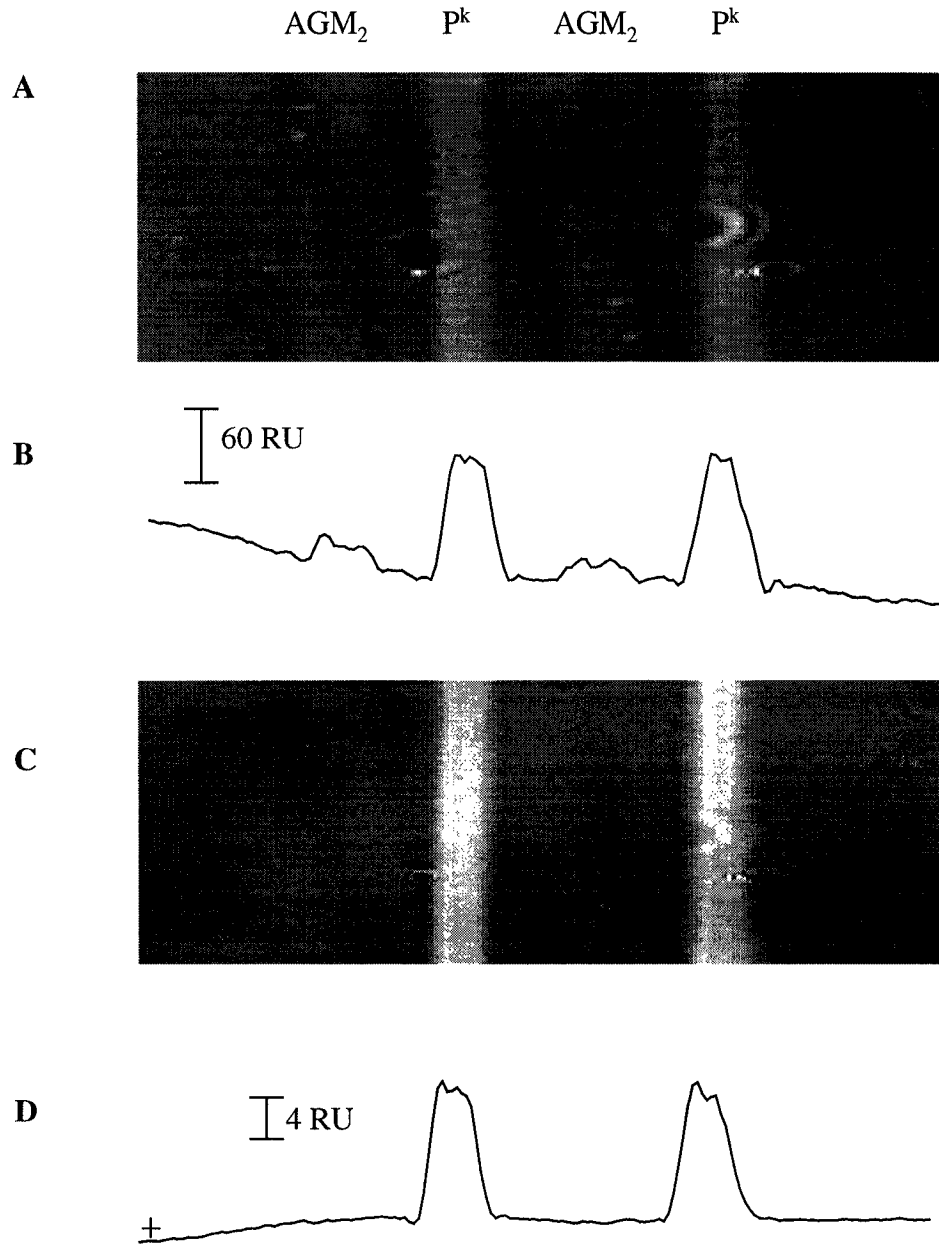


Figure 4.09. (A) SPR image of arrayed AGM₂ and P^k. (B) Cross section showing greater initial signal on the P^k regions than on the AGM₂. (C) Difference image after exposure of array to 5 μg/mL SLT for 10 min. (D) Cross-section of difference image shows exclusive binding to P^k; cross indicates the zero level for the difference image.

specific protein recognition. Given this high protein resistance, the AGM₂ species was used as a diluent for further studies involving the surface-bound P^k trisaccharide.

Given the fixed locations of the binding sites on the SLT B₅ subunit, the effect of ligand density in the monolayer was studied using IRRAS. By tracking the changes in the amide II band intensity upon SLT binding to mixed C₁₆P^k/ C₁₆AGM₂ SAMs, it was possible to determine the optimal C₁₆P^k/ C₁₆AGM₂ concentration ratio. Figure 4.10(A) shows a spectrum before and after adsorption of SLT. The increase in the amide II band is thought to correlate approximately linearly with the amount of protein,^{33, 34} making it a good diagnostic peak for SLT adsorption. Measurements of band intensity were made after subtracting the spectra before and after SLT adsorption, thus ruling out variations in contributions from the C₁₆AGM₂, which itself contains amide groups.

The plot in Fig. 4.10(B) shows the change in amide II intensity with changes in C₁₆P^k density on the surface. The percentages indicated reflect the solution concentrations used to form the SAMs, and not necessarily the actual surface coverage. This plot showed a maximum in binding at around 15% C₁₆P^k, with a slow decrease as the concentration increased. The observed decrease in binding with increasing receptor concentration is not nearly as dramatic as with the *Salmonella* epitopes due to the shallowness of the binding site on the SLT in comparison with the Se155-4 antibody. The fact that most lectins have weak binding interactions is partly a result of the lack of depth in the binding sites. The greater factor in undermining the strength of carbohydrate-protein interactions, however, is the lack of hydrophobic contact area between the carbohydrate and the receptor site. That is, because of the competition for hydrogen bonding sites from the ~56 M water in aqueous systems, the interactions

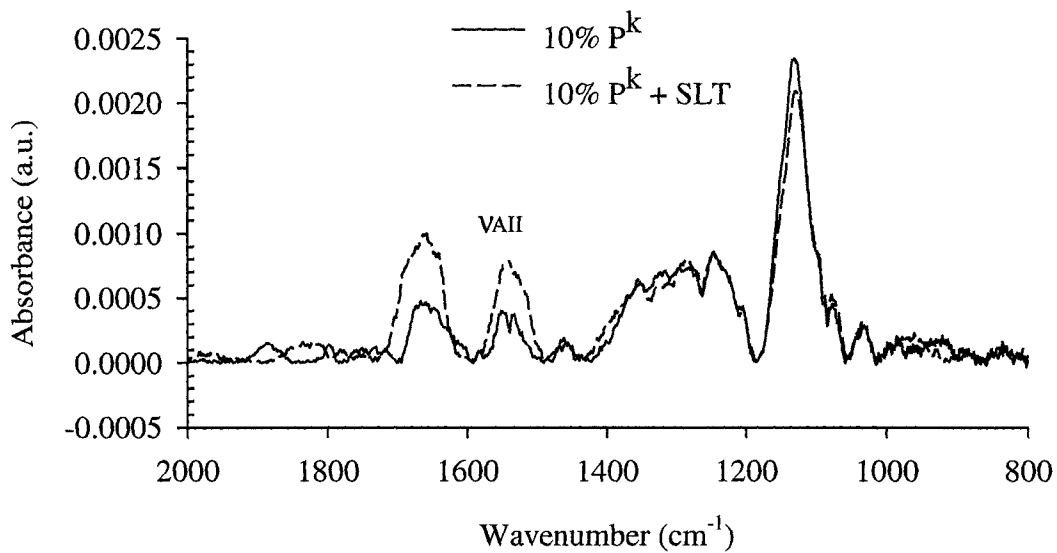
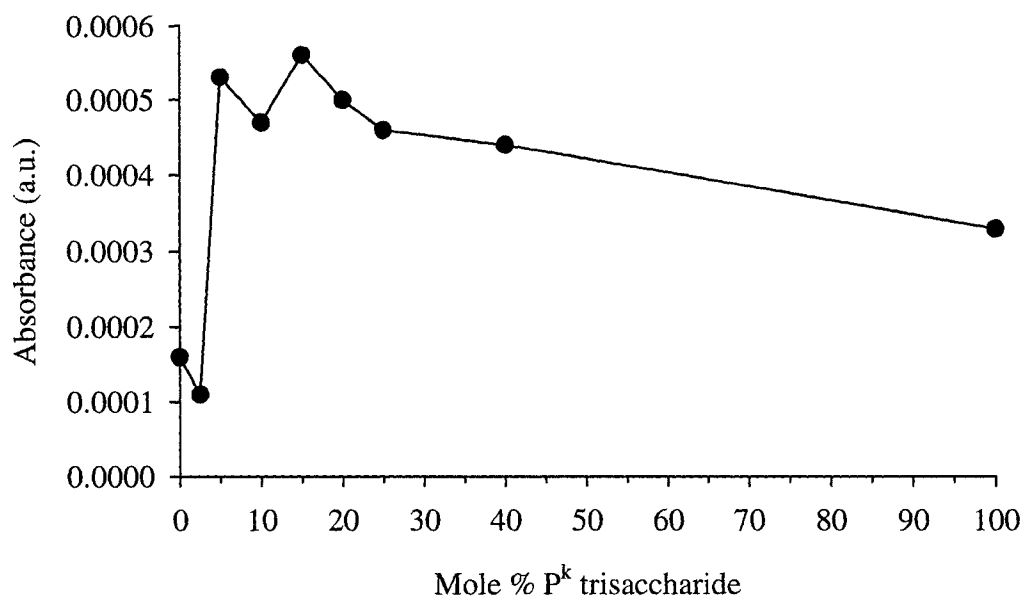
A**B**

Figure 4.10. (A) Examples of IRRAS spectra used to assess SLT binding to SAMs of varying P^k trisaccharide density. (B) Amide II band (V_{Am}) intensity was used to track the amount of bound SLT from a 1 μg/mL solution.

between the carbohydrate and the receptor are unfavourable, necessitating multiple interactions in order to effect strong binding. In addition to the five strong binding sites, SLT also has ten weak binding sites for the P^k trisaccharide, allowing for enhanced interactions even at non-optimal ligand densities.

Having determined an optimal concentration for SLT binding, assays were performed in order to determine values for IC₅₀, the key parameter in inhibition studies. The IC₅₀ value is determined from isotherm fits, and is analogous to the K_d value determined for surface adsorption. By definition, IC₅₀ is the inhibitor concentration at which 50% of the receptor is inhibited. The equation for the curves used to fit the binding data follows equation 4.1, with values of % inhibition replacing values of Δ%R.

Assays were performed by incubating 1.6 μg/mL (42 nM) SLT in PBS with varying inhibitor concentrations overnight, then using SPR imaging on a P^k array to detect the unbound SLT. Inhibition curves for SF-2 and Daisy are shown in Figure 4.11 and Figure 4.12, respectively; the fit parameters are listed in Table 4.3. The measured parameter was the adsorption of the SLT to the array. The resulting values of Δ%R were then fit to equation 4.1 to obtain the maximum and minimum values. The range defined by these extremities was then normalized to 100% by dividing all values by the range and multiplying by 100 (%). The results were then converted to % inhibition values by subtracting all the values from 100%; i.e. the inhibition values plotted reflect the fraction of the maximum signal which was *not* observed as a result of the inhibition. The values were then fit to equation 4.1 once more in order to obtain the parameters listed in Table 4.3.

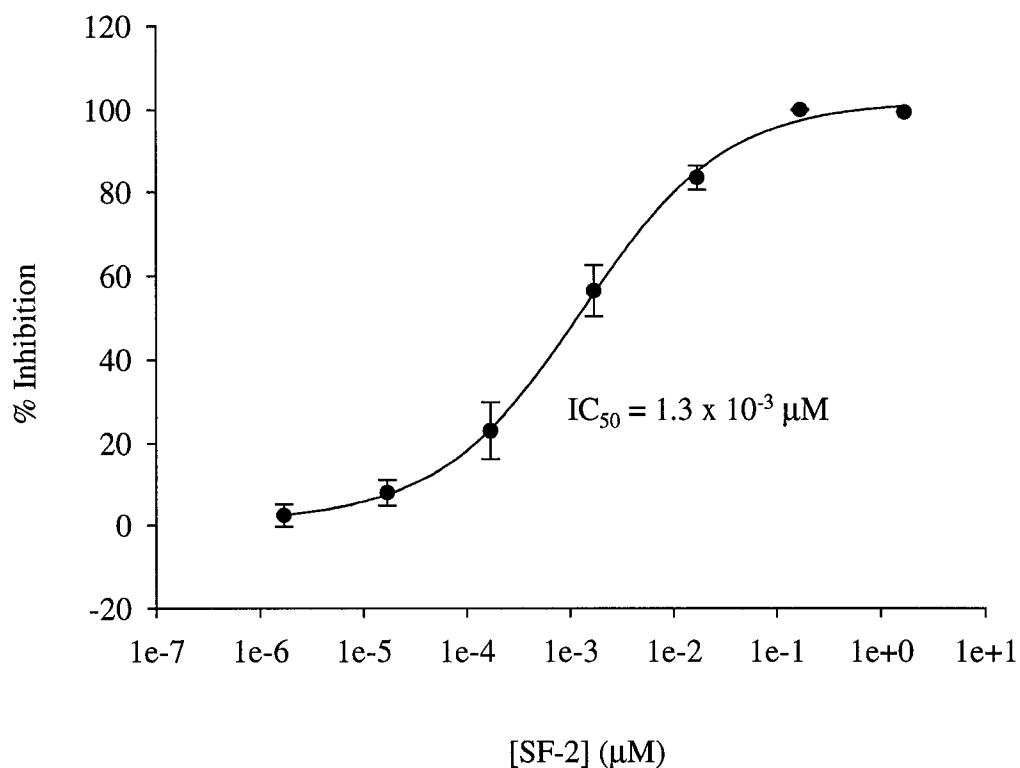


Figure 4.11. Inhibition of 1.6 µg/mL SLT by SF-2 inhibitor. Points are average values measured by SPR imaging on a four-line array; error bars represent standard deviations of the data points. Curvilinear fits are based on equation 4.1. Asymptotic values of % inhibition based on the curve fitting results gave upper and lower limits.

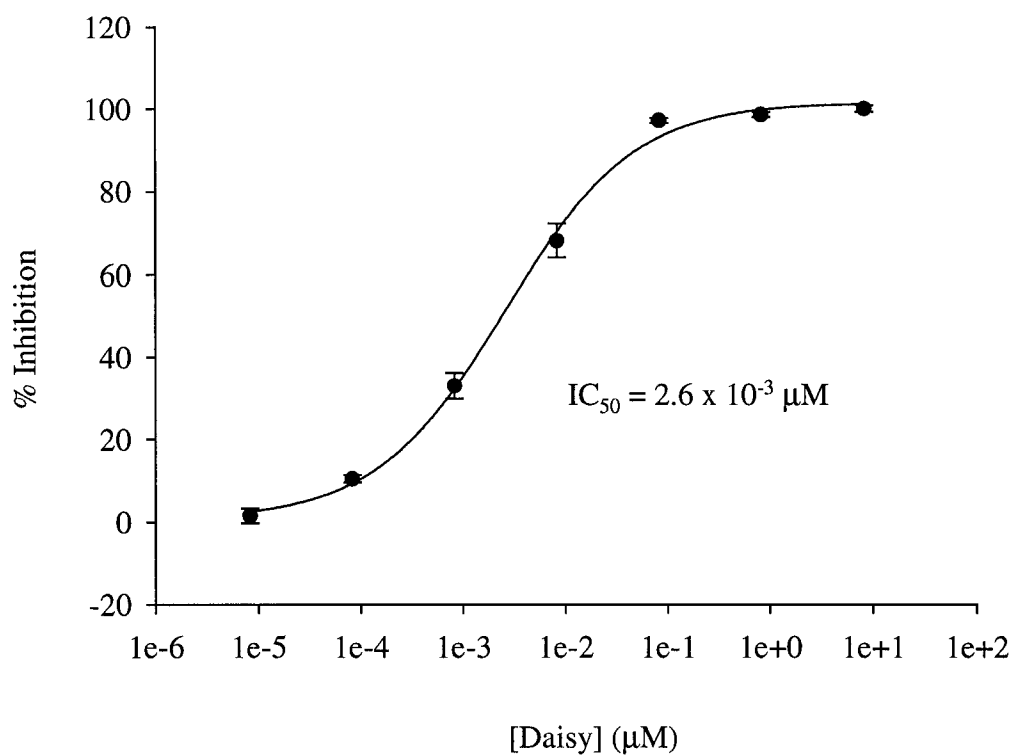


Figure 4.12. Inhibition of 1.6 µg/mL SLT by Daisy inhibitor. Points are average values measured by SPR imaging on a four-line array; error bars represent standard deviations of the data points. Curvilinear fits are based on equation 4.1. Asymptotic values of % inhibition based on the curve fitting results gave upper and lower limits.

inhibitor	IC ₅₀ (nM ⁻¹)	%Inhibition _{min}	%Inhibition _{max}	b	R ²
SF-2	1.3(0.2) x 10 ⁻⁸	0.9 (2.1)	102 (2)	0.62 (0.05)	0.9985
Daisy	2.6(0.3) x 10 ⁻⁸	0.6 (1.6)	102 (1)	0.69 (0.04)	0.9996

Table 4.3. Curve-fitting parameters for SF-2 and Daisy inhibition curves in Figs.s 4.11 and 4.12. Values in parentheses are standard deviations of the indicated values.

The values of the slope parameter b from equation 4.1 were 0.62 for the Daisy inhibition curve and 0.69 for the SF-2 inhibition curve. Although the multivalent nature of the binding between the inhibitors and the SLT may predict a cooperative influence, these values suggest that such an effect may not be dominating the interaction. Given the large number of possible binding sites within each SLT, and the fact that these inhibitors may bind across two SLTs, there may be some heterogeneity in the binding modes in solution.³⁵ The IC_{50} values are in the low nanomolar range for each inhibitor, in agreement with ELISA work performed previously. The value of 2.6 nM for Daisy is slightly less than the reported value of 8.05 nM using ELISA (protocol B, see next paragraph).²⁴ The value of 1.3 nM for SF-2 is slightly larger than the values of 0.24 nM (protocol A) and 0.4 nM (protocol B) for a similar inhibitor.²³ The values reported here tend towards a lower end of the ranges of IC_{50} values determined by various methods in the literature, and likely reflect the differences in the methods used for the determinations. The clear advantages of SPR for this type of assay are operational simplicity and, more importantly, a minimization of the number of interactions necessary to produce a signal.

In previous ELISA studies of SLT inhibition, two separate protocols, termed protocols A and B, were used.²³ In protocol A, SLT was coated on a 96 well ELISA plate, blocked with milk protein (MP) and then exposed to solutions with 10 $\mu\text{g/mL}$ of a biotinylated BSA- P^k trisaccharide conjugate and varying concentrations of inhibitor. Analysis was performed by adding a streptavidin-horseradish peroxidase conjugate and developing with tetramethylbenzidine (TMB)/hydrogen peroxide and phosphoric acid.

The absorbance was then detected at 450 nm. In protocol B, C₁₆P^k was applied to a 96 well ELISA plate before blocking with BSA. SLT with varying inhibitor concentrations was then added. Surface-bound SLT was detected by first adding a rabbit anti-SLT antibody to bind the SLT, then adding HRP-conjugated anti-rabbit IgG antibody. The detection was again performed by developing with TMB/peroxide and reading the absorbance. A schematic comparison of the interactions employed in the ELISA protocols and the SPR imaging protocol used in this work is shown in Figure 4.13. The SPR imaging method is shown to be advantageous in that far fewer reaction steps are necessary in order to perform the assay. As a result, there are fewer steps at which a systematic or random error can be introduced to the assay. In addition to the time savings, by which a 2 day procedure essentially becomes a 1 day procedure, the elimination of many tedious pipetting and washing steps, which require high precision and training, is a major advantage of the SPR imaging methodology presented. The colour development step for detection is a kinetic process that also requires a high degree of precision.

4. Conclusions

SPR imaging of microarrays has been shown to provide a simple and effective means for analyzing protein-carbohydrate interactions. For both systems studied, those of the surface *Salmonella* epitopes and the receptor for SLT, complementary protein binding was maximized by lowering the surface receptor density to a level reflecting 10-

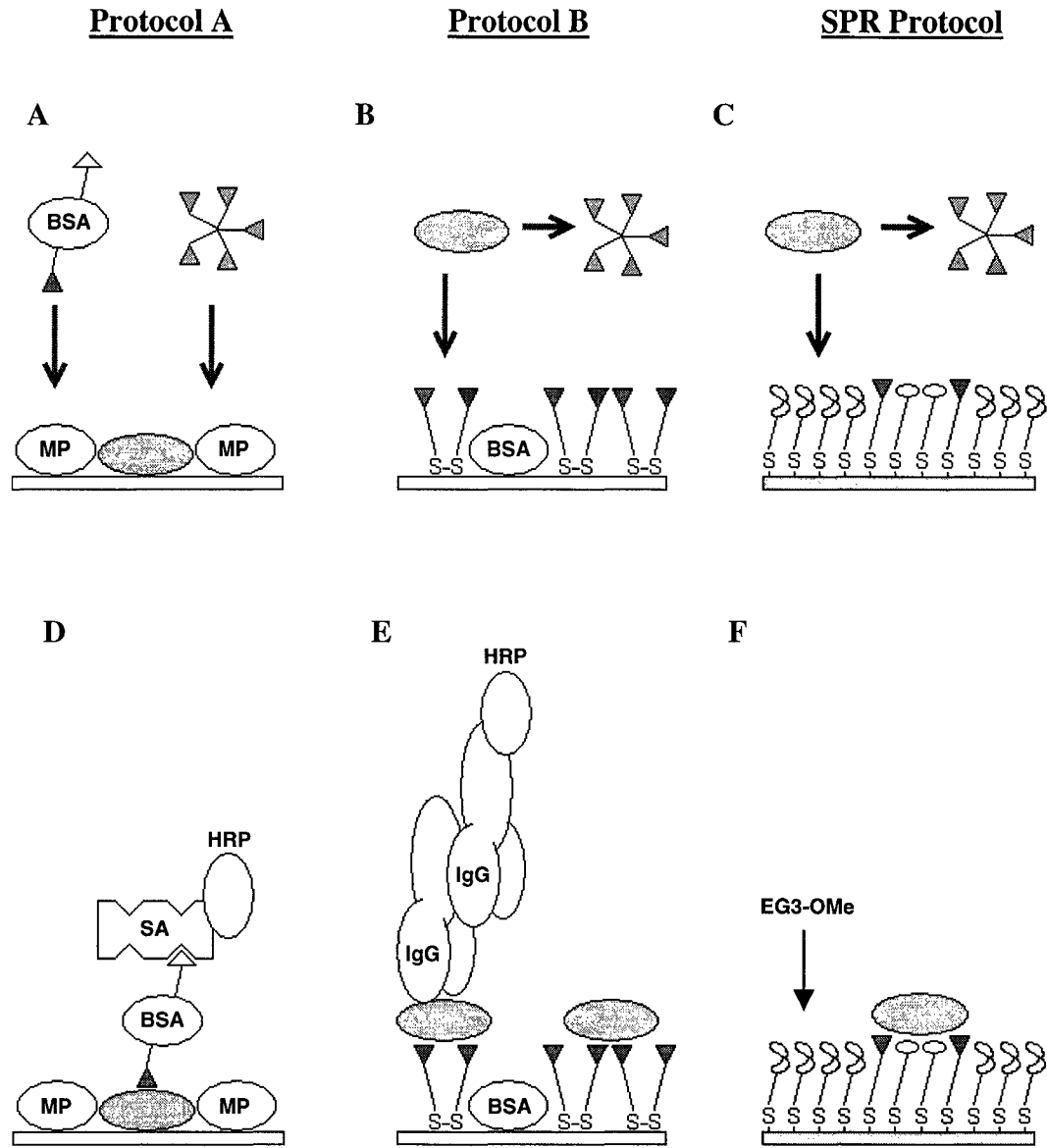


Figure 4.13. Comparison of SPR imaging with ELISA. Green ovoids are SLT, magenta triangles are P^k trisaccharide, orange pentamer is multivalent inhibitor. (A) Competitive assay in which P^k- and biotin-labelled BSA competes with multivalent inhibitor for surface-bound SLT. (B) Competitive inhibition assay in which SLT can bind to either the inhibitor or the surface-bound P^k. (C) Direct inhibition assay adsorbs non-inhibited SLT at mixed P^k/AGM₂ monolayer. (D) Detection by binding of HRP-labelled streptavidin; development with TMB. (E) Detection with anti-SLT, followed by HRP-labelled antibody to anti-SLT; development with TMB. (F) SPR detection.

15% mole fraction in solution. The inhibition assays were shown to be far simpler and reliant upon fewer interactions than typical ELISA protocols.

5. References

- (1) Feizi, T. *Glycoconjugate J.* **2000**, *17*, 553-565.
- (2) Wang, D.; Liu, S.; Trummer, B. J.; Deng, C.; Wang, A. *Nat. Biotechnol.* **2002**, *20*, 275-281.
- (3) Mammen, M.; Choi, S.-K.; Whitesides, G. M. *Angew. Chem. Int. Ed.* **1998**, *37*, 2754-2794.
- (4) Bertozzi, C.; Kiessling, L. L. *Science* **2001**, *291*, 2357-2364.
- (5) Houseman, B. T.; Mrksich, M. In *Host-Guest Chemistry*; Penades, S., Ed.; Springer-Verlag: Berlin, 2002; Vol. 218, pp 1-44.
- (6) Smith, E. A.; Thomas, W. D.; Kiessling, L. L.; Corn, R. M. *J. Am. Chem. Soc.* **2003**, *125*, 6140-6148.
- (7) Fang, Y.; Frutos, A. G.; Lahiri, J. *Langmuir* **2003**, *19*, 1500-1505.
- (8) Houseman, B. T.; Mrksich, M. *Chem. Biol.* **2002**, *9*, 443-454.
- (9) Park, S.; Lee, M.-R.; Pyo, S.-J.; Shin, I. *J. Am. Chem. Soc.* **2004**, *126*, 4812-4819.
- (10) Sharon, N.; Lis, H. *Science* **1989**, *246*, 227-246.
- (11) Lee, Y. C.; Lee, R. T. *Acc. Chem. Res.* **1995**, *28*, 321-327.
- (12) Lee, R. T.; Lee, Y. C. *Glycoconjugate J.* **2000**, *17*, 543-551.
- (13) Horan, N.; Yan, L.; Isobe, H.; Whitesides, G. M.; Kahne, D. *Proc. Natl. Acad. Sci. USA* **1999**, *96*, 11782-11786.

- (14) Duverger, E.; Frison, N.; Roche, A.-C.; Monsigny, M. *Biochimie* **2003**, *85*, 167-179.
- (15) Schengrund, C.-L. *Biochem. Pharmacol.* **2003**, *65*, 699-707.
- (16) Kensinger, R. D.; Yowler, B. C.; Benesi, A. J.; Schengrund, C.-L. *Bioconjugate Chem.* **2004**, *15*, 349-358.
- (17) Gustafson, I. *Colloids Surf. B* **2003**, *30*, 13-24.
- (18) Critchley, P.; Clarkson, G. J. *Org. Biomol. Chem.* **2003**, *1*, 4148-4159.
- (19) Kuziemko, G. M.; Stroh, M.; Stevens, R. C. *Biochemistry* **1996**, *35*, 6375-6384.
- (20) MacKenzie, C. R.; Hiramata, T.; Lee, K. K.; Altman, E.; Young, N. M. *J. Biol. Chem.* **1997**, *272*, 5533-5538.
- (21) Cygler, M.; Rose, D. R.; Bundle, D. R. *Science* **1991**, *253*, 442-445.
- (22) Soltyk, A. M.; MacKenzie, C. R.; Wolski, V. M.; Hiramata, T.; Kitov, P. I.; Bundle, D. R.; Brunton, J. L. *J. Biol. Chem.* **2002**, *277*, 5351-5359.
- (23) Kitov, P. I.; Sadowska, J. M.; Mulvey, G.; Armstrong, G. D.; Ling, H.; Pannu, N. S.; Read, R. J.; Bundle, D. R. *Nature* **2000**, *403*, 669-672.
- (24) Mulvey, G. L.; Marcato, P.; Kitov, P. I.; Sadowska, J.; Bundle, D. R.; Armstrong, G. D. *J. Infect. Dis.* **2003**, *187*, 640-649.
- (25) Aherne, D.; Rao, S. N.; Fitzmaurice, D. *J. Phys. Chem. B* **1999**, *103*, 1821-1825.
- (26) Xia, Y.; Whitesides, G. M. *Angew. Chem. Int. Ed.* **1998**, *37*, 550-575.
- (27) Verma, N.; Reeves, P. *J. Bacteriol.* **1989**, *171*, 5694-5701.
- (28) Rodbard, D.; Hutt, D. M. In *Radioimmunoassay and Related Procedures in Medicine*; IAEA: Vienna, 1974; Vol. 1, pp 165-192.

- (29) Henderson, P. J. F. In *Enzyme Assays: A Practical Approach*; Eisenthal, R., Danson, M. J., Eds.; Oxford University Press: New York, 1993, pp 277-316.
- (30) Nix, B.; Wild, D. In *The Immunoassay Handbook*; Wild, D., Ed.; Nature Publishing: New York, 2001, pp 198-210.
- (31) Kitova, E. N.; Kitov, P. I.; Bundle, D. R.; Klassen, J. S. *Glycobiology* **2001**, *11*, 605-611.
- (32) Luk, Y.-Y.; Kato, M.; Mrksich, M. *Langmuir* **2000**, *16*, 9604-9608.
- (33) Jakobsen, R. J.; Brown, L. L.; Winters, S.; Gendreau, R. M. *J. Biomed. Mater. Res.* **1983**, *16*, 199-201.
- (34) Liedberg, B.; Ivarsson, B.; Lundstrom, I. *J. Biochem. Bioph. Methods* **1984**, *9*, 233-243.
- (35) Kitov, P. I.; Bundle, D. R. *J. Am. Chem. Soc.* **2003**, *125*, 16271-16284.

Chapter V

Surface Chemical Modifications with Microfluidics

1. Introduction

Self-assembled monolayers (SAMs) are a valuable tool for manipulating the surface chemistry of gold. The gold-alkylthiolate monolayers have been widely studied and employed for controlling surface chemistry. The resultant body of knowledge has enabled a variety of researchers to use SAMs in the study of diverse aspects of interfacial chemistry and nanotechnology. Given that the nature of the terminal functional group can dictate the reactivity or influence adsorption, much interest was generated in the patterning of SAMs. Interest in patterning geometrically defined regions of a surface with different thiolates, usually with differing terminal functionalities, has led to the development of a variety of patterning methods.

The typical method for single-component monolayer formation is the exposure of a gold surface to a solution of a given alkylthiol or disulphide, although it is also possible to enact SAM formation via the gas phase.^{1, 2} While this method forms a predictable surface with controllable surface chemistry, it allows only for a homogenous distribution over the exposed gold surface. Several methods for spatially-defined removal of thiolates from gold have been reported in the literature, including UV photolithography,^{3, 4} electron beam etching,⁵ and scraping away regions of a SAM using a sharp tool⁶ or AFM

probe.^{7, 8} Following up the removal of thiolates with the adsorption of a second thiolate-generating species results in the controlled patterning of the surface chemistry.

An alternative to removal of thiolates from a pre-existing monolayer is to select the placement of thiols, for example, by nanoscale writing methods using an atomic force microscopy (AFM) probe.⁸⁻¹⁰ An inexpensive, convenient, and flexible platform for patterned monolayer formation was developed in the laboratories of Prof. G. M. Whitesides. By using relief patterns in polydimethylsiloxane (PDMS) as a contact stamp, and alkylthiols as the ink, the technique of microcontact printing (μ CP) enabled rapid, spatially-controlled monolayer formation.^{11, 12} There are several advantages of this method for generating patterned monolayers. Firstly, μ CP is very operationally simple since no monolayer removal step is necessary. The characteristic self-lamination of PDMS onto macroscopically smooth surfaces, along with the ability to conform to microscopically rough surfaces, allow for high fidelity patterns to be printed over irregular surfaces. The area over which a desired pattern can be printed is dependent only on the stamp design. In addition, the speed of monolayer formation allows for rapid repeatability, especially since the stamps are reusable. The method involves partitioning alkylthiols from solution or neat liquid in to the polymer. During the contact with a gold surface, the alkylthiols can undergo diffusion from the surface and bulk of the PDMS stamp onto the gold surface, with a particular enhancement of transport at the edges of the contacting structures.¹³ One of the limitations of the technique, however, is the difficulty in inking the highly hydrophobic PDMS with alkylthiols containing hydrophilic termini.

The work presented herein demonstrates two strategies for the formation of SAMs with hydrophilic termini. A key motivation for the work was to enable the patterning of hydrophilic SAMs over dimensions compatible with surface plasmon resonance (SPR) imaging. That is, the methods developed were desired to be compatible with preexisting technologies for patterning adsorbates at scales on the order of tens or hundreds of microns. One of these strategies involved enhancing the aqueous solubility of hydrophobic adsorbates using micelles in order to be compatible with surface patterning via PDMS microchannels. Aqueous micelles of the surfactant Tween 20 were used to solubilize carboxylate-terminated alkylthiols ordinarily only sparingly soluble in water.

The other strategy employed was to modify the PDMS microchannels in order to facilitate the microfluidic patterning of alkylthiols from organic solvents or aqueous-organic solvent mixtures. The modification consisted of an oxidation in oxygen plasma followed by silanization with a perfluorinated alkyl chain. A large effort in the modification of PDMS surface chemistry has been driven by the need to control electroosmotic flow and protein/reagent absorption by the polymer in microfluidic analytical systems.¹⁴ The efforts made in this chapter could potentially apply to the confinement of organic liquids in bonded microfluidic systems.

2. Experimental

Octadecanethiol (ODT; Aldrich) was purchased and used after recrystallizing from acetone; 11-mercaptoundecanoic acid (MUA), 11-mercaptoundecanol (MUO), and $\text{HS}(\text{CH}_2)_{11}(\text{OCH}_2\text{CH}_2)_3\text{OCH}_3$ (EG3-OMe) were synthesized in general agreement with

published methods.¹⁵ The synthesis of MUA was detailed in the experimental section of Chapter II, that of EG3-OMe was in Chapter III, that of MUO was in Chapter IV. (Tridecafluoro-1,1,2,2-tetrahydrooctyl)-1-trichlorosilane (TFS) was purchased from United Chemical Technologies and used as received. Poly(oxyethylene)sorbitan monolaurate (Tween 20) was obtained from Fisher and used without further purification. 16-Mercaptohexadecanoic acid (MHA) was obtained from Aldrich and used as received.

Proteins used in this work were obtained in the highest available purity and used as received. Bovine fibrinogen (BFG) and bovine serum albumin (BSA) were obtained from Sigma. Bovine immunoglobulin G (bIgG) was obtained from ICN Biomedicals (Aurora, OH). All protein solutions were prepared in phosphate-buffered saline (PBS: 8.1 mM Na₂HPO₄, 1.5 mM KH₂PO₄, 137 mM NaCl, 2.7 mM KCl in 18MΩ water).

Poly(dimethylsiloxane) (PDMS) microfluidic channels were fabricated according to established methods.¹² Briefly, a relief pattern of photoresist on a silicon wafer was created photolithographically. By curing the prepolymer and cross-linker (Sylgard 184, Dow Corning; Midland, MI) 10:1 by weight against this relief structure, a negative of the relief was formed in the PDMS. The microchannels measured 200 μm wide by 10-15 μm deep. The stamp was also through-bored at the ends of the channels to allow fluids access to the channels when the PDMS device was applied to a surface. Fluid flow was driven by applying vacuum to one access point on the microchannel while connecting the other access point to a reservoir of solution.

Plasma oxidation was performed in a home-built RF plasma generator operating at 27.12 MHz in the laboratory of Prof. J.-B. Green. The plasma was ignited at pressures of 15-40 μm Hg (0.015-0.040 Torr) after evacuating and repressurizing the plasma

chamber several times with oxygen. The plasma was used at a forward power of 75 W, with reflected power generally less than 12 W. Silanization was accomplished by exposing the PDMS to TFS vapour in a dessicator under house vacuum for 1-2.5 h. TFS was used neat and dispersed in paraffin oil, with the latter method providing a slower rate of reaction.

All SPR imaging utilized sensing films consisting of 45 nm gold films deposited on SF10 glass (Schott; Toronto, ON, Canada) with a 1 nm adhesive layer of chromium. Imaging was performed using the GWC Instruments SPRImager (GWC Instruments; Madison, WI). Gold substrates for infrared reflection absorption spectroscopy (IRRAS) were prepared by sputtering 10 nm Ti and 300 nm Au onto clean glass microscope slides. IRRAS spectra were collected on a Mattson Infinity spectrometer with an externally housed low noise MCT-A detector at a resolution of 2 cm^{-1} . Transmission infrared spectra were obtained through the Department of Chemistry spectral services laboratory.

X-ray photoelectron spectra were obtained through the Alberta Centre for Surface Engineering and Science on an Axis 165 XPS spectrometer (Kratos, Chestnut Ridge, NY). The source was monochromated Al $K\alpha$; survey and high-resolution spectra were spectra were collected with a bandpass of 160 eV and 20 eV, respectively.

3. Results and Discussion

The utility of μ CP for the patterning of methyl-terminated SAMs has been well documented.^{11, 12} In contrast, μ CP of alkyl thiols with polar tail-groups using PDMS stamps is relatively rare; a literature search excavated only one example of data showing

μ CP of MUA, but no characterization of the resultant SAMs were presented.¹⁶ Figure 5.01 shows an example of how this barrier may be overcome in the case of a hydroxyl-terminated alkylthiol. By inking the PDMS for an extended period (>1 h) in a relatively high concentration (41 mM) solution of MUO, the stamp was able to absorb enough alkylthiol to print a SAM. As was also seen in Chapter IV, MUO is able to permeate PDMS. In Fig. 5.01(A), the printed regions comprise the “background” while the four vertical lines are SAMs of ODT formed by backfilling the unprinted regions in solution. Adsorption of 100 μ g/mL BFG showed a preferential adsorption to the ODT regions, as expected. The profile in Fig. 5.01(D) shows that the background MUO regions adsorb a significant amount of protein due to the use of the tenaciously surface active fibrinogen¹⁷ for visualization of the pattern. Although this method appeared to be a solution to the problem of patterning ω -functionalized alkylthiols with polar terminal groups, it was not acceptable since some alkylthiolates, such as the glycosides used in Chapter IV, would not be available in large enough quantities to make high-concentration “inks”.

Alternative methods for the direct printing of hydrophilic molecules have made use of surface-modified PDMS stamps. Delamarche *et al* showed that the key to printing high quality patterns of proteins and water soluble catalysts was to modify the surface of PDMS microchannels using a covalently end-grafted poly(ethylene glycol) layer.¹⁸ The modified surface layer maintained a sufficient hydrophilic capacity to allow for the printing of various hydrophilic species, but difficulties in inking resulted in poor printing of hydrophilic thiols and similar molecules.¹⁸

As was demonstrated in Chapter III, it was possible to pattern aqueous MUAM through PDMS microchannels. The water-solubility of MUAM combined with the low

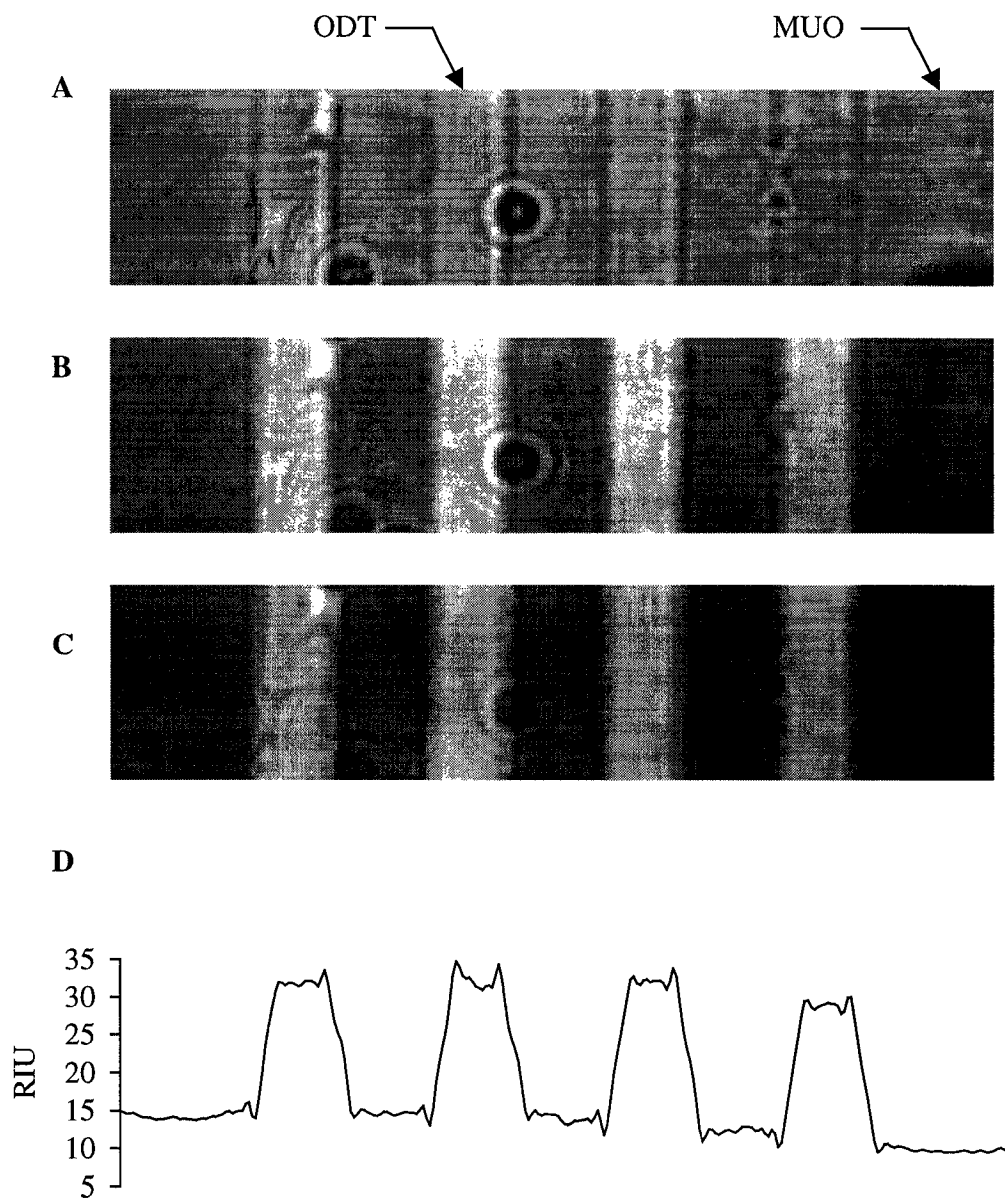


Figure 5.01. SPR images of a microcontact printed MUO SAM (A) before and (B) after adsorption of 100 $\mu\text{g}/\text{mL}$ BFG. The difference image (C) and corresponding image profile (D) indicate the preferential adsorption on the ODT regions.

volumes required by the use of microchannels allowed for the use of very small mass quantities of MUAM in the patterning process.¹⁹ Applying this method to carboxylate-terminal alkylthiols was not possible due to their lower observed solubility in water. Although simply using an aqueous PBS at high pH (11.2 in tribasic sodium phosphate) was discovered to solubilize MUA, the monolayers formed were of poor quality. In order to avoid extremes of pH, which may adversely affect exotic terminal groups with multiple functionalities, another approach was sought. A typical method for enhancing the solubility of organics in aqueous media is the use of micelle-generating surfactants.

It has been shown by others that SAMs deposited from aqueous micelles can be of high quality,²⁰⁻²² possibly even surpassing the alkyl chain densities observed with SAMs deposited from organic solvents.²⁰ For the present study, the surfactant Tween 20 was chosen due to its availability and non-ionic character.

Figure 5.02 shows a series of IRRAS spectra of MUA monolayers formed from 1 mM aqueous solutions in 10 mM Tween 20 (CMC=0.06 mM) for various times. Also included is a spectrum of neat Tween 20 collected in transmission mode for comparative evaluation of any surfactant inclusion in the MUA SAMs. The negative peaks in the IRRAS spectra correspond to the C-D stretches of the deuterated ODT background. As indicated in the C-H stretching region (2800-3000 cm^{-1}) and the C=O stretching region ($\sim 1700 \text{ cm}^{-1}$), largely complete SAMs are formed over the range of adsorption times examined, with no apparent inclusion of Tween 20 within the monolayer structure. The most obvious spectral diagnostic of Tween 20 inclusion was the large C-O-C stretch present at $\sim 1100 \text{ cm}^{-1}$ (that of EG3-OMe typically occurs at 1130 cm^{-1}). The absence of this band in the monolayer spectra indicates that the rinsing procedure used was sufficient

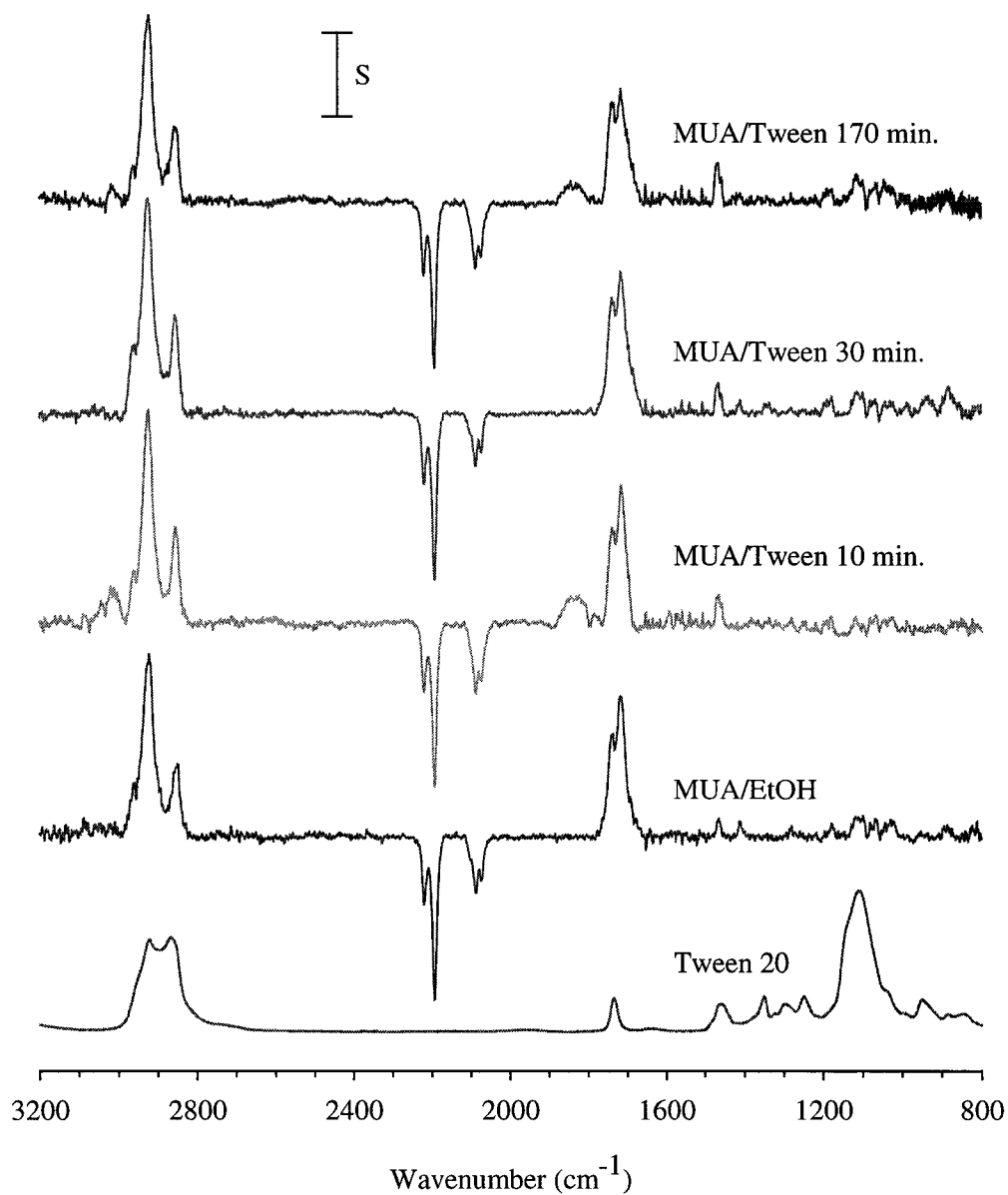


Figure 5.02. IRRAS spectra comparing SAM formation of MUA from 1 mM solutions in ethanol and 10 mM Tween 20 (aq). Bottom spectrum is an absorbance spectrum of neat liquid Tween 20. The scale bar corresponds to $S=0.0004$ a.u. for IRRAS spectra, $S=0.4$ for the Tween 20 spectrum.

to remove any adsorbed or included Tween 20 molecules. The quality of the MUA monolayers was assessed by peak characteristics listed in Table 5.1.

The EtOH-deposited SAM was used as the benchmark for comparison, and showed the most ordered alkyl chain structure. The asymmetric methylene C-H stretch, $\nu_a(\text{CH}_2)$, was observed at 2923 cm^{-1} . The peak position expected for crystalline alkyl chains in all-trans conformation is 2920 cm^{-1} .²³ As can be seen from Table 5.1, the spectra of the films formed from Tween 20 solutions are nearly identical; the peak positions indicate more disordered structures compared with that formed over 170 min. In addition, the increased peak intensities are indicative of a less ordered alkyl chain structure. For the methylene stretching modes, the transition dipole moment of the CH_2 groups is aligned perpendicular to the chain axis in a fully extended all-trans conformation. Given that the tilt angle of the chain in a well-ordered SAM is $20\text{-}30^\circ$ from normal, and that more disordered chains will be able to tilt to higher angles (away from the surface normal), the transition dipole will be aligned more perpendicular to the surface. As a result, the intensity observed would be higher.²³ The same reasoning explains the peak intensities for the symmetric methylene stretch, $\nu_s(\text{CH}_2)$. Thus, although aqueous micellar solutions were shown to be useful for patterning MUA SAMs, the monolayers were shown to be disordered at 10 min. and 30 min. adsorption times. The utility of such solutions in conjunction with PDMS microchannels for patterning of gold was investigated by SPR imaging.

Surfaces were patterned by flowing aqueous micellar solutions of MUA (1 mM in 10 mM Tween 20) through PDMS microchannels on gold for variable times, rinsing with water and ethanol, and back-filling the unmodified gold with EG3-OMe. Figure 5.03

	$\nu_a(\text{CH}_2)$	Abs. (a.u.)	$\nu_s(\text{CH}_2)$	Abs. (a.u.)
Tween/ 10 min.	2925	0.001022	2856	0.000464
Tween/ 30 min.	2926	0.001019	2856	0.000468
Tween/ 170 min.	2923	0.000881	2858	0.000356
EtOH	2923	0.000869	2850	0.000352

Table 5.1. IRRAS peak analyses for MUA SAMs formed from aqueous micellar solutions of Tween 20.

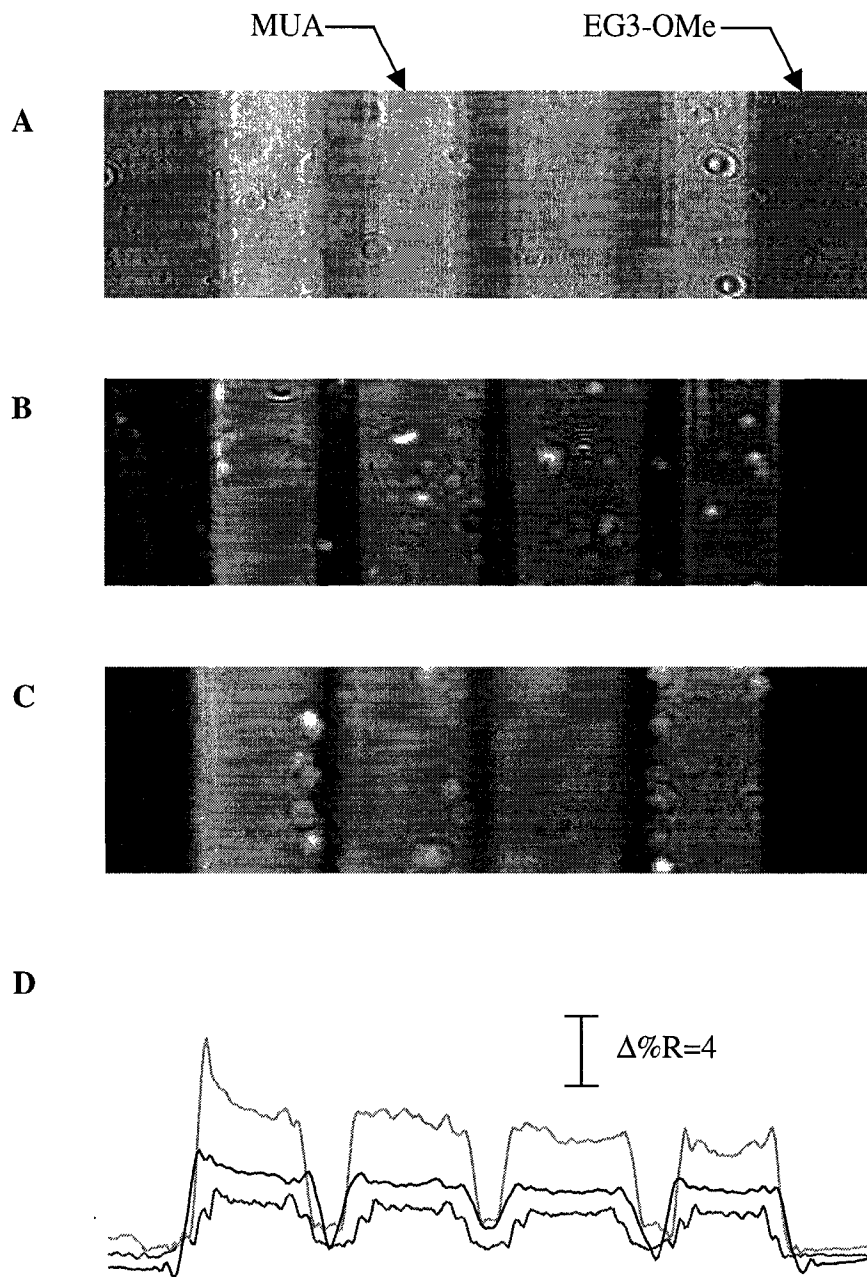


Figure 5.03. SPR difference images after adsorption of 100 μg/mL bIgG to lines formed from 1 mM MUA in 10 mM Tween 20_(aq) for (A) 10 min. (B) 30 min. (C) 170 min. (D) Section profiles for the 10 min. (red), 30 min. (green) and 170 min. (blue) adsorption times.

shows three difference images of patterned SAMs after adsorption of 100 $\mu\text{g}/\text{mL}$ bIgG. The protein was adsorbed in order to provide a contrast for the MUA regions versus the EG3-OMe regions in the difference images. Figure 5.03(A) shows a pattern of MUA lines which had been adsorbed for 10 min. via microchannels. From this image, it can be seen that the patterning appears to have been confined by the channels. In contrast, longer adsorption times within the channels led to broadening of the lines, as seen by the expansion of the MUA line widths in Fig. 5.03(B, C). The decrease in surface tension of the aqueous solution at high concentrations of surfactant may be enough to begin weakening the seal, resulting in spreading of the solution into the region between the PDMS and the gold film. Fig. 5.03(D) shows that the edges of the MUA features are relatively sharp. Also, images viewed over larger areas show local areas of seal failure; if the MUA were diffusing through the bulk PDMS and being printed onto the regions adjacent to the channel, it is likely that the distance diffused would be the similar from all channel walls. Uneven variations in the spreading of the patterns in comparison with the channel dimensions indicated differences in the tenacity of the seal over different parts of the channel device, likely due to variations in mechanical properties. Variations in mechanical properties or topography of PDMS have been observed to occur randomly, most likely due to irregular restoration of the stamp shape after removal of a highly-swelling extraction solvent.

Although the likely cause of the feature broadening is the slow penetration of the PDMS-gold contact regions by the solution, it is interesting to note that, unlike the case with organic solvents such as ethanol, the seal failure is not immediately catastrophic. When ethanol is used, for example, seal failure is easily observable as the entire PDMS-

gold interface is infiltrated with solvent. Thus, while the use of micelle-based self-assembly in microchannels may prove of use in generating chemically patterned surfaces, there appears to be a tradeoff between feature resolution and monolayer quality. Fig. 5.03(D) also indicates that the monolayer formed for 170 min. adsorbs more bIgG than the 10 min film, the adsorption is maximal on the SAM formed for 30 min. Thus, there may be a difference in the nature of the protein adsorption based on the disorder in the SAMs.²⁴ As a result of this difficulty in maintaining a seal in the microfluidic channels, as well as the uncertainty in the quality of the resultant SAMs, a method of microfluidic patterning by which the seal could be maintained for longer time periods was sought.

There has been an increase in interest towards surface-modification of PDMS microchannels in recent years. The majority of applications have been in the areas of controlling electroosmotic flow^{14, 25} and sorption of apolar molecules or proteins within microchannels²⁶ as well as improving the utility of PDMS for printing hydrophilic molecules.^{18, 27, 28} Several methods for the modifications have been demonstrated, but most follow the motif of oxidation of the surface to generate silanol residues followed by silanization of these residues.^{18, 25, 29-31}

By first oxidizing the contacting surface of PDMS in an oxygen plasma and then silanizing the surface with a perfluorinated alkylsilane, a solvophobic surface could be generated.³¹ If this surface were still able to adhere reasonably strongly to a gold surface, then organic solvents could be flowed through the microchannels without breaking the conformal seal. The swelling of PDMS by organic solvents necessitated judicious choosing of the solvent for microfluidic patterning. It was hoped that the silanization of

the surface of PDMS with a perfluorinated alkylsilane would reduce the susceptibility of the bulk polymer to swelling due to uptake of solvent.

Initial attempts to oxidize the surface of PDMS using a RF oxygen plasma revealed that the surface could be made highly wettable by an exposure of just a few seconds. A drop of pure water placed on the freshly oxidized surface quickly spreads to a thin film in order to maximize contact with the newly hydrophilic surface. It is known that oxidation of PDMS $(-\text{Si}(\text{CH}_3)_2-\text{O}-)_n$ by argon,³² hydrogen³² or oxygen plasma,³³ arc/corona discharge,¹⁴ or UV/ozone treatment^{34, 35} creates a silica-like layer (SiO_2) with silanol^{29, 30, 36} and possibly also hydroxyl, carboxyl and peroxide functional groups at the surface.^{33, 37} The mechanisms for this reaction are not completely understood, but are generally thought to involve various high energy plasma species such as electrons, ozone and ions.²⁶ The oxidation of PDMS is thought to proceed by bond cleavage and formation of reactive surface radicals followed by reaction with active plasma species and crosslinking of the polymer chains.^{33, 36} The oxidation of PDMS was explored using x-ray photoelectron spectroscopy (XPS).

Figure 5.04 shows typical XPS survey spectra of native PDMS, plasma-oxidized PDMS (PDMS[ox]), and the oxidized PDMS after modification with TFS (PDMS[ox]-F). Peak areas measured from such spectra were used to determine atomic compositions at the surface of PDMS. Under the conditions of pressure and power used in this work, the surface of PDMS was oxidized within 5 s to a degree so as to enable water to spread into a flat film over the surface. The plasma conditions were chosen in order to facilitate ignition at low power and pressure in an effort to minimize the formation of a glassy silica-like layer (i.e. to preserve flexibility). Figure 5.05 shows high-resolution XPS

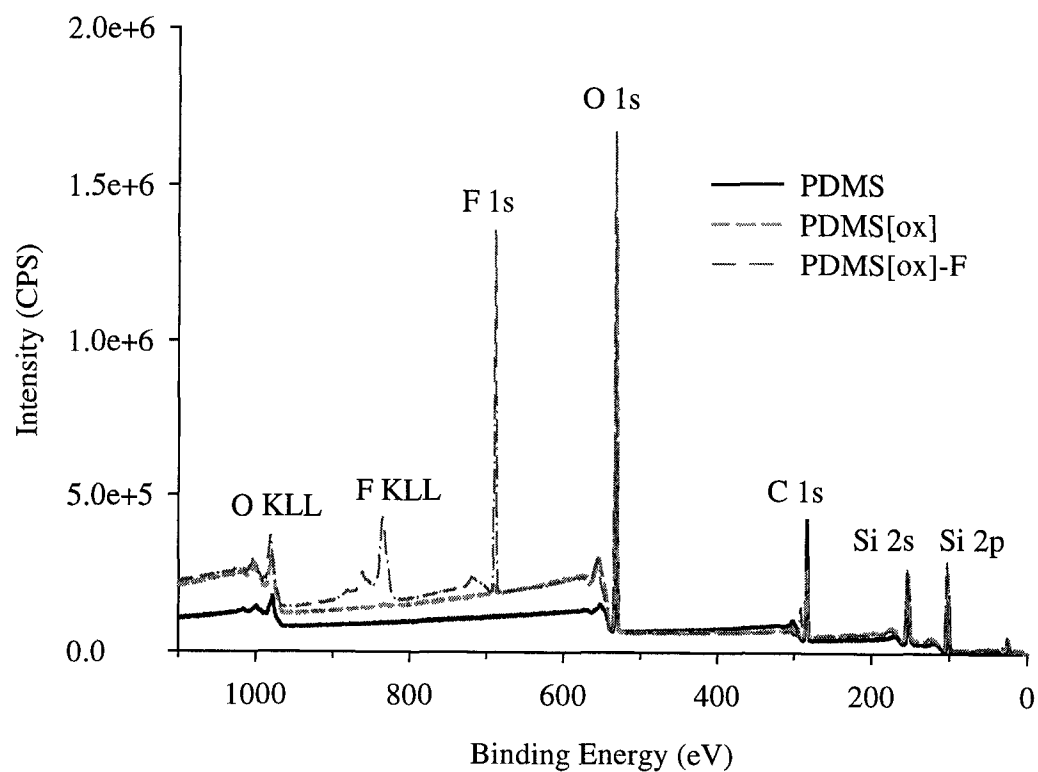


Figure 5.04. XPS survey spectra for native PDMS, a sample oxidized for 30 s, and an oxidized sample modified with TFS.

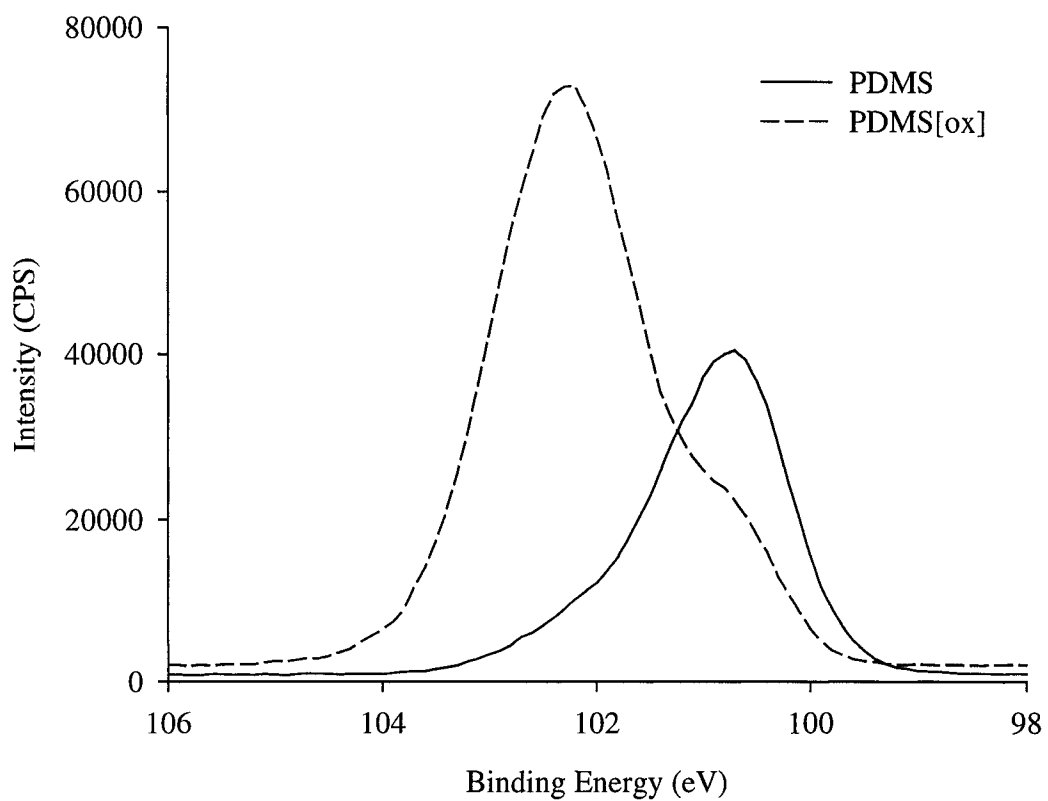


Figure 5.05. High-resolution XPS spectra comparing native PDMS with PDMS oxidized by plasma for 90 s.

spectra for native PDMS and PDMS oxidized for 90 s in plasma. The figure shows that the binding energy of the Si 2p peak was shifted from 100.7 eV to 102.5 eV; the series of high resolution spectra indicated that this shift in energies was complete after 45 s oxidation (i.e. beyond 45 s of oxidation, there was no further shift). Given that the known binding energy of SiO₂ occurs in the range 103.3-103.7,³⁴ the observed shift is indicative of the conversion to a more silica-like structure.

Figure 5.06 shows the changes in composition at oxidation times ranging from 30-120 s. The atomic concentrations were determined by taking into account the relative sensitivity of the instrument for each element and the total composition of the PDMS surface was normalized to 100%. The expected values for Si, O, and C based on the formula (-Si(CH₃)₂-O-)_n are 25%, 25%, and 50%, respectively. Fig. 5.06 uses dashed lines to indicate these levels, and the values measured for unmodified PDMS at zero oxidation time are very close to the expected values. Figure 5.07 graphs the changes in composition after vapour-phase silanization with TFS. The level of compositional change within the surface region reached a limiting value within 45 s, as is shown by Fig. 5.07. The sampling depth in this case was unknown, but would not likely be greater than 10 nm based on the attenuation lengths for Si, O, C, and F.³⁸ Table 5.2 lists the observed changes in composition after various surface treatments.

The results in Table 5.2 indicate that plasma oxidation resulted in a change towards greater oxygen content and reduced carbon content in the PDMS[ox] surface. That the carbon content is not completely eliminated can be attributed to incomplete oxidation of deeper polymer chains. The Si/O ratio undergoes change from 0.8 to 0.5, as expected for the conversion of PDMS to a more silica-like structure. In addition, nearly

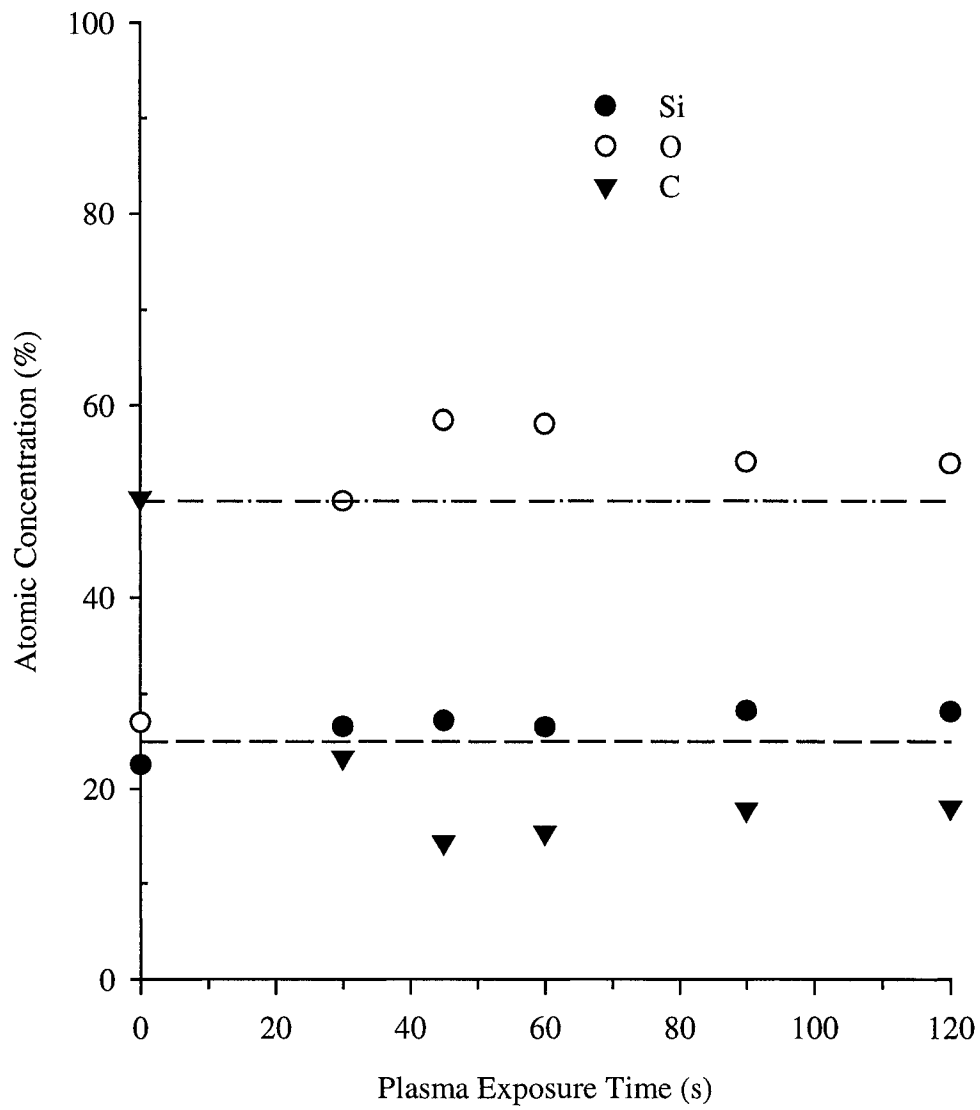


Figure 5.06. XPS was used to determine atomic concentrations of PDMS for various exposure times to the plasma. Dashed lines indicate theoretical composition values of 25% and 50% as a visual guide.

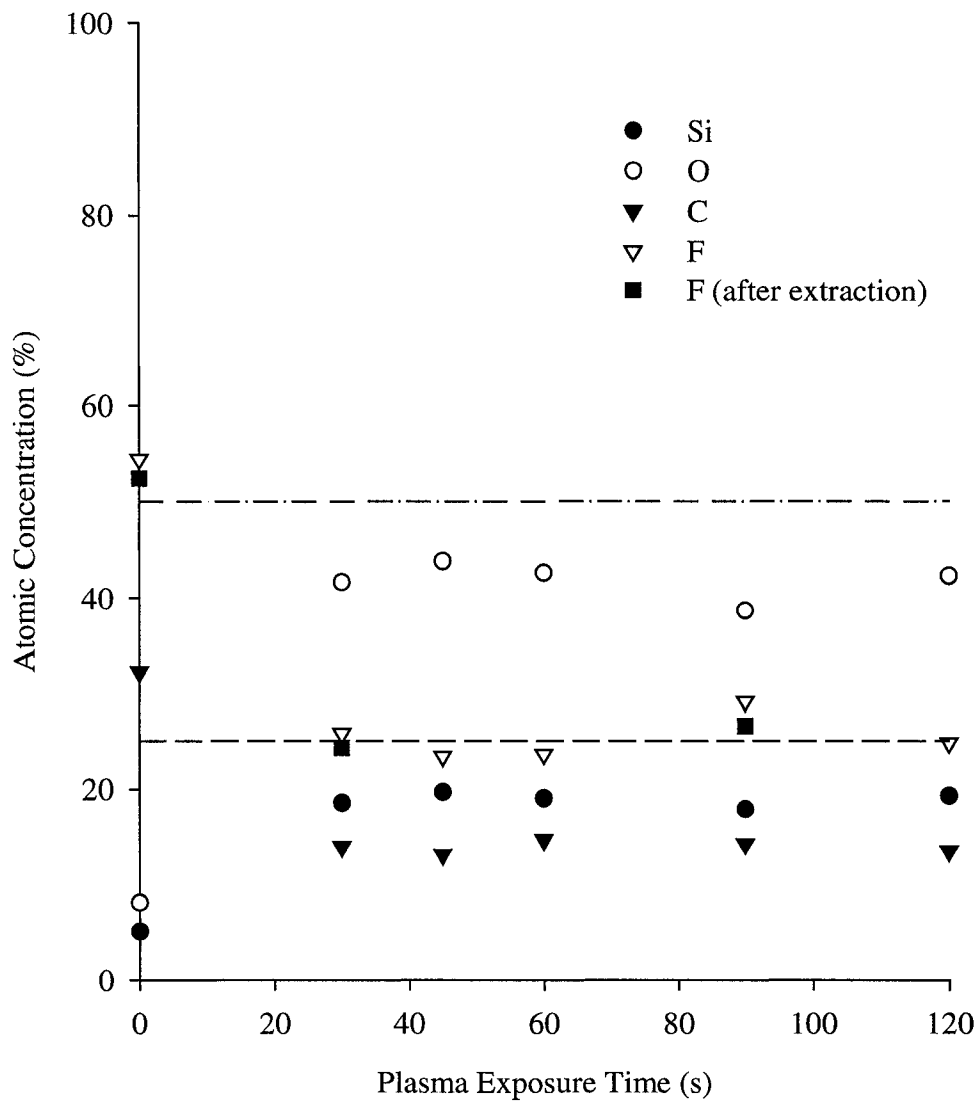


Figure 5.07. XPS determined atomic concentrations of PDMS[ox]-F samples (I.e. PDMS after oxidation and silanization with TFS). Filled squares indicate fluorine concentrations measured after solvent extraction. Dashed lines indicate theoretical composition values of 25% and 50% as a visual guide.

	Si	O	C	F
PDMS (theoretical)	25	25	50	
PDMS (measured)	22.59	27.07	50.33	
PDMS[ox]	27.34 (0.79)	54.90 (3.46)	17.76 (3.50)	
PDMS[ox] (ex)	26.99 (1.03)	48.95 (6.09)	23.75 (7.14)	
PDMS-F	5.19	8.17	32.23	54.42
PDMS-F (ex)	5.40	8.96	33.21	52.43
PDMS[ox]-F	18.90 (0.69)	41.84 (1.93)	13.91 (0.61)	25.34 (2.34)
PDMS[ox]-F (ex)	18.78 (0.01)	40.96 (1.75)	14.85 (0.13)	25.44 (1.62)

Table 5.2. Percent composition of PDMS with plasma treatment and silanization as measured by XPS. The (ex) suffix refers to values measured after solvent extraction of the samples. Numerical values in parentheses indicate standard deviations of the indicated values, which are averages over all oxidation times.

all samples, other than those maintained in UHV conditions, contain adventitiously adsorbed carbon. In fact, the C 1s peak position due to this carbon is a common basis for calibration of XPS binding energies.³⁹ Solvent extraction with hexanes was performed on samples oxidized for 0, 30, and 90 s in order to assess the presence of non-covalently sorbed material. Swelling and extraction of low molecular weight fragments from PDMS using hexane followed by sonication in ethanol/water mixtures had previously been demonstrated to prevent the fouling of contacted surfaces by PDMS microdevices.⁴⁰ Extraction of PDMS[ox] resulted in an increase in the relative carbon concentration, possibly due to the removal of cleavage products from the original plasma treatment. While the carbon may have been removed as volatiles it is also possible that some silicon-oxygen bonds were cleaved, resulting in smaller fragments that could be removed by solvent extraction.

An interesting feature of native PDMS treated with TFS is that this surface (PDMS-F) contained a far greater amount of fluorine than silicon or oxygen. This was not the case when oxidized PDMS was silanized (PDMS[ox]-F). It is clear that the TFS was able to partition into at least the surface region of native PDMS. The fact that this anomaly is observed only for unmodified PDMS suggests that the silica-like layer formed by oxidation acts as a barrier to TFS sorption and/or that the initial reaction of TFS with surface silanol groups creates a barrier against further sorption. It is possible, however, that this effect may also have been present to a lesser degree for the oxidized samples. Extraction in hexanes caused little change in the atomic concentrations for either the native or oxidized PDMS treated with TFS. The swelling of PDMS by hexanes normally causes a warping of the material in addition to its increase in size. For the PDMS[ox]-F

samples, exposure to hexanes was seen to cause the samples to curl as the treated surface resisted the solvent while the other side swelled. The dimensions of PDMS upon exposure to hexane have been reported to increase by a factor of 1.35.⁴¹ Over a period of minutes, the entire structure is swelled. Although it seems likely that the presence of the perfluorinated groups afforded resistance against swelling, it may also be possible that the curling was a result of the greater cross-linking of the silica layer formed by oxidation.

Despite the apparent similarity in the effects of plasma treatment on the surface structure of the PDMS, several differences were observed in the material as a result of increased plasma exposure times. The samples treated for a longer time likely were altered to greater depths as a result of the plasma treatment. This was apparent from the increase in the formation of a light-refracting surface “halo” which appeared to initiate at the edges of the flat samples and structured channels. The refractive index of PDMS is 1.405, while that of silica is 1.457.³⁴ In addition, all fluorinated stamps needed to be pressed into contact at many points on the device in order to form a seal against the substrate.

Figure 5.08(A) shows an array formed using microchannels modified with a 90 s plasma exposure followed by silanization with TFS. An ethanolic 1 mM ODT solution was passed through the channels for 5 and 15 min. Previous experience with unmodified PDMS had shown a tendency towards leakage due to seal failure and adsorbate diffusion through the PDMS when patterning from ethanolic solutions. There is an apparent fouling of the background region, which had been backfilled with EG3-OMe after ODT patterning. After exposure of the array to 1% BSA for 10 min., however, a very even

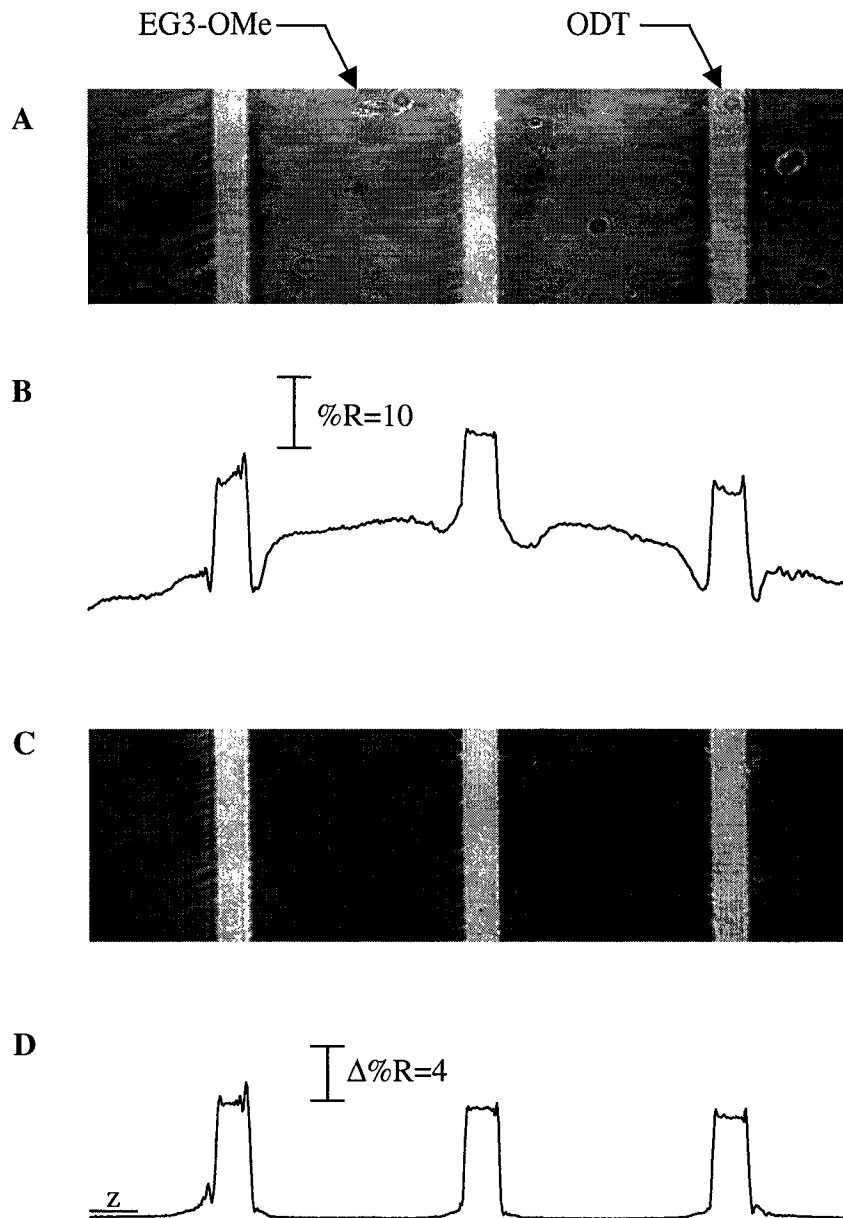


Figure 5.08. SPR image (A) and corresponding profile (B) of a line array formed by patterning ODT from ethanolic solution through PDMS[ox]-F microchannels, backfilled with EG3-OMe. The two outer lines were patterned for 5 min.; the middle line for 15 min. Difference image (C) and corresponding profile (D) after adsorption of 1% BSA. The horizontal line indicated by the letter z shows the zero difference level. Average signal on the EG3-OMe regions is -0.5 .

change of signals was observed in both the ODT and EG3-OMe regions (Fig. 5.08(C)). Fig. 5.08 (C) shows some apparent streaks emanating from the ODT lines. It is likely that these were caused by cracks in the PDMS induced by the plasma. It has been shown that oxidation of PDMS can decrease the thickness of a PDMS film and induce cracks in the shrinking, brittle silica-like surface layer.^{34, 36} In addition, the cracks may have been further enhanced by the greater compressive force applied to the stamp in order to form a seal with the gold surface. The fact that the apparent fouling did not diminish the protein resistant character of the background region suggests that although there may have a variable level of surface contamination, EG3-OMe adsorbed at a sufficient density to bar adsorption over the entire background region.

The fouling of the surface by PDMS[ox]-F microchannel devices was investigated qualitatively by stamping the microchannel device against glass. It was found that the contact between the device and the glass left behind a residue that rendered the contacted areas hydrophobic. The residue was persistent against rinsing with water or ethanol, and repeated stamping with the same device left hydrophobic residue over at least three consecutive attempts. In order to remove the residue, which may have been caused by unreacted TFS, short PDMS oligomers, and/or plasma oxidation products, the devices were cleaned exhaustively by extracting with hexanes overnight, sonication in ethanol/water mixtures twice for 5-10 min., soaking overnight in 1% SDS, rinsing with water and ethanol, and further sonication three times in ethanol/water mixtures (roughly 1:1) for 10 min. The resulting stamps still printed a small amount of residue on glass, but the residue was less tenacious than before and was mostly removed by rinsing with water.

Figure 5.09(A) shows a pattern made by flowing ethanolic 1 mM MHA through a cleaned PDMS[ox]-F microchannel device for 10 min. The initial surface appeared to deposit less residue than in Fig. 5.08. A negative tradeoff, however, was that the extensive cleaning procedure, which included swelling in hexane, may alter the integrity of the surface chemical modifications. Fig. 5.09(D) shows the section profile of the difference image after adsorption of 100 $\mu\text{g}/\text{mL}$ BSA. It is apparent from the curved edges of the MHA regions that some of the MHA had been transferred to the surface beyond the geometric constraints of the channel. The mechanism of this transfer is unknown, but the shapes of the profiles indicate that diffusion through the polymer was a possibility.

The examples shown in Figs. 5.08 and 5.09 notwithstanding, the sealing of the PDMS[ox]-F microchannels was unreliable, with unpredictable failures as a result of catastrophic seal failures. As a result of the greater seal integrity of native PDMS, it was decided that solvent systems compatible with both the patterning species and PDMS would have to be chosen on a case-by-case basis. The patterning schemes for the glycosides in Chapter IV were a direct result of this conclusion. It was found that mixtures of methanol and water could be used for solubilization of the amphiphilic molecules used therein without failure of the PDMS seal for times up to 30 min. Longer times were not investigated.

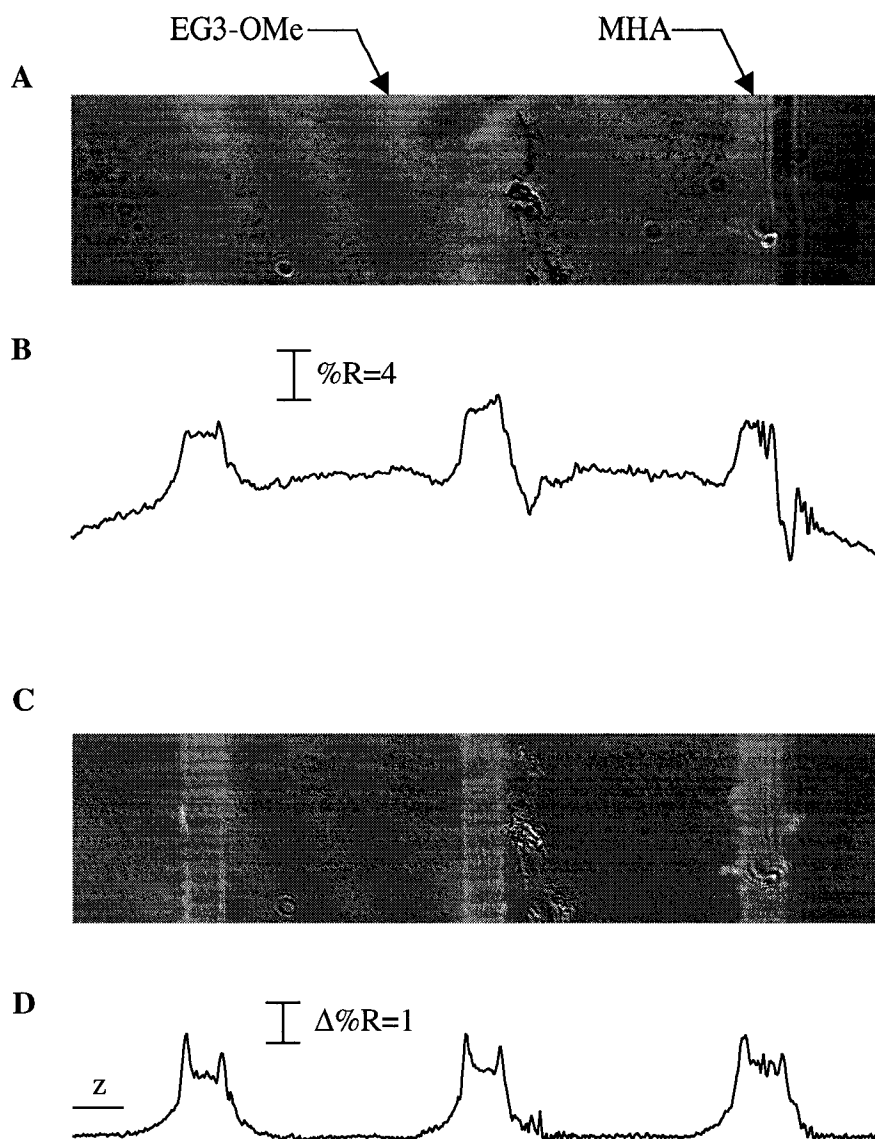


Figure 5.09. SPR image (A) and corresponding profile (B) of a line array formed by patterning MHA from ethanolic solution through PDMS[ox]-F microchannels, backfilled with EG3-OMe. Difference image (C) and corresponding profile (D) after adsorption of 0.01% BSA. The horizontal line marked by the letter z in the line profile indicates the zero difference level; average signal on the EG3-OMe regions is -0.7 .

4. Conclusions

Aqueous micellar solutions of Tween 20 were shown to be able to solubilize MUA for the purpose of generating SAMs. The SAMs formed were found to require long adsorption times in order to form SAMs of reasonable quality. The solutions were not well confined by microchannels in PDMS for periods over 10 min. Plasma modification schemes were enacted in order to allow for functionalization of the PDMS surface. XPS spectroscopy showed that the surface of PDMS was easily modified by oxygen plasma and subsequent silanization. The resulting modified channels were found to require extensive cleaning in order to remove undesirable contaminants. The perfluorinated alkyl chains grafted onto the PDMS resulted in poor sealing between the channels and the substrate, leading to the conclusion that the best compromise would be to adjust solvent systems for use with native PDMS.

5. References

- (1) Dubois, L. H.; Zegarski, B. R.; Nuzzo, R. G. *J. Chem. Phys.* **1993**, *98*, 678-688.
- (2) Yan, C.; Golzhauser, A.; Grunze, M. *Langmuir* **1999**, *15*, 2414-2419.
- (3) Huang, J.; Dahlgren, D. A.; Hemminger, J. C. *Langmuir* **1994**, *10*, 626-628.
- (4) Tarlov, M.; Burgess, J., D. R. F.; Gillen, G. *J. Am. Chem. Soc.* **1993**, *115*, 5305-5306.

- (5) Lercel, M. J.; Redinbo, G. F.; Pardo, F. D.; Rooks, M.; Tiberio, R. C.; Simpson, P.; Parikh, A. N.; Allara, D. L. *J. Vac. Sci. Technol. B* **1994**, *12*, 3663-3667.
- (6) Abbott, N. J.; Folkers, J. P.; Whitesides, G. M. *Science* **1992**, *257*, 1380-1382.
- (7) Amro, N. A.; Xu, S.; Liu, G.-Y. *Langmuir* **2000**, *16*, 3006-3009.
- (8) Xu, S.; Miller, S.; Laibinis, P. E.; Liu, G.-Y. *Langmuir* **1999**, *15*, 7244-7251.
- (9) Piner, R. D.; Zhu, J.; Xu, F.; Hong, S.; Mirkin, C. A. *Science* **1999**, *283*, 661-663.
- (10) Hong, S.; Zhu, J.; Mirkin, C. A. *Science* **1999**, *286*, 523-525.
- (11) Kumar, A.; Whitesides, G. M. *Appl. Phys. Lett.* **1993**, *63*, 2002-2004.
- (12) Xia, Y.; Whitesides, G. M. *Angew. Chem. Int. Ed.* **1998**, *37*, 550-575.
- (13) Delamarche, E.; Schmid, H.; Bietsch, A.; Larsen, N. B.; Rothuisen, H.; Michel, B.; Biebuyck, H. A. *J. Phys. Chem. B* **1998**, *102*, 3324-3334.
- (14) Wang, B.; Chen, L.; Abdulali-Kanji, Z.; Horton, J. H.; Oleschuk, R. D. *Langmuir* **2003**, *19*, 9792-9798.
- (15) Pale-Grosdemange, C.; Simon, E. S.; Prime, K. L.; Whitesides, G. M. *J. Am. Chem. Soc.* **1991**, *113*, 12-20.
- (16) Braun, H.-G.; Meyer, E. *Thin Solid Films* **1999**, *345*, 222-228.
- (17) Chapman, G.; Ostuni, E.; Yan, L.; Whitesides, G. M. *Langmuir* **2000**, *16*, 6927-6936.
- (18) Delamarche, E.; Donzel, C.; Kamounah, F. S.; Wolf, H.; Geissler, M.; Stutz, R.; Schmidt-Winkel, P.; Michel, B.; Mathieu, H. J.; Schaumburg, K. *Langmuir* **2003**, *19*, 8749-8758.
- (19) Typically, ~20 μL of aqueous solution is enough to provide a reservoir droplet of solution for filling a single channel. In comparison with standard methods for

enacting SAM formation, in which an entire substrate is immersed in solution, the required volumes for microfluidic patterning are small.

- (20) Yan, D.; Saunders, J. A.; Jennings, G. K. *Langmuir* **2000**, *16*, 7562-7565.
- (21) Yan, D.; Saunders, J. A.; Jennings, G. K. *Langmuir* **2002**, *18*, 10202-10212.
- (22) Liu, J.; Kaifer, A. E. *Isr. J. Chem.* **1997**, *37*, 235-239.
- (23) Porter, M. D.; Bright, T. B.; Allara, D. L.; Chidsey, C. E. D. *J. Am. Chem. Soc.* **1987**, *109*, 3559-3568.
- (24) The nature of this difference was unclear; some IRRAS data indicated the possibility of a contaminant codepositing with the SAM. Difficulty in spectral interpretation of the unusual bands observed when Tween 20 was adsorbed and then rinsed away from a gold substrate led to the exclusion of this data.
- (25) McDonald, J. C.; Duffy, D. C.; Anderson, J. R.; Chiu, D. T.; Wu, H.; Schueller, O. J. A.; Whitesides, G. M. *Electrophoresis* **2000**, *21*, 27-40.
- (26) Makamba, H.; Kim, J. H.; Lim, K.; Park, N.; Hahn, J. H. *Electrophoresis* **2003**, *24*, 3607-3619.
- (27) Michel, B.; Bernard, A.; Bietsch, A.; Delamarche, E.; Geissler, M.; Juncker, D.; Kind, H.; Renault, J.-P.; Rothuizen, H.; Schmid, H.; Schmidt-Winkel, P.; Stutz, R.; Wolf, H. *Chimia* **2002**, *56*, 527-542.
- (28) Papra, A.; Bernard, A.; Juncker, D.; Larsen, N. B.; Michel, B.; Delamarche, E. *Langmuir* **2001**, *17*, 4090-4095.
- (29) Chaudhury, M. K.; Whitesides, G. M. *Langmuir* **1991**, *7*, 1013-1025.
- (30) Ferguson, G. S.; Chaudhury, M. K.; Sigal, G. B.; Whitesides, G. M. *Science* **1991**, *253*, 776-778.

- (31) Genzer, J.; Efimenko, K. *Science* **2000**, *290*, 2130-2133.
- (32) Olander, B.; Wirsén, A.; Albertsson, A.-C. *J. Appl. Polym. Sci.* **2003**, *90*, 1378-1383.
- (33) Youn, B.-H.; Huh, C.-S. *Surf. Interface Anal.* **2003**, *35*, 445-449.
- (34) Schnyder, B.; Lippert, T.; Kotz, R.; Wokaun, A.; Graubner, V.-M.; Nuyken, O. *Surf. Sci.* **2003**, *532-535*, 1067-1071.
- (35) Berdichevsky, Y.; Khandurina, J.; Guttman, A.; Lo, Y.-H. *Sens. Actuators B* **2004**, *97*, 402-408.
- (36) Hillborg, H.; Ankner, J. F.; Gedde, U. W.; Smith, G. D.; Yasuda, H. K.; Wikström, K. *Polymer* **2000**, *41*, 6851-6863.
- (37) Donzel, C.; Geissler, M.; Bernard, A.; Wolf, H.; Michel, B.; Hilborn, J.; Delamarche, E. *Adv. Mater.* **2001**, *13*, 1164-1167.
- (38) Briggs, D. *Surface Analysis of Polymers by XPS and Static SIMS*; Cambridge University Press: Cambridge, UK, 1998.
- (39) Barr, T. L.; Seal, S. *J. Vac. Sci. Technol. A* **1995**, *13*, 1239-1246.
- (40) Graham, D. J.; Ratner, B. D. *Langmuir* **2002**, *15*, 1518-1527.
- (41) Lee, J. N.; Park, C.; Whitesides, G. M. *Anal. Chem.* **2003**, *75*, 6544-6554.

Chapter VI

Conclusions and Suggestions for Future Work

1. General Conclusions

The overall research goals as stated in the Introduction to this thesis were, broadly, to develop methods for manipulation of surface chemistry and protein adsorption as well as methods for the analysis of adsorbed films. The preceding chapters have shown the development of scanning probe microscopy (SPM) and surface plasmon resonance (SPR) imaging as instrumental probes of the properties of adsorbed films and the protein-binding interactions taking place at the solid-liquid interface. Of particular interest was the application of these techniques to the study of adsorbed protein films on chemically well-defined surfaces.

Chapter II detailed a case study of protein adsorption involving fibrinogen on patterned self-assembled monolayers (SAMs). The study was based around the discovery of a difference in the phase shift of the detected signal when an oscillating probe was used to image films of fibrinogen on a patterned methyl- and carboxylate-terminated monolayer. A variety of instrumental techniques, including infrared reflectance absorbance spectroscopy (IRRAS), SPR, and SPM force curve analysis revealed a difference in the adsorbed state of the fibrinogen depending on the underlying surface. The SPM phase imaging was shown to be probing local differences in overall conformational relaxations on the differently patterned regions of the substrate.

Further application of the manipulation of surface chemistry was shown in Chapter III. SPR imaging was shown to be a promising method for studying heterogeneous binding interactions using the example of protein antigen-antibody interactions. By controlling surface chemistry, it was possible to effect defined patterning of gold surfaces with thiolates and proteins using microfluidic channel devices constructed in poly(dimethylsiloxane) (PDMS). The soft lithographic methods employed in this work included microcontact printing (μ CP) and adsorption from solutions via microchannels. Some of the work towards modifying surface chemistries for expanding the scope of these modifications was presented in Chapter V. Plasma oxidation was shown to be a rapid, simple method for producing a functional surface on PDMS.

The utility of SPR imaging for biochemical interactions was expanded in Chapter IV, in which protein-carbohydrate interactions were analyzed at modified sensor surfaces. The tremendous advantages of array-based analysis with inherent detection were highlighted in both Chapters III and IV. The advantage of the SPR imaging and microfluidic patterning methodology in Chapter IV was particularly intriguing in direct comparison with ELISA methodologies. The SPR imaging-based methodology was shown to simplify the procedure for analysis of binding inhibition, especially in the detection of binding interactions.

2. Suggestions for Future Work

A further application of the phase imaging technique would be to evaluate lipid raft distributions on cell surfaces. Lipid rafts are hypothetical constructs entailing a

lateral structural organization of particular membrane lipid components, and represent a break from the traditional view of the laterally homogeneous fluid mosaic.¹ Using the Bioscope SPM instrument in our laboratory, it is possible to collect optical images from below a cell under buffer in a transparent petri dish. The configuration of the instrument is such that *in situ* SPM imaging can be performed using an inverted scanner with a cantilever probe attached. In this configuration, it is possible to immerse a sample in buffer and image individual cells using optical microscopy in combination with tapping-mode SPM. The advantage to studying cells in this manner would be the ability to measure changes in mechanical properties or adhesions over the surface of a cell membrane, potentially indicating the presence of lipid rafts. Of paramount importance in this endeavor would be the issue of sample preparation. Most studies aimed at imaging raft-like distributions involve artificial membranes on flat substrates due to the likely fluidity and transient nature of the structures.¹ In order to circumvent this problem, cryogenic sample preparation methods may need to be developed.

Another area of investigation, with a greater likelihood of producing useful data, would be the characterization of protein distributions in microspotted mixtures for matrix-assisted laser-desorption ionization mass spectrometry (MALDI-MS). MALDI for proteins typically involves mixing of sample with an organic molecule which can absorb radiation and vaporize proteins with a minimum of damage. The identification of candidate matrix molecules has been empirical, and no consistent set of rules exist to predict or explain the utility of a given matrix. The distribution of proteins within MALDI samples is notoriously heterogeneous, and has been studied by various techniques, none of which offer insight into the local protein-matrix interactions which

characterize a successful matrix.² High-resolution electron microscopy has been used to examine protein distributions in slowly grown MALDI crystals.² For real-world samples, however, phase imaging SPM may provide an operationally uncomplicated means of assessing the surface distributions of proteins in a matrix mixture.

In order to overcome the limitation of the imaging to the surface, a novel sample preparation by micro-scale tomography could be developed, whereby a stiff AFM cantilever would be used to scrape away surface layers at fixed depths, and a second probe could be used to then image the exposed regions. Such a technique would be useful for the visualization of nano-scale internal structures in soft samples such as gels and low-modulus crystals. Micro-toming has been used to prepare biological samples in hard matrices for TEM and SPM analysis;³ the proposed method differs in the ability to examine smaller-scale protein distributions and to prepare the sample using the same instrument for analysis.

Currently, work in our lab is underway employing the surface patterning and SPR imaging methods described in this thesis. An interesting extension of the work in Chapters III and IV would be to develop arrays for the specific detection of biomolecules and pathogens from biological fluids. The complex matrices that constitute real biological fluids, such as blood plasma, would make necessary a research effort into appropriate surface and sample preparation strategies to allow for detection from complex fluids without interference and non-specific adsorption.

Further research into the covalent modification of PDMS may also yield interesting results. The issue of seal failure may be overcome by the grafting of an alkyltrichlorosilane, allowing stronger dispersion interactions with the substrate. In

addition, it has been shown that high-density silanization of PDMS can be accomplished by mechanically elongating the polymer prior to oxidation and silanization.^{4, 5} When the stress is released, the PDMS adopts its original dimensions, but with a higher density of silanes on the surface than would have been grafted without the mechanical assistance. The hydrophobicity of native PDMS is due to the dense packing of methyl groups. By using a more densely packed group of long alkyl chains, it may be possible to confer a high level of resistance against permeation by organic solvents and thiols, as well as to maintain an integral seal against gold.

3. References

- (1) Mayor, S.; Rao, M. *Traffic* **2004**, *5*, 231-240.
- (2) Horneffer, V.; Reichelt, R.; Strupat, K. *Int. J. Mass. Spectrom.* **2003**, *226*, 117-131.
- (3) Matsko, N.; Mueller, M. *J. Struct. Biol.* **2004**, *146*, 334-343.
- (4) Genzer, J.; Efimenko, K. *Science* **2000**, *290*, 2130-2133.
- (5) Wu, T.; Efimenko, K.; Genzer, J. *Macromolecules* **2001**, *34*, 684-686.